Spring 2014

Flow structure and vorticity transport on a plunging wing

Azar Eslam Panah
University of Iowa

FLOW STRUCTURE AND VORTICITY TRANSPORT ON A PLUNGING WING

by

Azar Eslam Panah

A thesis submitted in partial fulfillment of the
requirements for the Doctor of Philosophy
degree in Mechanical Engineering
in the Graduate College of
The University of Iowa

May 2014

Thesis Supervisor: Assistant Professor James H. J. Buchholz

Graduate College
The University of Iowa
Iowa City, Iowa

CERTIFICATE OF APPROVAL

PH.D. THESIS

This is to certify that the Ph.D. thesis of

Azar Eslam Panah

has been approved by the Examining Committee for the thesis requirement for the Doctor of Philosophy degree in Mechanical Engineering at the May 2014 graduation.

Thesis Committee: _____
James H. J. Buchholz, Thesis Supervisor

_____
Frederick Stern

_____
H.S. Udaykumar

_____
Pablo M. Carrica

_____
Sarah C. Vigmostad

ACKNOWLEDGEMENTS

I would like to express my sincere gratitude and grateful thanks to my advisor, Prof. James Buchholz, for his extensive wisdom, great guidance, extreme encouragement, close support, and distinguished supervision throughout this study which helped me to overcome many challenges. The opportunity to work with one of the best professors in the area of fluid mechanics was a great honor for me and I hope I can be as productive and energetic as he is. Also, I would like to thank him for the opportunity of presenting my work at several conferences and sharing the latest developments in the fluid dynamics field with other researchers, which was an invaluable experience for me as I move forward in my career life.

I would like to extend my gratitude to my committee members, Prof. Frederick Stern, Prof. H.S. Udaykumar, Prof. Pablo Carrica, and Prof. Sarah Vigmostad, for their valuable time and suggestions to evaluate of this work. Thanks to many people in the MIE Department and IIHRHydroscience & Engineering Laboratory for their constant support in every aspect of this work and for their instant help specially Laura Myers, Timothy Houser, Brandon Barquist, and Greg Wagner.

I have also been fortunate to have many great colleagues including Mohammad Hajimirzaie, Craig Wojcik, James Akkala, Jordan Null, and Kevin Wabick, who have generously shared their knowledge, time, effort, and friendship. This journey would not have gone smoothly without having great friends by your side providing joyful times beyond stressful school work and research time.

I owe my heartfelt gratitude and thanks to my parents and sister for their moral support and motivation. Last but the most, I am grateful to my husband Amir Barakati for his encouragement, support, patience, love and everything, who deserves all the best.

I also want to mention that this work was supported by the Air Force Office of Scientific Research under Award Number FA9550-11-1-0019, monitored by Dr. Doug Smith.

ABSTRACT

The structure and dynamics of the flow field created by a plunging flat plate airfoil are investigated at a chord Reynolds number of 10,000 while varying plunge amplitude and Strouhal number. Digital particle image velocimetry measurements are used to characterize the shedding patterns and the interactions between the leading and trailing edge vortex structures (LEV and TEV), resulting in the development of a wake classification system based on the nature and timing of interactions between the leading- and trailing-edge vortices. The convection speed of the LEV and its resulting interaction with the TEV is primarily dependent on reduced frequency; however, at Strouhal numbers above approximately 0.4, a significant influence of Strouhal number (or plunge amplitude) is observed in which LEV convection is retarded, and the contribution of the LEV to the wake is diminished. It is shown that this effect is caused by an enhanced interaction between the LEV and the airfoil surface, due to a significant increase in the strength of the vortices in this Strouhal number range, for all plunge amplitudes investigated. Comparison with low-Reynolds-number studies of plunging airfoil aerodynamics reveals a high degree of consistency and suggests applicability of the classification system beyond the range examined in the present work. Some important differences are also observed.

The three-dimensional flow field was characterized for a plunging two-dimensional flat-plate airfoil using three-dimensional reconstructions of planar PIV data. Whereas the phase-averaged description of the flow field shows the secondary vortex penetrating the leading-edge shear layer to terminate LEV formation on the airfoil, time-resolved, instan-

taneous PIV measurements show a continuous and growing entrainment of secondary vorticity into the shear layer and LEV. A planar control volume analysis on the airfoil indicated that the generation of secondary vorticity produced approximately one half the circulation, in magnitude, as the leading-edge shear layer flux. A small but non-negligible vorticity source was also attributed to spanwise flow toward the end of the downstroke.

Preliminary measurements of the structure and dynamics of the leading-edge vortex (LEV) are also investigated for plunging finite-aspect-ratio wings at a chord Reynolds number of 10,000 while varying aspect ratio and root boundary condition. Stereoscopic particle image velocimetry (SPIV) measurements are used to characterize LEV dynamics and interactions with the plate in multiple chordwise planes. The relationship between the vorticity field and the spanwise flow field over the wing, and the influence of root boundary conditions on these quantities has been investigated. The viscous symmetry plane is found to influence this flow field, in comparison to other studies [82, 66, 15], by influencing tilting of the LEV near the symmetry wall, and introducing a corewise root-to-tip flow near the symmetry plane. Modifications in the root boundary conditions are found to significantly affect this. LEV circulations for the different aspect ratio plates are also compared. At the bottom of the downstroke, the maximum circulation is found at the middle of the semi-span in each case. The circulation of the $sAR = 2$ wing is found to significantly exceed that of the $sAR = 1$ wing and, surprisingly, the maximum circulation value is found to be independent of root boundary conditions for the $sAR = 2$ case and also closely matched that of the quasi-2D case.

Furthermore, the 3-D flow field of a finite wing of $sAR = 2$ was characterized using

three-dimensional reconstructions of planar PIV data after minimizing the gap between the plunging plate and the top stationary wall. The LEV on the finite wing rapidly evolved into an arch structure centered at approximately the 50% spanwise position, similar to previous observations by Calderon et al. [16], and Yilmaz and Rockwell [82]. At that location, the circulation contribution due to spanwise flow was approximately half that of the shear layer flux because of the significantly greater three-dimensionality in the flow. Increased tilting at the 25% and 75% spanwise locations suggests increasing three-dimensionality at those locations compared to the symmetry plane of the arch (50% spanwise location). The deviation between the LEV circulation and integrated convective vorticity fluxes at the 50% spanwise location suggests that entrainment of secondary vorticity plays a similar role in regulating LEV circulation as in the 2D case. While the wing surface flux of vorticity could not be measured in that case, the significant difference between LEV circulation and the known integrated fluxes is comparable to that for the 2D plate, suggesting that a significant boundary flux of secondary vorticity may exist.

TABLE OF CONTENTS

LIST OF FIGURES

Figure

CHAPTER 1
INTRODUCTION

Birds, insects, and aquatic animals use oscillatory and undulatory motions to generate lift and thrust in a manner that produces high agility and often also efficiency. A wide range of investigations, reviewed by Sane [55], Wang [74], Platzer et al. [49], Lentink and Dickinson [42], Dabiri [20], and Shyy et al. [56], have improved our understanding of unsteady aerodynamics for the design and development of flapping wing micro-aerial vehicles and agile unmanned combat air vehicles. These studies have been motivated by the notable flight characteristics of insects and birds, which involve a variety of wing motions. At least two fundamental questions are introduced in these types of classical unsteady aerodynamic problems. One is how the trailing edge vortex (TEV) sheds into the wake whenever there is a change in effective angle of attack, either due to pitch or plunge which is an essentially inviscid problem. The second question is how the leading edge vortex (LEV), whose formation, pinch-off, advection and shedding into the wake are the core problems of dynamic stall, contributes to the overall vorticity transport in the flow field.

Although unsteady aerodynamics models for predicting the aerodynamic forces have been improved recently [73], they are typically validated for single canonical maneuvers of specific geometries. Wagner [71] and Theodorsen [60] initiated the low-order modeling of unsteady aerodynamics and established a basis for analyzing such problems by decomposing the forces and moments on the wing into contributions from circulatory and non-circulatory effects. Such classical vortex models are reliable for low angles of attack, but they cannot predict forces when the angle of attack is increased where the LEV

presents. For a pitching motion, McCroskey et al. [70] pointed out that as the LEV passes over the airfoil surface, it significantly changes the chordwise pressure distribution and produces transient forces and moments fundamentally different from those in static stall. Wu [79] showed that for the simple case of any bound circulation, the sectional lift is equal to the product of the circulation (Γ) created by a wing and its translational velocity (U) , in agreement with the Kutta-Jukowski theorem, as below:

$$\mathrm{F} = \mathrm{U} \times \Gamma \vec{e_y} \tag{1.1}$$

where $\vec{e_y}$ is the unit vector along the vortex axis. In this formula F is related to a contineous shedding of the vorticity created on the body surface.

Since the vorticity shed from oscillating aerodynamic bodies can significantly alter the aerodynamic forces on the body, the dynamics of the flow field have been reported for a broad range of kinematics, geometries, and dynamic and kinematic parameters (Williamson and A. Roshko [75], Freymuth [25], Koochesfahani [39], Triantafyllou et al. [62, 61], Anderson et al. [3], Lai and Platzer [40], Lewin and Haj-Hariri [43], Lua et al. [46]). Of equal importance, the shed vorticity field can significantly impact aerodynamic loads on other bodies that are present in the wake, such as tandem wings or fins and other members within a formation (Akhtar et al. [2], Rival et al. [51], Lua et al. [45], and Gopalkrishnan [27]), and thus understanding the evolution of the shed vorticity can provide insight into flow interactions within bird flocks and fish schools, as well as the control of biorobotic vehicles. Moreover, the observations from boundary vorticity dynamics ([79] and [80]) suggest that one must be able to express the total force and moment in terms of the boundary vorticity fluxes.

In the present work, we are intrested in a periodic plunge motion through a range of Strouhal numbers and plunge amplitudes on the order of those observed in biological locomotion in fluids. Many previous investigations are concerned with either amplitudes that are small compared with that of flying or swimming animals (Freymuth [24]; Jones et al. [36]; Lai and Platzer [40]; Young and Lai [84], Bohl and Koochesfahani [7]), which tend to be on the order of the wing or fin chord length; or the dimensionless frequencies are lower than those observed in biological locomotion (Lewin and Haj-Hariri [43], Lua et al. [46]), as reported by Hu et al. [33]. This chapter represents a review of the relevant literature of unsteady aerodynamics.

1.1 Prior Research on Two-Dimensional Wakes

1.1.1 Wakes of 2D Oscillating Foils

It is well known that flapping airfoils generate thrust at certain combinations of flapping frequency and amplitude. Previous characterizations of flow structure at low Reynolds number, $O(100)$ to $O(1000)$ and low amplitudes have shown the type of wake structure produced may depend on Strouhal number, or reduced frequency (or non-dimensional plunge amplitude h_o/c), but knowledge of the vortex topology in the unsteady wakes remains incomplete and the role of each parameter is not clear. For propulsion with periodically-articulated airfoils, Triantafyllou et al. [62, 61] conducted a linear stability analysis on the mean wake profile to demonstrate that a) Strouhal number $St = fA/U$ (where f is the frequency of oscillation, A is the wake width or peak-to-peak amplitude of the trailing edge, and U is the swimming speed or free-stream velocity) is the primary parameter governing

thrust performance, and b) that optimal propulsive efficiency occurs within the approximate range $0.25 \leq St \leq 0.35$. They supported this conclusion with experimental measurements and the observation that a broad range of aquatic animals swim within this Strouhal number range. These ideas were extended to flapping flight by Taylor et al. [59], who observed that the flapping kinematics of several bird species were also tuned to this Strouhal number range. However, additional dependencies on other parameters have also been identified. The reduced frequency $k = \pi fc/U$ (where c is the chord length), which is a dominant parameter emerging from ideal, linearized unsteady aerodynamic theory (Theodorsen [60], Bisplinghoff et al. [5]), has also been identified as an important parameter governing aerodynamic performance and flow structure. Gharib, Rambod, and Sharif [26] introduced the formation number $n = Ut/D = L/D$ for a piston-generated axisymmetric vortex ring. As illustrated in Figure 1.1, at $n \approx 4$, the vortex ring was found to pinch off such that no additional vorticity would be entrained into the ring and instead forms secondary vortices akin to a Kelvin-Helmholtz instability. As defined by Dabiri [20], vortex ring pinch-off is the process whereby a forming vortex ring is no longer able to entrain additional vorticity from a vortex generator.

Focusing on plunging motion, dye visualization experiments of Lai and Platzer [40] on a plunging NACA-0012 airfoil showed that for $4.0 \leq k \leq 20.0$, the wake structures originated from only the trailing edge of the airfoil (Figure 1.2). In a subsequent numerical study, Young and Lai [84] used a 2D Reynolds-Averaged Navier-Stokes (RANS) approach to study the frequency-amplitude parameter space for optimal thrust efficiency for a plunging NACA-0012 airfoil at $Re = O(10^4)$, and Jones et al. [36] demonstrated good agree-

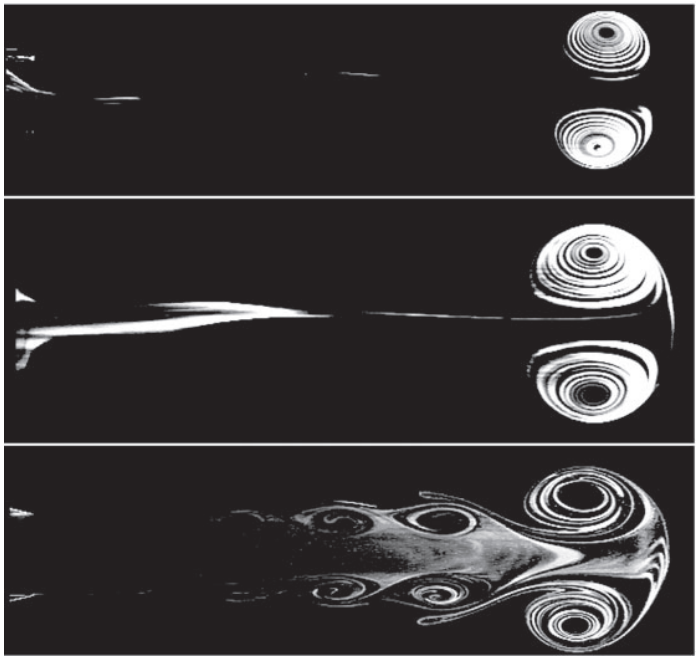

Figure 1.1: Visualization of vortex rings at downstream position $X/D \approx 9$ for (a) $\hat{T} = 2$, (b) $\hat{T} = 3.8$, and (c) $\hat{T} = 14.5$ (Adopted from Gharib et al. [26]).

ment in wake vortex structure between dye injection at the airfoil trailing edge in a water tunnel, 2D laminar Navier-Stokes computation, and a 2D vortex-particle method. They showed that, although leading-edge separation occurs for $k \leq 4$, wake structures appear to be controlled primarily by trailing-edge effect only. They demonstrated that the wake structure simulations and thrust calculations carried out at constant St show that this cannot be the single parameter controlling the flow, but that k and kh must be treated separately for $k \leq 4$ approximately and for the Reynolds number under consideration. Lewin and Haj-Hariri [43] numerically investigated the wake structure and thrust performance of a plunging airfoil at $Re_c = 500$. They found a dependence of wake structure on Strouhal number and reduced frequency. Leading edge vortices were found to be shed within the

ranges $0.25 \leq St \leq 0.48$ and $1.0 \leq k \leq 4.0$. For $k < 4$, discrete LEVs are shed; whereas at higher k, nascent LEVs shear the previously generated vortex and do not advect downstream (Figure 1.4). At increased St, asymmetry, and aperiodicity are observed in the wake. They found that the wake patterns depend primarily on the fate of the LEV: whether or not it is shed, and how it interacts with the TEV. When shed, the LEV can either reinforce (positively or negatively) the TEV, resulting in two vortices shed into the wake per flap, or it can form a counter-rotating pair with the TEV, resulting in four vortices shed per flap.

In a recent experimental study, Lua et al. [46] identified five different wake structures generated by a harmonically plunging elliptic airfoil, caused by different interactions between the vortices shed from the leading and trailing edge dependent on frequency and amplitude (Figure 1.5). They found that the type of wake structure produced depends on not only the Strouhal number, but also the non-dimensional plunge amplitude. Focusing on the more relevant range of Reynolds numbers, Koochesfahani [39] studied high-frequency low-amplitude airfoil pitch oscillations with quantitative and qualitative visualization, identifying vortex shedding patterns vs. motion kinematic parameters. He experimentally examined the wake structure produced by a NACA-0012 airfoil at $Re_c = 12,000$, as shown in Figure 1.6. The kinematics of the airfoil were characterized in terms of the reduced frequency $0.835 \leq k \leq 10.0$. In general, for small k, a net drag force was experienced and four spanwise vortices were shed in each pitching cycle, forming two counter-rotating pairs, as shown. Two streamwise momentum deficits were observed corresponding to the velocity fields induced by the vortex pairs. With increasing k, only two vortices were shed in each pitching cycle aligned parallel to the free stream to form a momentumless wake.

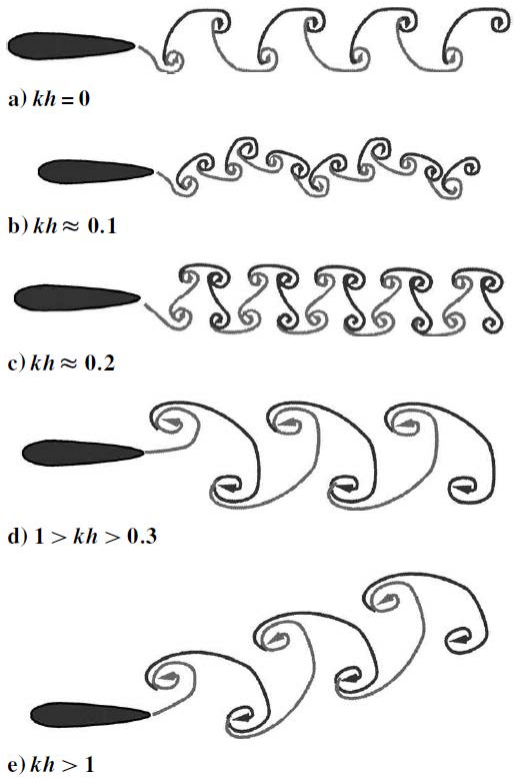

Figure 1.2: Sketches of the wake of a plunging airfoil for various kh values. Note that h is nondimensional amplitude of oscillation, and kh is nondimensional plunge velocity which is proportional to St (Adopted from Lai and Platzer [40]).

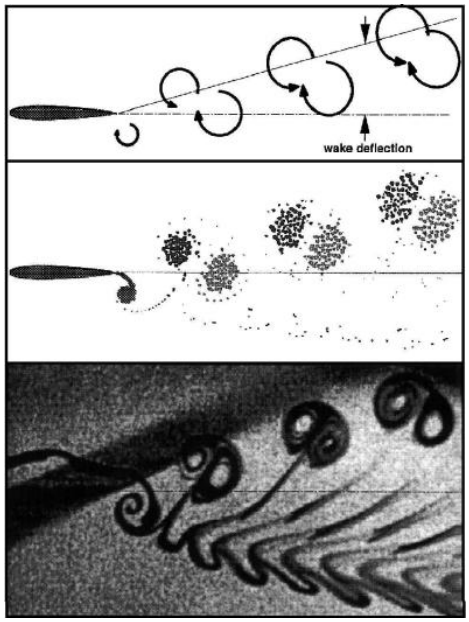

Figure 1.3: Asymmetric wake produced by a plunging airfoil for St = 0.48, and ho/c=0.12 (Adopted from Jones et al. [36]).

With further increases in k, the vortices are slightly displaced in the transverse direction to form a pattern resembling a von Karman vortex street but with the signs of the vortices reversed such as to produce a mean addition of momentum rather than a deficit. For the two pitching amplitudes examined, the estimated thrust coefficients were found to fall on two distinct curves with varying k. Anderson et al. [3] used particle image velocimetry and direct force measurement to study the combined pitch-plunge parameter space for propulsive efficiency optimization, conducting a large parameter study, albeit force measurements and flow field data were obtained at quite disparate Reynolds numbers (1.7). They demonstrate the significance of the Strouhal number on the form of the wake, as predicted by the theory of Triantafyllou et al. Their results for lower h_o/c show nearly identical trends as far as the

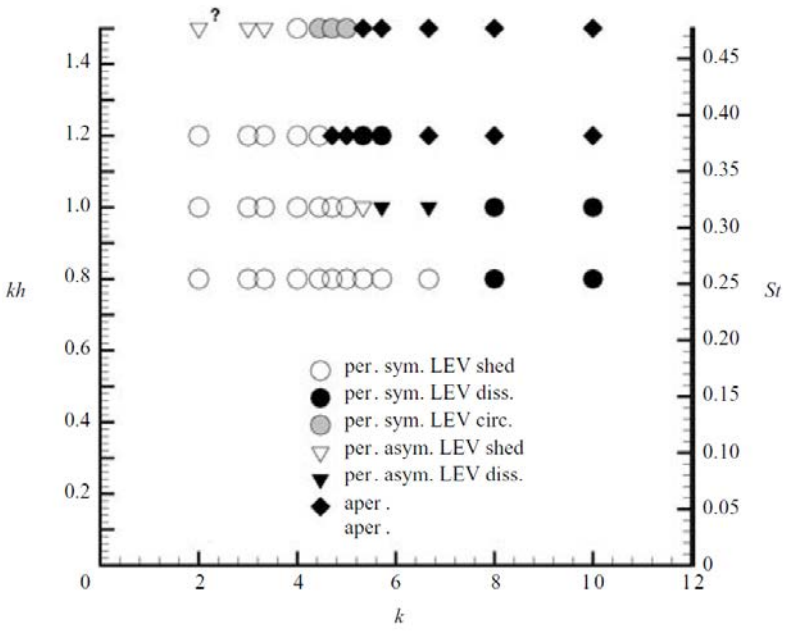

Figure 1.4: Qualitative results for all simulations, based on k and kh. per=periodic; aper= aperiodic; sym=symmetric; asym=asymmetric; LEV shed=LEV shed into flow; LEV diss=LEV dissipated by interaction with the leading edge/nascent LEVs; LEV circ=LEV circumnavigates the leading edge and is shed on the other side (Adopted from Lewin and Haj-Hariri [43]).

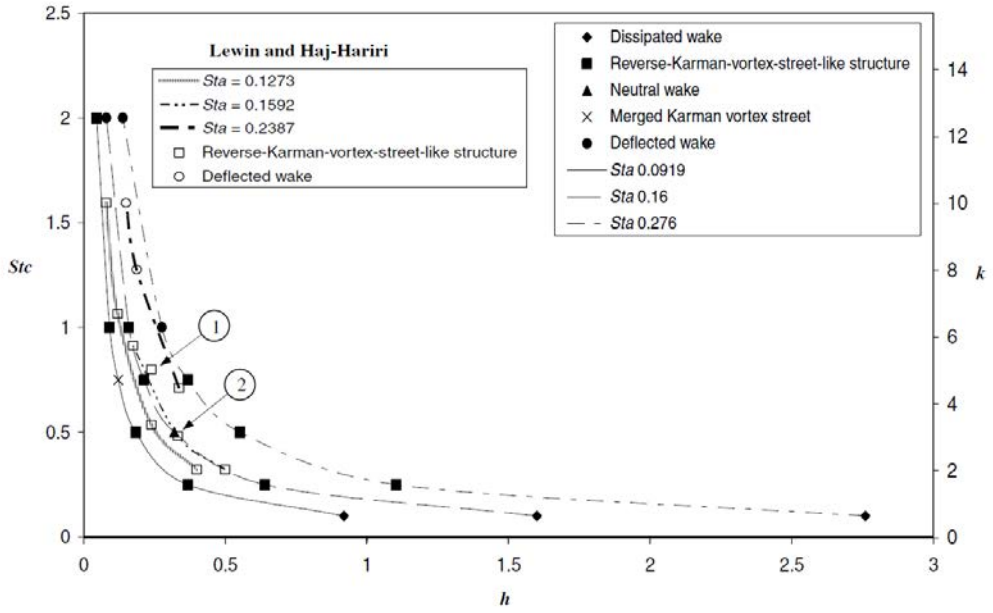

Figure 1.5: A plot showing the dependency of wake structures on St_a, St_c, and h_o/c. Note that $St_c = k/2\pi$ and $St_a = kh/2\pi$. Open symbols represent the computation results of Lewin and Haj-Hariri [43]. Solid symbols represent the Lua et al. [46] results. (Adopted from Lua et al. [46])

wake form is concerned; however, the formation of a leading-edge vortex depends on h_o/c and angle of attack. They found that optimum efficiency occurs when the leading-edge vortices interact constructively with the trailing-edge vortex, leading to two vortices deposited per flap.

1.1.2 Vortex Interaction with a Wall

In order to develop robust models for wake structure and aerodynamic loads, it is therefore important to understand the physics of leading-edge vortex formation and the

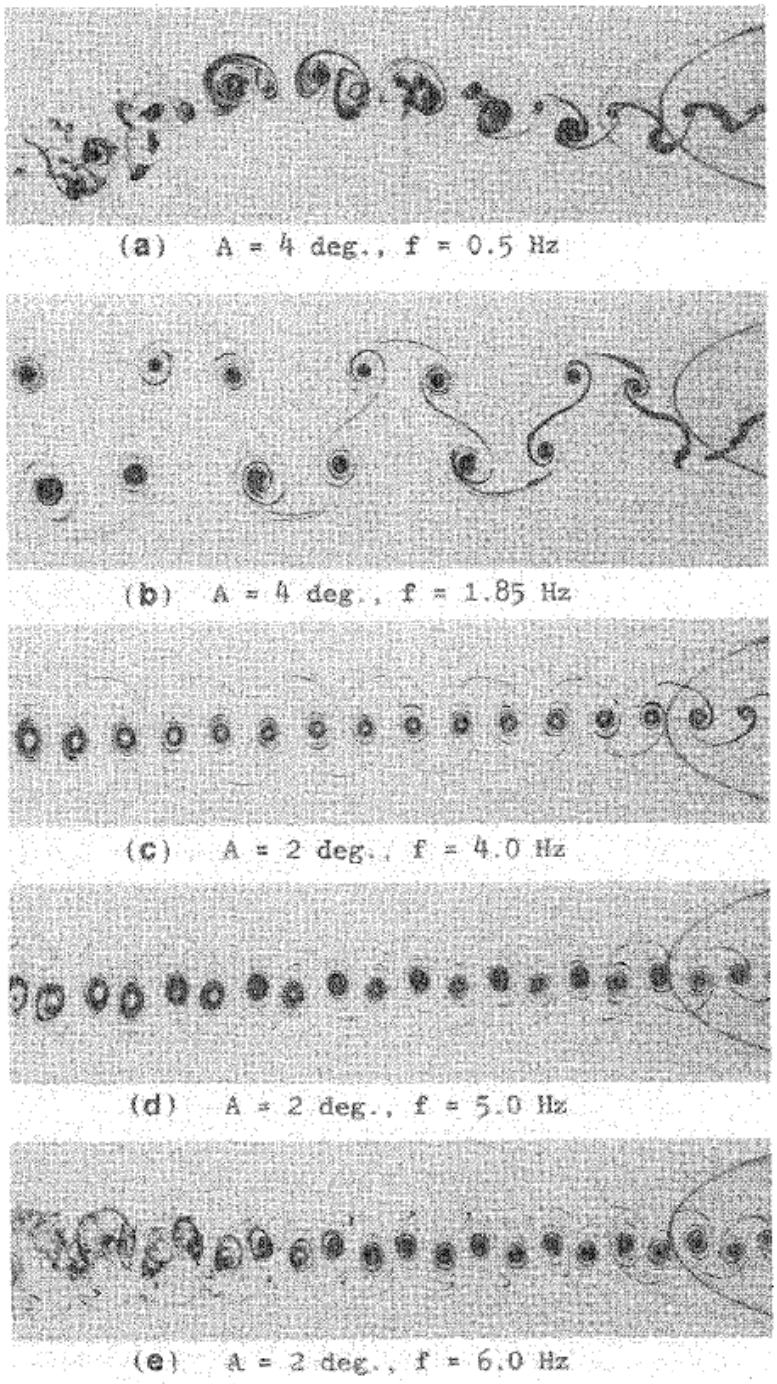

Figure 1.6: Wake of a NACA-0012 airfoil pitching sinusoidally about 1/4-chord point (Adopted from Koochesfahani [39]).

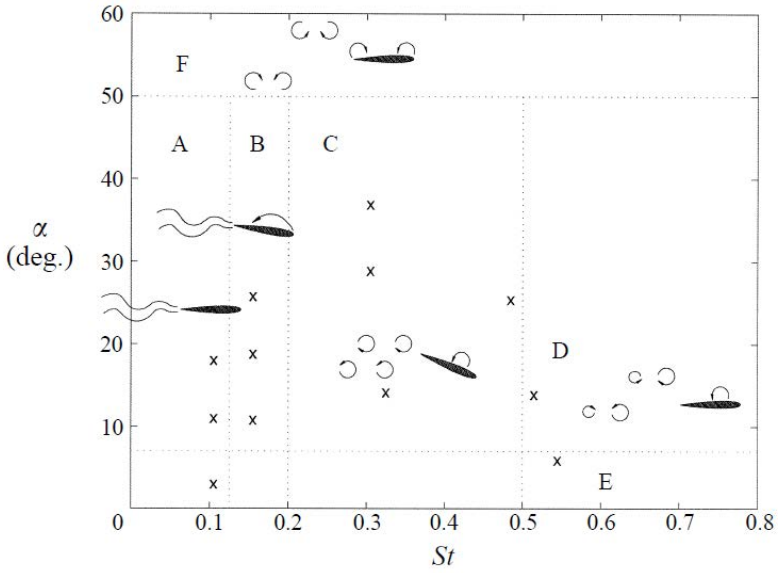

Figure 1.7: Wake patterns as function of the Strouhal number and angle of attack for ho/c = 1 (Adopted from Anderson et al. [3]).

mechanisms which are responsible for its strength. As will be shown in this dissertation, interaction of the leading-edge vortex with the surface of the airfoil has a significant impact on vortex strength. Visbal[64] performed high-fidelity large eddy simulations of a plunging airfoil at Reynolds numbers between 10,000 and 60,000 and noted that, when the shear layer became transitional, secondary vorticity, of opposite sign to the leading-edge vortex, became entrained into the leading-edge vortex. Wojcik and Buchholz[77] observed a similar phenomenon on the *attached* leading-edge vortex on the inboard portion of a rotating blade, and inferred that the rate of annihilation of the leading-edge vortex due to entrainment of secondary vorticity is often comparable to the circulation flux in the leading-edge shear layer. Lewin and Haj-Hariri[43] performed numerical simulations of a plunging airfoil at $Re = 1000$, and noted that the evolution of the secondary vorticity appeared to

participate in the disconnection of the leading-edge vortex from the leading-edge shear layer. These observations all suggest that the interaction of the leading-edge vortex with the surface of a wing or airfoil plays an important role in governing the evolution of the vortex, and therefore also the aerodynamic loads.

Many studies before on vortex interaction with walls are dedicated to infinite walls, which were comprehensively reviewed by Doligalski et al. [21]. A dominant concept is the eruption of the wall boundary layer leading to secondary vortex, originally calculated by Walker [72] for a vortex along a wall. Figure 1.8 shows a schematic representation of the various stages of ”spike-like” vortex layer formation upstream of the LEV. This vortex layer appears at high Reynolds numbers and gives rise to a thin plume containing significant levels of vorticity, which rapidly leaves the surface as shown in Figure 1.8 (c). Acharya and Metwally [1] mentioned that, [the opposite-sign vorticity] cuts off the dynamic-stall vortex from its source of vorticity. Luton et al. [47] numerically investigated the interaction of a spanwise convective vortex with a boundary layer using incompressible Navier-Stokes equations. They showed that a strong vortex induces an eruption and produces a secondary vortex. The secondary vortex causes the primary vortex to rebound. However, weaker vortices do not follow the inviscid trajectory despite the absence of a secondary vortex. A weaker vortex redistributes the vorticity of the boundary layer, pulling it away from the wall, which alters the vortex trajectory.

Very recently, Rival et al. [53], experimentally investigated the LEV growth and detachment in a free-surface water tunnel with different leading-edge shapes. The tests have been performed at $Re_c = 10,000$, $k = 0.25$ and $St = 0.16$. The leading-edge shape

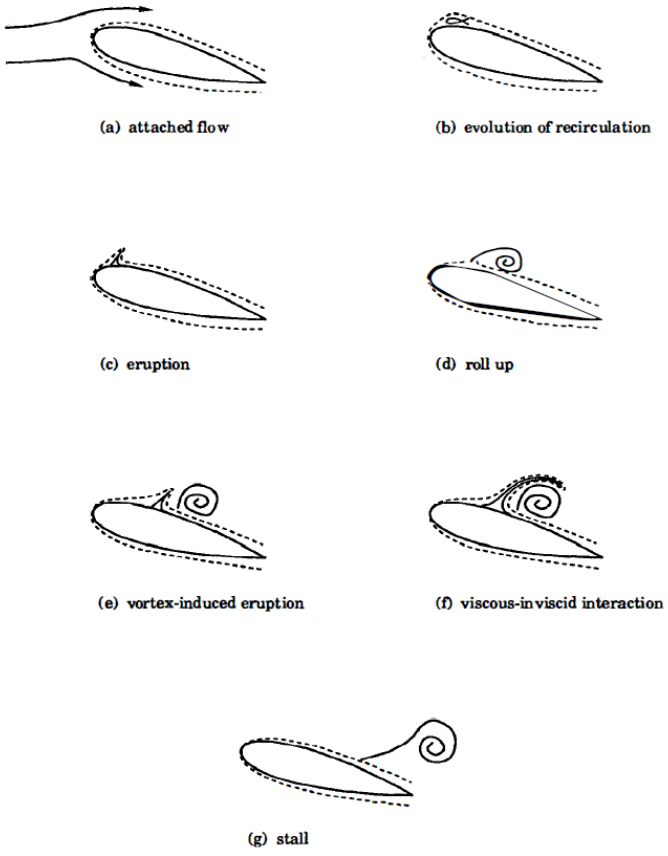

Figure 1.8: Schematic of stages of dynamic stall at high Reynolds number (Adopted from Doligalski et al. [21].

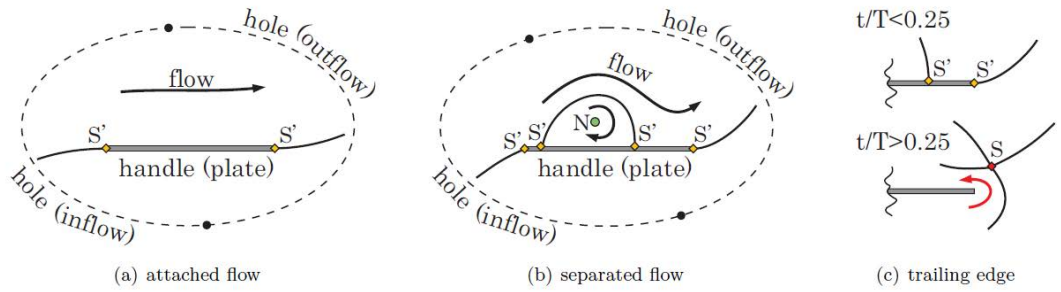

(a) attached flow (b) separated flow (c) trailing edge

Figure 8. Sketches of possible topological scenarios for a collapsed sphere with one handle (plate) and two holes (in-/outflow boundary): (a) attached flow with two half-saddles S' at leading and trailing edge; (b) a separated region on the plate leads to one additional node N and two additional half-saddles S'; (c) the rear stagnation point S' and trailing-edge stagnation point S' merge to a (separated) full saddle S such that the a channel for reversed flow opens, as indicated by the red arrow (half-saddle S' ♦, full-saddle S ♦, node N ●, boundary switch point ●, sphere of interest - - -).

Figure 1.9: Adopted from Rival et al. [53]).

is shown to influence the feeding shear layer; and thus the development of the LEV. They argued that there are two mechanisms that are responsible for LEV detachment process: a) eruption layer (secondary vorticity), b) flow reversal from the trailing edge. The former is affected by the vortex growth rate and thus the feeding shear layer. The latter dictates the overall maximum circulation of the LEV and forces a rapid cut-off once the rear stagnation point passes off of the trailing edge. They showed that the opposite-sign vorticity causes the half saddle to lift off and form a full saddle, in turn allowing the rapid feeding of trailing-edge vorticity forward to cut off the LEV as illustrated in Figure 1.9. Therefore, the trailing edge (chord length) plays a critical role of limiting the LEV size (circulation) and this is the most characteristic length scale for the vortex-separation process at higher Reynolds numbers, where the eruption process will be less pronounced.

We need to clarify the effect of secondary vorticity on LEV strength and detachment from feeding shear layer, also to determine the role of vorticity transport equation's terms

to understand the physical mechanisms governing the form and the strength of the wake.

1.2 Prior Research on Three-Dimensional Wakes

1.2.1 Wakes of 3D Oscillating Foils

Experimental and numerical investigations have shown that the flow structure in the wakes of finite-aspect-ratio wings is complex and three-dimensional, and is therefore fundamentally different from that of two-dimensional airfoils. Freymuth [24] represented the formation of a vortex ring in the wake of a wing, including trailing edge and tip vortices. Furthermore, the ends of the leading edge vortex were observed to anchor onto the surface of the wing shedding to the wake to form its own vortex ring. Von Ellenrieder, Parker and Soria [69] characterized the topological features of the near-wake of oscillating wing. They proposed a model based on dye visualization of the flow field of a pitching and plunging finite-AR rectangular wing at $Re_c = 164$ and $St = 0.35$. As shown in Figure 1.10, the model consists of two merged vortex rings shed in each stroke where each structure wrapped around the nearby structure. These connected vortex rings were generated from wing tip vortices and successive trailing and leading edge vortices. Moreover, Blondeaux et al. [48] and Dong, Mittal and Najjar [22], computationally characterized the features of the vortical structures and their interaction in the near-wakes of an airfoil and an elliptical planform. Blondeaux et al. [48] performed full three-dimensional numerical simulations, in order to quantitatively analyse the unsteady flows studied by Freymuth [24] and von Ellenrieder et al. [69]. Dong et al. [22] used an immersed boundary method to simulate the flow field and thrust performance of a pitching and plunging ellipsoidal wing, for $Re_c = 200$, and

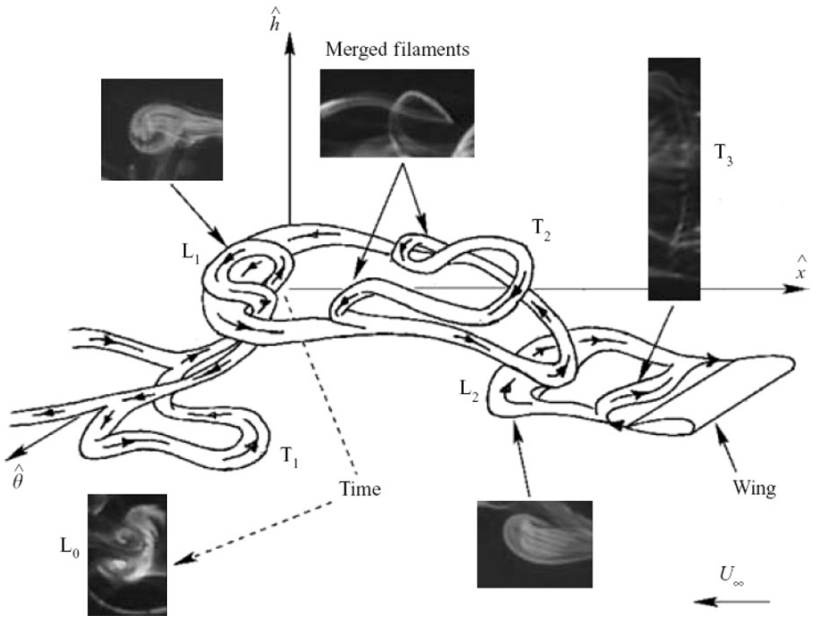

Figure 1.10: Sketch of the flow structure behind a pitching and plunging wing of aspect ratio 3 (Adopted from von Ellenrieder et al. [69]).

$St = 0.6$. They found the wake to consist of a separated array of vortex rings, where each ring was formed from a vortex shed from the trailing edge and the connection of two tip vortices as illustrated in Figure 1.11. A leading edge vortex is also shed, but it is not clear how it is merged to the wake. They also investigated the effect of aspect ratio on these wake structures, illustrating that reducing the aspect ratio has the effect of strengthening the interaction between tip vortices, altering the formation of vortex rings which propagate downstream under their own self-induced velocity.

For the panels pitching about its leading edge, Buchholz and Smits [13] defined the topology in the wake region using a combination of qualitative and quantitative imaging. They made a model of the wake of a finite-AR rectangular plate at $Re_c = 640$, using both

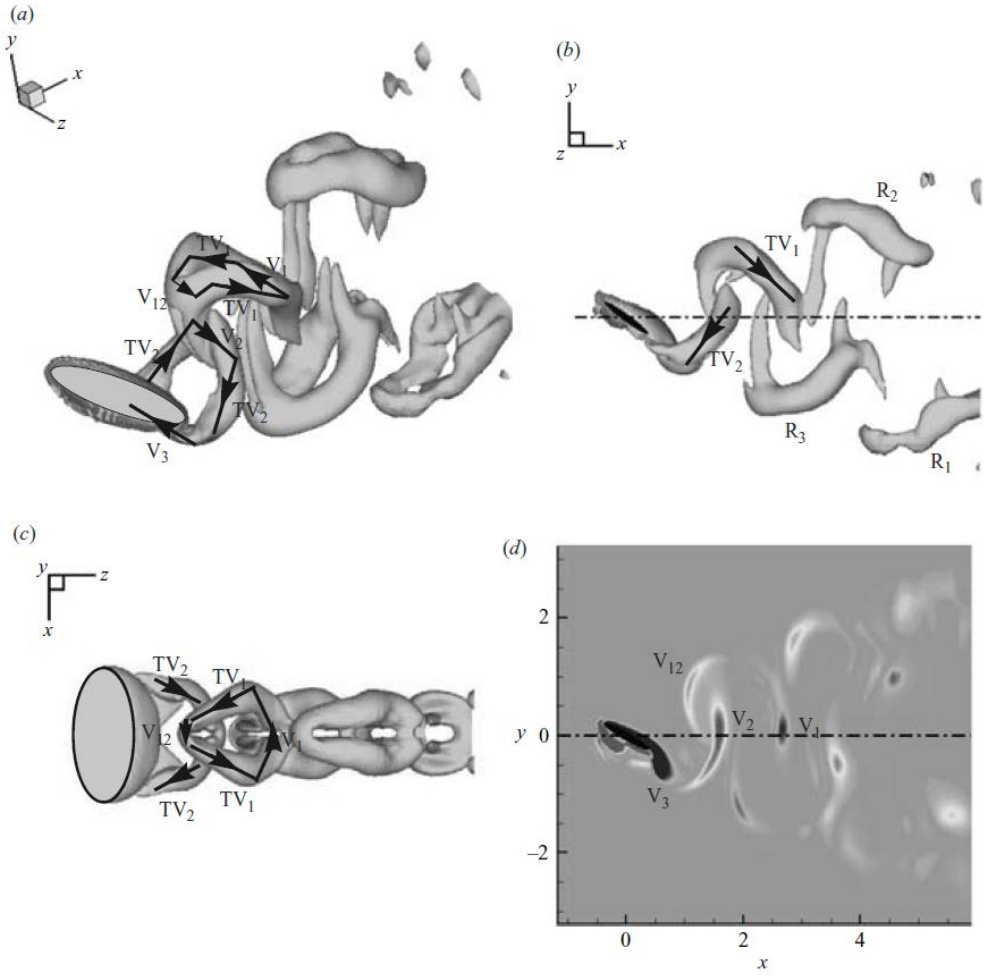

Figure 1.11: Wake topology of an ellipsoidal foil of aspect ratio 2.55 at St = 0.6 (Adopted from Dong et al. [22]).

dye visualization and DPIV to develop a qualitative vortex skeleton model supported by quantitative measurements of vortex circulation (Figures 1.12(a) and 1.12(b)). The dye visualization picture and wake model is shown in Figures 1.12(c) and 1.12(d). Regardless of the presence or absence of a leading edge vortex, differences in aspect ratio, geometry and kinematics, their model was very similar to Dongs pattern. Clark and Smits [18] examined a mechanical model of a flexible manta ray with oscillating wings, and proposed wake models consistent with the previous studies. They reported that at low Strouhal numbers ($St < 0.15$), near the root, there is minimal vortex interaction because little circulation is generated in this region. At higher Strouhal numbers, in regions away from the root, a greater degree of vortex interaction generates spanwise compression of the wake, which makes the wake spread above and below the planform.

More recently, Borazjani and Sotiropoulos [8, 9, 10] investigated the effect of geometry, kinematics, and Reynolds number on wake structure by computing the flow field generated by three-dimensional swimming bodies at $Re_c = O(100)$, $O(10^4)$, and $O(\infty)$. They concluded that, while Reynolds numbers and Strouhal numbers had strong effect on the shape of the wakes, each wake could have been fit in one of the previous models (Figure 1.13). Taira and Colonius [58] computed the wake structure from impulsively translated plates and characterized the strong interaction between the tip and trailing-edge vortex systems.

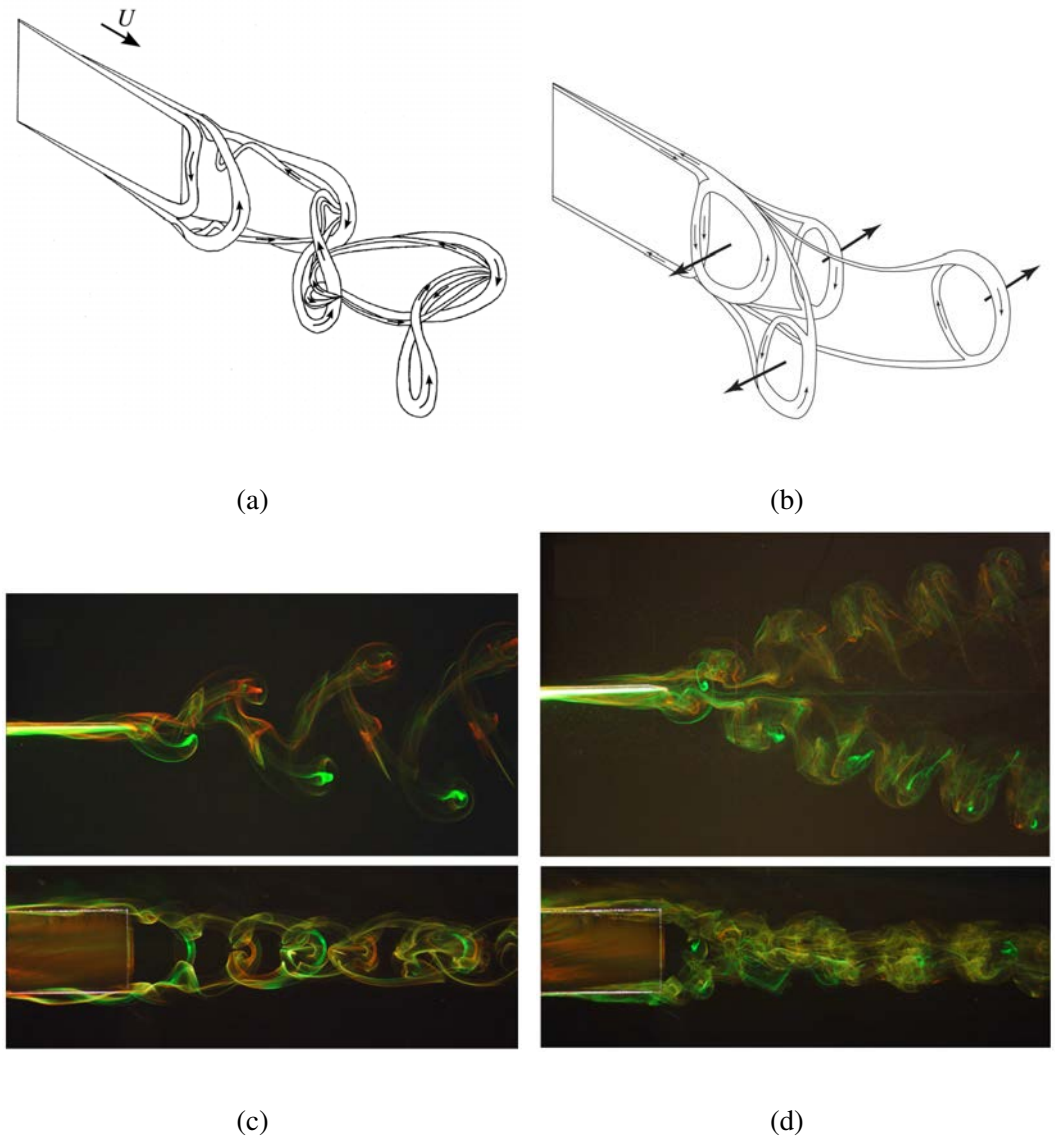

Figure 1.12: Vortex skeleton and dye visualization of wakes for $S/C = 0.54$, $A/S = 0.31$, $Re_C = 640$, a,c) $St = 0.43$, b,d) $St = 0.23$; (Adopted from Buchholz [13]).

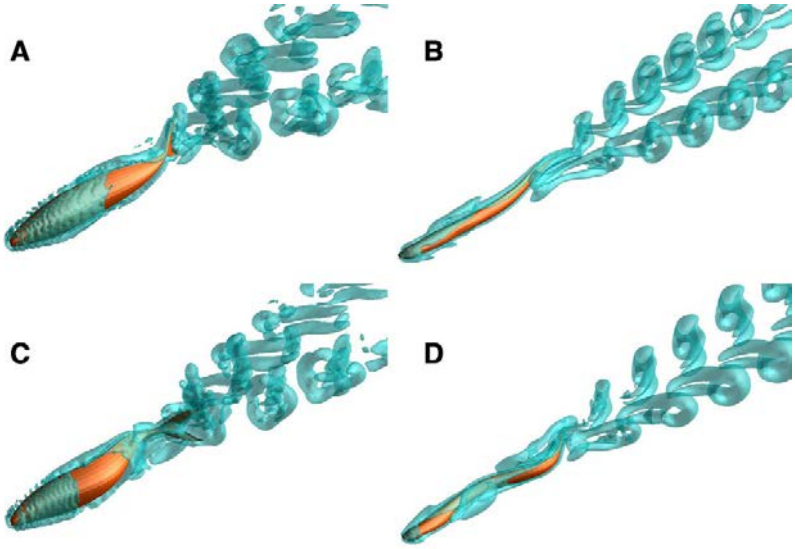

Figure 1.13: Wake structure visualized by the isosurfaces of q-criterion for $Re_o = 4000$, $St_o = 0.6$, for self-propelled virtual swimmers: (A) mackerel swimming like a mackerel (MM); (B) lamprey swimming like a mackerel (LM); (C) mackerel swimming like a lamprey (ML); (D) lamprey swimming like lamprey (LL), (Adopted from Borazjani et al. [10].

1.2.2 LEV Structure of finite-AR wings

With the intention of focusing more on the near surface flow of finite aspect ratio wings, the onset and development of the three-dimensional LEV was addressed recently from both experimental and computational perspectives. Yilmaz and Rockwell [82] considered unsteady plunging finite-AR plate, using quantitative imaging, showing the development of large-scale patterns of streamwise-oriented vorticity. They also performed dye flow visualizations as well as PIV measurements on a rectangular flat plate with angle of $\alpha = 8^o$, $St_c = 0.34$ and $h_o/c = 0.5$ (Figure 1.14). Strong axial flows were reported in the leading edge vortex, directed towards the symmetry plane of the wing. As the plunging motion progresses, the location of the transverse velocity maxima moves inboard.

Visbal [65] computed this sequence of flow patterns, and developed a model of the three-dimensional flow structure, which involves the evolution of an arch-type vortex. Figure 1.15(a) displays the structure of the computed arch-vortex using iso-surface of phase-averaged pressure. The corresponding computed flow structure on several cross-flow planes is also provided in Figure 1.15(a). Yilmaz, Ol and Rockwell [81] further characterized the types of three-dimensional vortex structures experimentally addressed by Yilmaz and Rockwell [82] and computed by Visbal [67]. Granlund, Ol and Bernal [29] used dye visualization and force measurements to determine the distinctions between rectangular versus elliptical planforms, in a pitch-up motion. Trizila et al. [63] considered the combined effects of the leading-edge vortex, tip vortices and a jet induced by vortices shed into the wake. They found that aerodynamic improvements depend on the kinematic parameters. Tip vortices evolve more slowly than leading edge vortices, where a tip vortex remains

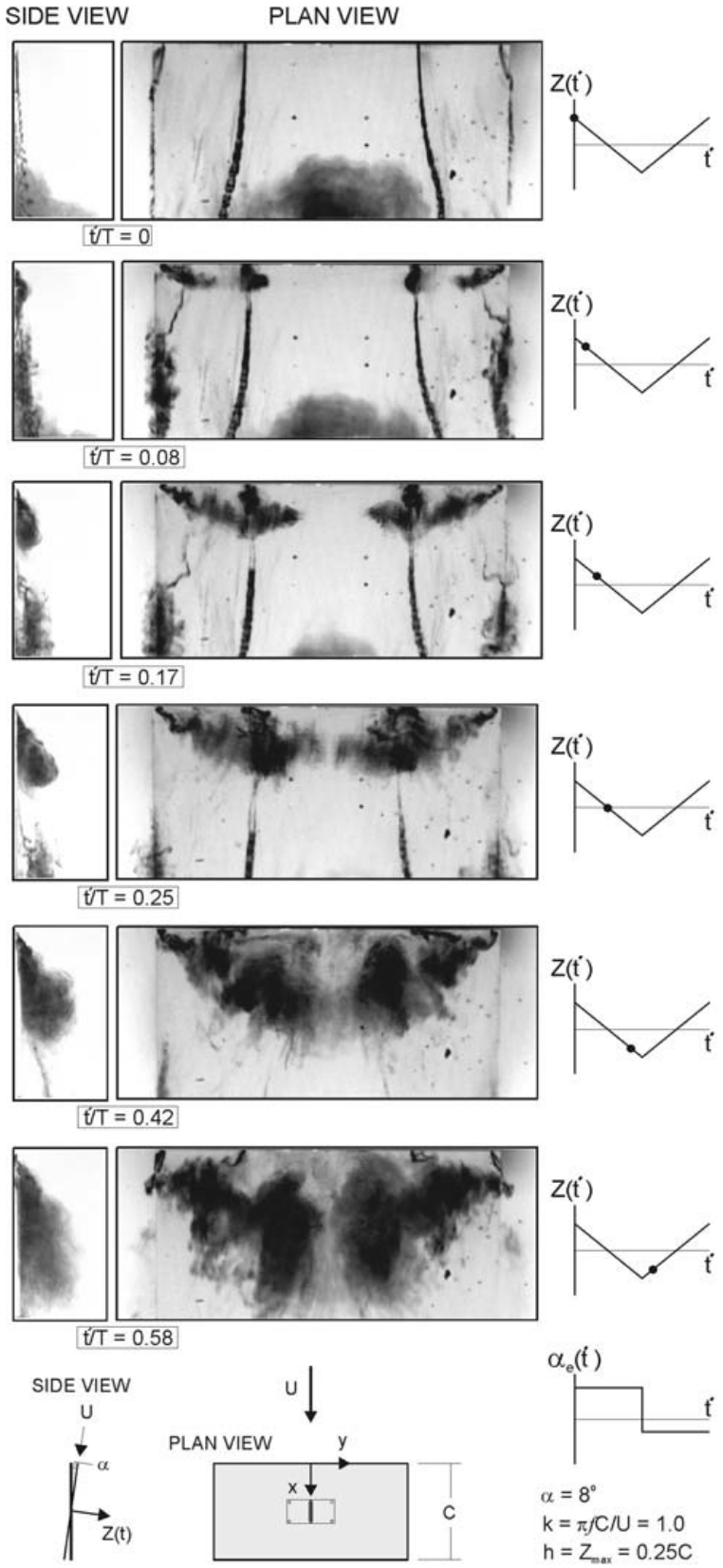

Figure 1.14: Dye visualization of three-dimensional vortex formation, (Adopted from Yilmaz and Rockwell [82]).

coherent and nearly attached to the wingtip until LEV detaches and sheds. As the reduced frequency is increased, maximum of lift is delayed to higher angles of attack shows less dependency on reduced frequency.

Volumetric three-component velocimetry measurements performed by Calderon et al. [15], on finite-AR rectangular and elliptical wings subjected to a small amplitude pure plunging motion with angle of attack of $\alpha = 20^o$. The highly three-dimensional leading edge vortex structure is shown to be highly dependent on the oscillating frequency. At low frequencies the vortex evolves quickly into an arch-type structure with an anchor point that progressively moves from the tip to the root of the wing. For the $sAR = 2$ they observed a full-arch on the half-span wing; however, a half-arch was detected on the half-span wing for $sAR = 1$ (Figure 1.16).

1.2.3 Spanwise Flow Within Shed Vortices

Spanwise flow in the LEV vortex structure can lead to a significant change in the vortex strengths. The contribution of spanwise flow to the LEV circulation is greater for three-dimensional flow. Koochesfahani [39] reported that there is an axial flow in the vortices in the wake of an oscillating airfoil with the walls at the end. Although, the wake is generated here by two-dimensional motions of a geometrically two-dimensional body, the resulting flow is not two-dimensional and an axial flow exists in the cores of the wake vortices. One might ask how this axial flow is created and how it would affect the LEV circulation. The axial flow takes the form of a spiraling of the vortex core fluid away from the channel side walls toward the channel centerline. Cohn and Koochesfahani [19] demon-

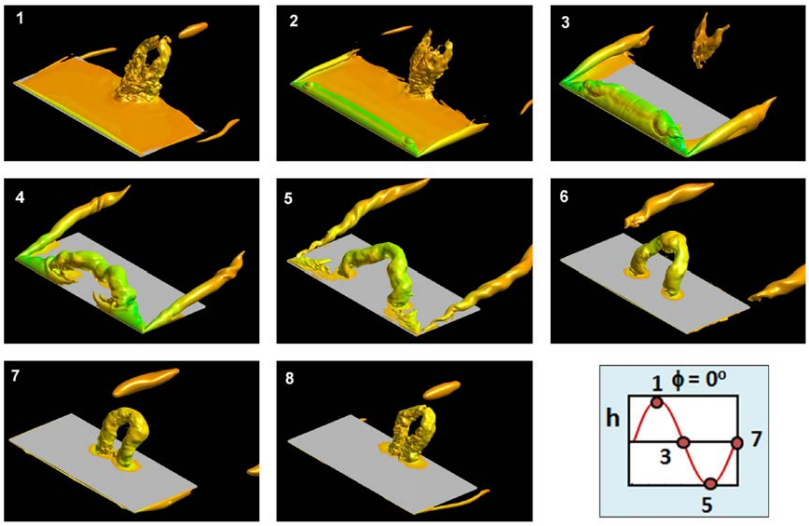

(a)

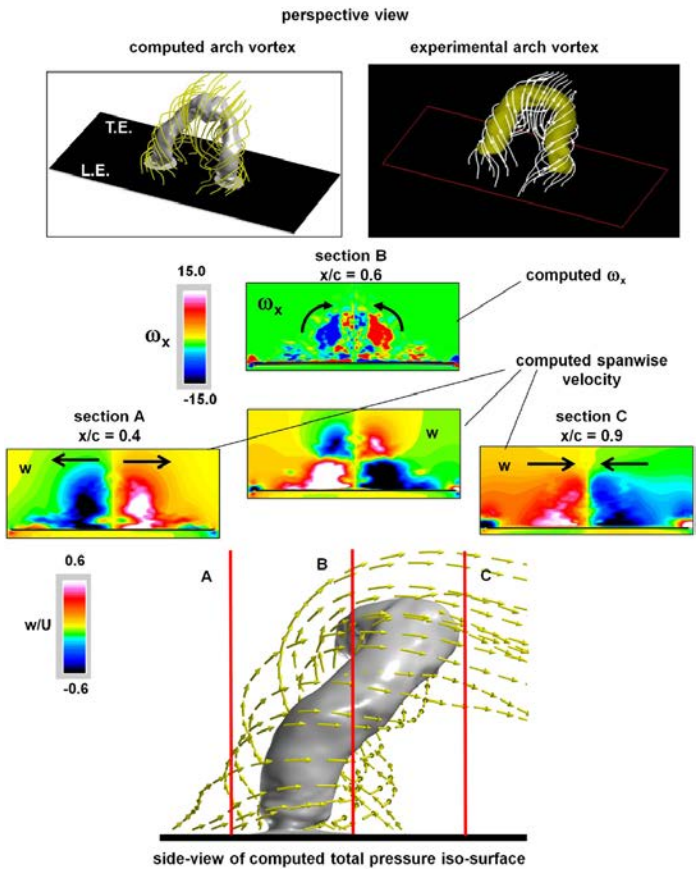

(b)

Figure 1.15: a) Iso-surface of computed phase-averaged total pressure at selected phases of the plunging motion, b) Perspective view of phase-averaged three-dimensional structure of arch-type vortex above heaving wing at $\phi = 225^{o}$, (Adopted from Visbal [67]).

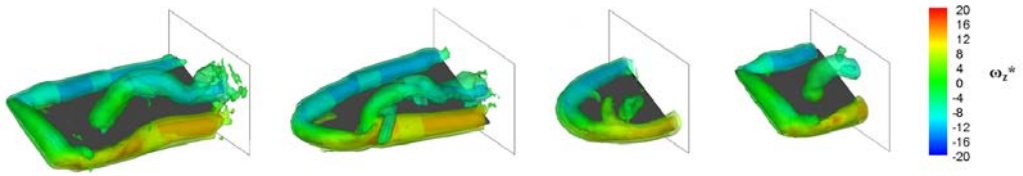

Figure 1.16: comparison between planforms for iso-surface of phase-averaged vorticity at St=0.6, (Adopted from Calderon et al. [15]).

strated that the end walls could generate substantial axial flow. The axial flow transports vorticity in and out of the plane and loses the coherency of the structure. These flows have been shown to alter vortex circulation, (Bohl and Koochesfahani [6, 7], Hagen and Kurosaka [31]). In a combined computational-experimental study, Visbal, Gogineni and Gaitonde [68] characterized axial flow in nominally spanwise vortices, and demonstrated that remarkably similar axial flows occurred for cases of either wall or free boundaries on either side of the wall jet. The physics behind this axial flow in a leading-edge vortex, during formation and development on the oscillating plate is still unclear, and has not been addressed in relation to the no-slip walls. Yilmaz and Rockwell [83] showed, for low-aspect-ratio wings, that the flow structure is highly three-dimensional, with pronounced regions of surface-normal vorticity and surface-parallel swirl that are orthogonal to the vorticity and swirl of the classical large-scale leading edge vortex. They described that there is an axial flow within the leading-edge vortex which is oriented towards the plane of symmetry of the wing, lifts up the structure from the wing surface and causes vortex distortion. Another important consequence of axial flow within the LEV is the interaction of

opposing axial flows at the plane of symmetry, which leads to the development of normal vorticity on both sidse of the plane of symmetry of the wing. This three-dimensionality has important consequences for the variation of spanwise vorticity of the leading-edge vortex along the span of the wing.

1.3 Objectives

The above discussion has demonstrated that our knowledge of vortex topology in three-dimensional unsteady wakes of plunging wings is still incomplete. While much is known about the vortex topology of these 2D and 3D flows, there is still not a framework for a robust model by which the complete vortex structure in the wake may be predicted, nor quantitative models for predicting the strengths of the various constituents of the wakes. Such quantitative models must take into account the effects of a) the nature of the shear layers shed from the edges of the wing or airfoil, b) interaction between the resulting flow structures and the surface of the wing or airfoil, and c) interaction between the structures. Two geometries are considered: a thin flat plate in nominally two dimensions, and thin flat plates of semi aspect ratios 1 and 2, in three dimensions. ”Nominally two dimensions” means that the model spans the water channel test section from wall-to-wall, with ideally a very small gap at the ends. Particle image velocimetry allows interpretation of the flow patterns in terms of phase-referenced wake patterns. Specifically, the objectives of the present investigation are as follows:

1. Describe the evolution of wake structures.

2. Characterize vortex interactions in the flow.

3. Demonstrate how LEV circulation varies with variation in parameters.

4. Elucidate the physical (vorticity transport) mechanisms that govern LEV circulation.

1.4 Overview of Thesis

In the present study, the flow dynamics for a simple plunging flat-plate airfoil fundamentally relevant to biologically-inspired micro air vehicle (MAV) aerodynamics is considered. Moreover, the evolution of the leading-edge vortices on a flat-plate airfoil and wing with a rectangular planform is characterizeed. In particular, Chapter 2 describes the experimental apparatus and PIV set ups used in this study. The airfoil geometries and kinematics and the parameter will be described. While it is well-established that the evolution of the leading edge vortex (and hence flow structure) and aerodynamic performance are controlled by a combination of reduced frequency and Strouhal number, the physical mechanisms governing the observed behaviors are not well-understood. Therefore, Chapter 3 seeks to characterize parameter dependence of the interactions between leading and trailing edge vortices and the forms of the resulting wakes, classification of observed wake patterns, as well as to identify the physical mechanisms governing these interactions. This is an important element of a framework for quantitative characterization of these wake structures. In chapter 4, we will focus on vorticity transport mechanisms present in the LEV which govern its evolution. Time-resolved and standard-frame-rate particle image velocimetry are used to qualitatively and quantitatively characterize the evolution of the leading edge vortex and its interaction with the secondary vortex generated on the plate surface. A planar control volume analysis is performed on the leading-edge vortex with

fluxes of circulation through the boundary quantified using PIV and streamwise measurements of the pressure distribution on the surface of the airfoil. 3-D flow evolution and vorticity transport analysis of finite-AR wings will be presented in chapter 5. Finally, the observations of this study and future works are summarized in Chapter 6.

CHAPTER 2
EXPERIMENTAL METHODOLOGY

2.1 Model Geometry and Kinematics

2.1.1 Parameter Space

To study the vortex characterization and circulation measurements of a rigid plunging wing, an aluminum flat-plate airfoil of chord length 76 mm and thickness 3 mm as shown in Figure 2.1 was articulated in a sinusoidal plunging motion:

$$h(t) = h_o sin(2\pi f t) \tag{2.1}$$

The leading and trailing edges were rounded with a constant radius of half the plate thickness, and the surface of the plate was painted black to minimize reflected light. Figure 2.2(a) shows the rigid airfoil that was used, and the whole mechanism together with other parts including holding bracket, mounting plate, and force transducer for force measurements purposes shown in Figure 2.2(b). Three plates were considered. The first, with an aspect ratio of 4 spanned the entire height of the flow facility to within 1 mm of the top and 2 mm of the bottom boundaries, and therefore is considered a nominally two-dimensional case. Two truncated plates were also considered with $sAR = 2$ and 1, as shown in Figure 2.3. Since the finite wing was bounded at its root by a stationary wall, this wall may be considered a symmetry plane such that the configuration approximates a symmetric wing with twice the aspect ratio. Thus, following the terminology applied by Calderon et al.[15] , we will refer to the geometry as having a semi-aspect-ratio $sAR = 2$.

Plunge position was monitored for external cyclic triggering of PIV data aquisi-

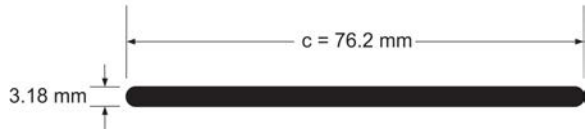

Figure 2.1: Cross-sectional shape of the plunging plate.

tion with a linear encoder having a resolution of 0.2 mm. The plunge amplitude and frequency of oscillation were adjusted to vary the dimensionless plunge amplitude h_0/c, and the Strouhal number $St = 2fh_o/U$ or reduced frequency $k = 2\pi fh_o/U$. Values investigated in this study were $h_0/c = 0.2$, 0.3, and 0.4, and $St = 0.1$ to 0.6 in increments of 0.1. This range of Strouhal numbers was chosen to bracket the range of Strouhal numbers relevant to biological locomotion [62, 59]. The resulting reduced frequencies were in the range $0.39 < k < 4.7$. For the finite-AR wings, the plunge amplitude was held constant at $h_o/c = 0.3$ and the frequency of oscillation was adjusted to control the Strouhal number St within the range $0.2 < St < 0.4$, which many flying and swimming animals employ; however, we will focus on $St_c = 0.2$ for the finite-aspect-ratio wings.

2.1.2 Apparatus and Water Channel

The motion was generated with a scotch yoke mechanism driven at constant speed by a a 24 VDC servo motor rated at 128 oz-in continuous torque at 380 rpm (Figure 2.4). The servo motor was driven by an Advanced Motion Controls model BE12A6J amplifier. For the 2D experiments, the amplifier was controlled by a constant analog voltage signal generated using a National Instruments USB-data acquisition board connected to a PC running National Instruments LabVIEW software. Later, for the finite-AR wings the motion

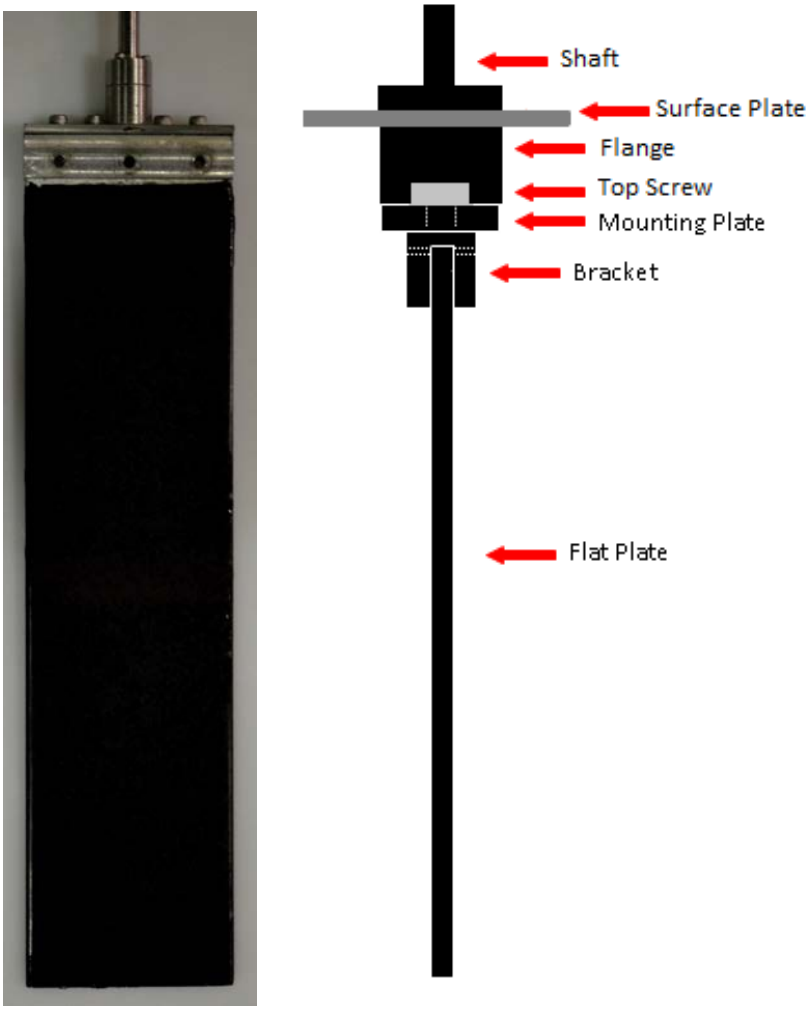

(a) (b)

Figure 2.2: a) Aluminum rigid airfoil, b) Parts of the mechanism which holds the rigid airfoil.

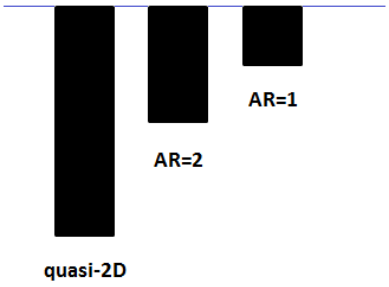

Figure 2.3: Plunging plates with different aspect ratios.

was controlled by a motion control system incorporating a Galil DMC-4040 controller, Emerson Control Techniques XVM-6011-TONS motor, and an Emerson EP-B amplifier.

Experiments were conducted in a free-surface water channel with test section width of 0.61 m, and a water depth of 0.33 m. The free surface was constrained between 0.6 m upstream and 0.6 m downstream of the airfoil by rigid plates at the water surface as illustrated in Figure 2.8. The flow facility has flow conditioning consisting of an 8:1 contraction ratio, honeycomb, and five screens to maintain free stream turbulence intensity below 0.3%. Free-stream velocity is held constant at $U_\infty = 0.13$ (m/s) for all experiments, producing a chord-based Reynolds number of $Re_c = 10,000$.

2.1.3 Root Boundary Conditions

To examine the influence of the root boundary condition two different boundary conditions were examined. The first root boundary condition considered as shown in the right side of Figure 2.5 is that of the water channel surface plate. Figure 2.6 illustrates the location of surface plate with respect to the apparatus and the driving shaft. There is

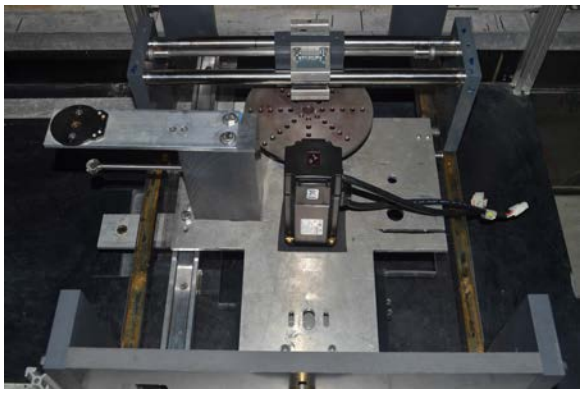

Figure 2.4: Top view of the scotch yoke mechanism.

a slot on the surface plate as wide as the largest plunging amplitude in which the driving shaft is moving back and forth. The slot has a Rectangular shape with rounded edges with 76.2 mm length and 25 mm width. There is a gap of approximately 6 mm between the top of the mounting bracket and the water surface plate to accommodate the heads of screws used to assemble the bracket. Second, a circular *root* plate was fixed perpendicular to the wing, as shown in the left side of Figure 2.5 in order to create a well-defined boundary on both top and bottom surfaces of the wing. The root plate shape is based on a design proposed by Boutilier and Yarusevych [11] for wind tunnel investigations of steady airfoil aerodynamics. In the absence of similar guidelines for plunging plates, this geometry was adopted for the present study. The gap between the root plate and top surface plate is 38 mm which is beyond the boundary layer thickness ($\delta = 20mm$).

Since the root plate has not been examined on moving bodies yet, therefore, the effects of moving root plates on vortex structures is still unclear. To reduce the effects of root boundary conditions on flow evolution and avoid the inflow and outflow from the slot

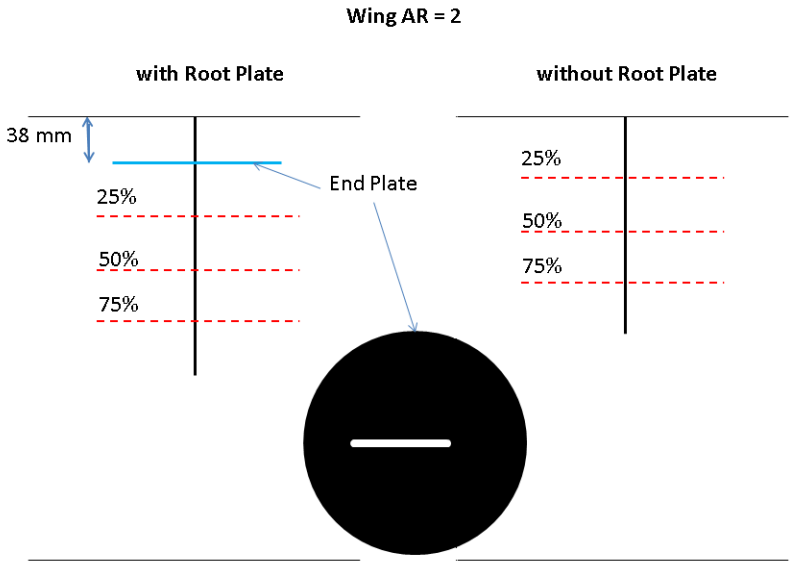

Figure 2.5: Two boundary conditions for the plunging plate with $sAR = 2$ with and without root plate.

on the surface plate, the gap between the top of the bracket (which mounted the airfoil or wing to the scotch yoke mechanism) and the surface plate has been minimized (by using countersunk screws) to less than 1 mm as shown in Figure 2.7. Similarly, a gap of less than 3 mm existed between the bottom of the airfoil and the bed of the water channel. For the 3-D volume reconstruction results in this study, this root boundary condition was used and the spanwise locations are measured with respect to the top of the holding bracket.

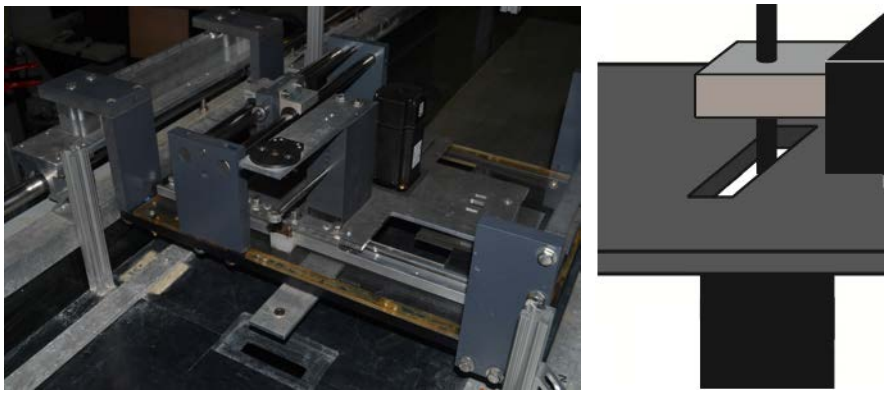

(a) (b)

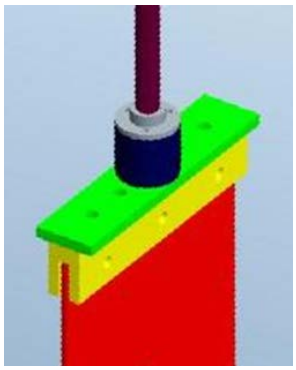

(c)

Figure 2.6: Boundary condition 2: a) Surface plate with the mounting bracket outside of the slot, b) Driving shaft in the slot of surface plate, c) Plunging plate with driving shaft and holding bracket outside of the slot.

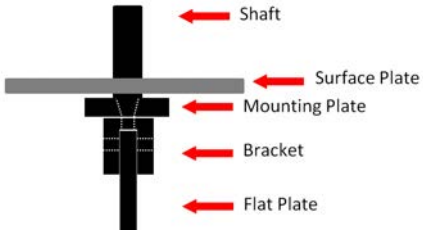

Figure 2.7: Details of the airfoil and wing modified mounting bracket.

2.2 Experimental Techniques

2.2.1 2-D Digital Particle Image Velocimetry (PIV) Setup

Digital Particle Image Velocimetry (DPIV) is a statistical Lagrangian method that estimates particle displacements between two consecutive images in a fluid flow to provide a representative velocity field in a plane (Adrian (2005), Raffel et. al. (2007), and Tropea et. al. (2007)). Potters Industries Inc.'s SPHERICEL® Hollow Glass Spheres were used to seed the flow. The particles had a mean particle diameter of 10-11 μm with a density of 1.1 g/cc. These particle properties corresponded to a Stokes number (Stk = $(\tau U_{tip})/c$; where τ is the relaxation time of the particles and U_{tip} and c are the plate tip speed and chord length, respectively.) of 8.5×10^{-4} which suggests the particles follow the streamlines very well and since Stk <0.1, the deviation of the particle trajectories from the actual flow displacements is <<1% (Tropea et. al. (2007)).

Two-component Digital Particle Image Velocimetry (DPIV) was applied as shown in Figure 2.8. A LaVision Flowmaster system was employed, running DaVis 8.0.6. Images were acquired with a 14-bit Imager ProX 4 megapixel CCD camera and 2048 × 2048 pixel resolution equiped with a Nikon Micro-Nikkor 105 mm f/2.8 lens (Figure 2.9(a)), and illuminated using a 200 mJ/pulse dual-cavity Nd:YAG laser (Figure 2.9(b)). Velocity vectors were calculated using an adaptive multi-pass cross-correlation method on 64 × 64 and 32 × 32 pixel interrogation windows with 50% overlap. Spurious vectors are removed using a local median filter. Out-of-plane vorticity was calculated using a second-order central differencing scheme.

Data presented in this study consists primarily of PIV velocity fields, each com-

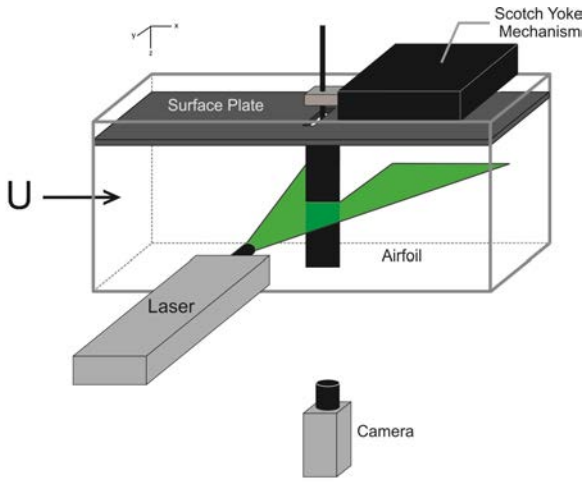

Figure 2.8: Side view of the experimental configuration. The plate plunges in and out of the page.

posed of 100 instantaneous realizations of the flow, processed by DaVis 8.0.6. software. The cameras were triggered using a US Digital EM1 Transmissive Optical Encoder Module and a 120-counts-per-inch linear encoder strip that was mounted to the scotch yoke. The velocity field was sampled at eight phases throughout the cycle separated by 45° increments. Eight phases were imaged for each of the cases are: $\phi = -90°, -45°, 0°, 45°, 90°, 135°, 180°,$ and 225°. The position $\phi = 0°$ is defined as the mid-point during the downstroke (where the downstroke is defined as that in which the wing moves away from the laser).

2.2.2 3-D Stereoscopic Digital PIV Setup

In selected experiments on the $sAR = 1$ and 2 finite wings, Stereoscopic Particle Image Velocimetry (SPIV) was implemented to obtain a three component velocity field at selected chordwise planes, as illustrated in Figure 2.10(a). A LaVision Flowmaster system

(a)

(b)

Figure 2.9: a) 14-bit Imager ProX 4 megapixel CCD camera, b) 200 mJ/pulse dual-cavity Nd: YAG Laser used for PIV.

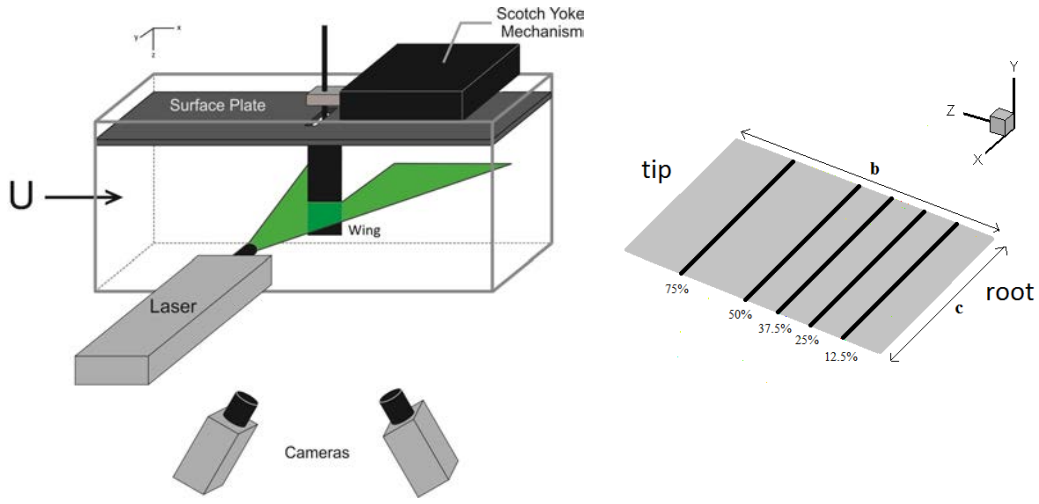

(a) (b)

Figure 2.10: a) Coordinate system b) Side view of the experimental configuration, the plunging plate moves in and out of the page.

was used which consisted of a dual cavity, 200 mJ/pulse Nd:YAG laser with light sheet optics and two CCD cameras with 2048 × 2048 pixel resolution with a 14-bit dynamic range, equipped with two 105 mm lenses placed at 54 degrees to each other with f-stop equal to 8.0. Velocity vectors were computed using LaVision DaVis 8.1.2 software with a standard cross-correlation analysis on window sizes of 64 × 64 and 32 × 32 and 50% overlap. A median filter was applied to remove any outliers. The experiments were performed on different spanwise locations as a percentage of the span length as shown for $sAR = 2$ in Figure 2.10(b). For example, 25% means the experiments were performed at $z/b = 0.25$ from the root boundary.

2.2.3 2-D Time-Resolved Digital PIV

Time resolved PIV was performed in order to better resolve the LEV formation and interaction with the airfoil. An IDT NX4-S1 1.0 megapixel high speed camera with 1024 $\times$ 1024 pixel resolution (shown in Figure 2.11(a)), equiped with a 50mm Micro-Nikkor lens, was used to image the full oscillation. The size of correlation windows was 32×32 and 32×32 pixel interrogation windows with 50% overlap.The camera's exposure time was 692 μs and images were usually taken at a rate of 800 frames-per-second where the number of frames per cycle was varied between 400 and 1900. If, however, the frequency of the motion was very high, the frame rate was increased to better discretize the motion and obtain more accurate cross-correlation measurements. As a general rule of thumb, the frame rate was set so that particles would travel about 4-6 pixels from one frame to another. A Laserglow Technologies LRS-0532 Series Diode-Pumped Solid-State Laser (532nm, green) continuous waveform laser, shown in Figure 2.11(b), was used to image the mid-span location and in order to prevent the interference of parallax on the imaging area, the camera was offset from the centerline so that it always had a direct view of the airfoil's side closest to the laser. Thirty full cycles were performed for each case, processed by DaVis 8.1.2. software using time-series images, and averaged at each phase.

2.2.4 2-D PIV Setup for 3-D Volume Reconstruction

In order to analyze vorticity transport within the leading-edge vortex, the phase-averaged flow field was measured within a three-dimensional region to capture the vorticity field and its derivatives. Use of stereo PIV was impractical for this purpose since data

(a) (b)

Figure 2.11: a) IDT NX4-S1 high speed camera, b) DPSS continuous waveform laser.

acquisition in multiple parallel planes would require a complicated refocusing and recalibration procedure at each plane, while imaging obliquely through a surface across which the refractive index changes. Therefore, planar PIV data for three-dimensional flow field reconstruction were acquired in multiple horizontal and vertical planes using the camera and laser configurations illustrated in Figure 2.12. Vertical (y-z) planes were acquired with the aid of a front-surface mirror of dimensions 75 x 75 mm suspended at a 45 degree angle in the flow approximately 1.5 m downstream of the trailing edge of the airfoil or wing (similar configuration as used in the experiments by [32], [13], [14]). As shown in 2.12(a), the laser was laid down on a platform underneath the flume and to do the experiments at different streamwise locations, The plunging wing mechanism was moved in the streamwise direction (x-direction) and positioned with the aid of a digital caliper. For this configuration, since the PIV setup was not changed during the experiments and only the apparatus was relocated in the x-direction, recalibration was not required.

For the horizontal planes ($x - y$ planes), the configuration shown in Figure 2.12(b)

was used where the cameras and the laser were moved separately in spanwise direction (z direction), checking their positions with a digital caliper to accurately position the mechanism relative to a fixed reference point, so that the distance between laser and camera does not change. Note that only for the PIV measuments in $x-y$ planes, two adjacent cameras were used simultaneously to expand the field of view to about 5 chord lengths, including the region over the wing as well as multiple chord lengths into the wake. The calibration process will be discussed in section 2.2.4.1.

Three-dimensional flow fields were reconstructed on the two-dimensional airfoil and the $sAR = 2$ wing. The vertical and horizontal separation between planes was 6.4 mm ($\Delta z/c = \Delta x/c = 0.08$). For the airfoil, measurements were acquired in 13 horizontal planes, and 40 vertical planes beginning 25 mm upstream of the leading edge. The volume construction technique, described in the following, yielded 425984 vectors. For the finite-aspect-ratio wing, 26 horizontal planes of data were acquired beginning at $z/S = 0.15$ ($0.15S$ from the root of the wing, where S is the span (i.e. for the $sAR = 2$ wing, S is equal to two chord lengths.)).

2.2.4.1 Calibration

To accurately calibrate the horizontal planes ($x-y$ planes), a calibration mechanism was designed and built as shown in Figure 2.13. In this mechanism, the calibration plate was attached to a 1" diameter Stainless Steel horizontal shaft which was mounted on two 1" diameter Stainless Steel vertical shafts using two stanchion cross clamps as shown in 2.13(d). These two vertical shafts were mounted on a horizontal Acrylic plate and the

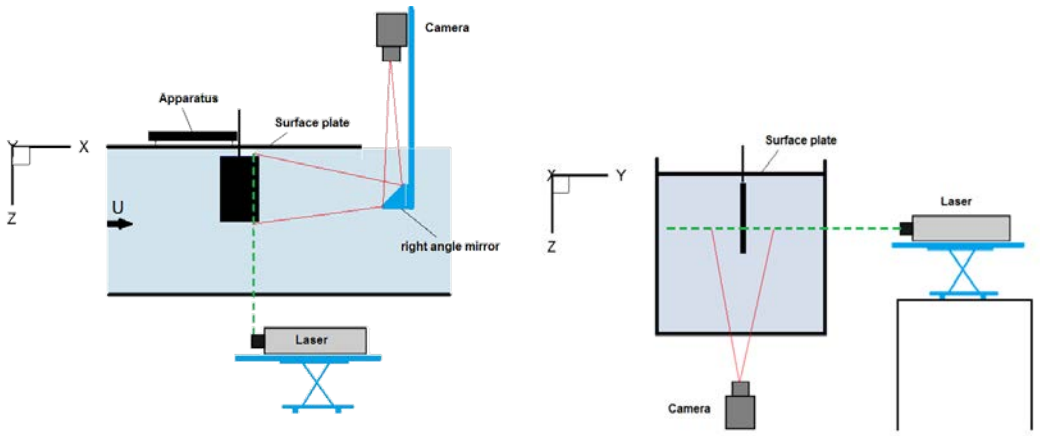

(a) (b)

Figure 2.12: Imaging configuration for PIV measurements. (a) side view showing the setup for acquiring images in vertical/transverse planes, (b) upstream view showing the setup for acquiring images in horizontal planes.

calibration mechanism was carefully laid down on the bed of flume at the same spot, so the reference point was at the same location for all calibration planes in z direction. The height of the calibration plate was adjusted by using custom-made gauge blocks, thus the position of this calibration plate was matched with the laser sheet at each spanwise location.

Since in this PIV setup two adjacent cameras were used, the key was calibrating each camera properly, so that the coordinate system of each camera could be properly registered. This was accomplished using the ”2 cameras (independent)” calibration mode in DaVis 8.1.2 with an orthogonal grid target that covered the field of view of both cameras. A LaVision calibration plate type 20 (Figure 2.13(c)) spanned the fields of view of both cameras. After calibrating both cameras in their respective co-ordinate systems, an origin was defined, and the relative x and y off-sets for Camera 2 were set with respect to the

origin in Camera 1. For processing the images, the ”Sequential Cross correlation” mode in DaVis 8.1.2 was employed to produce a single vector field spanning the two fields of view. Since the calibration was of high quality, the root-mean-square (RMS) of the fit for pixel displacement was 0.106 pixels.

2.2.4.2 3-D Volume Reconstruction

In order to obtain volumetric representations of the three-dimensional flow field, Yilmaz and Rockwell [54] demonstrated that it is sufficient to have data in parallel planes and one cross-plane as shown in Figure 2.14. They computed the out-of-plane component of velocity for each parallel planes using the two in-plane components v and w and the continuity equation for an incompressible flow as discussed in their study. Two interpolation methods (Adaptive Gaussian Window and the Spline Thin Shell (STS)) were used and they showed that the the STS technique provides a more faithful reconstruction of the actual value of the out-of-plane velocity component. They also mentioned that the in-plane interpolation of the velocity field can lead to substantial uncertainty of the interpolated values, in the case of randomly located velocity vectors, which emphasizes the importance of employing high quality experimental techniques that generate high particle image density. Later Yilmaz and Rockwell [83] used this method to investigate the 3-D flow evolution of flapping wings. They used Tecplot software (Tecplot, Inc., Bellevue, WA) for the linear interpolation as well as in-house developed software for the uncertainty analysis involving in the interpolation and volume construction technique. They reported that for the parameters employed in the their investigation, the representative uncertainty of the reconstructed

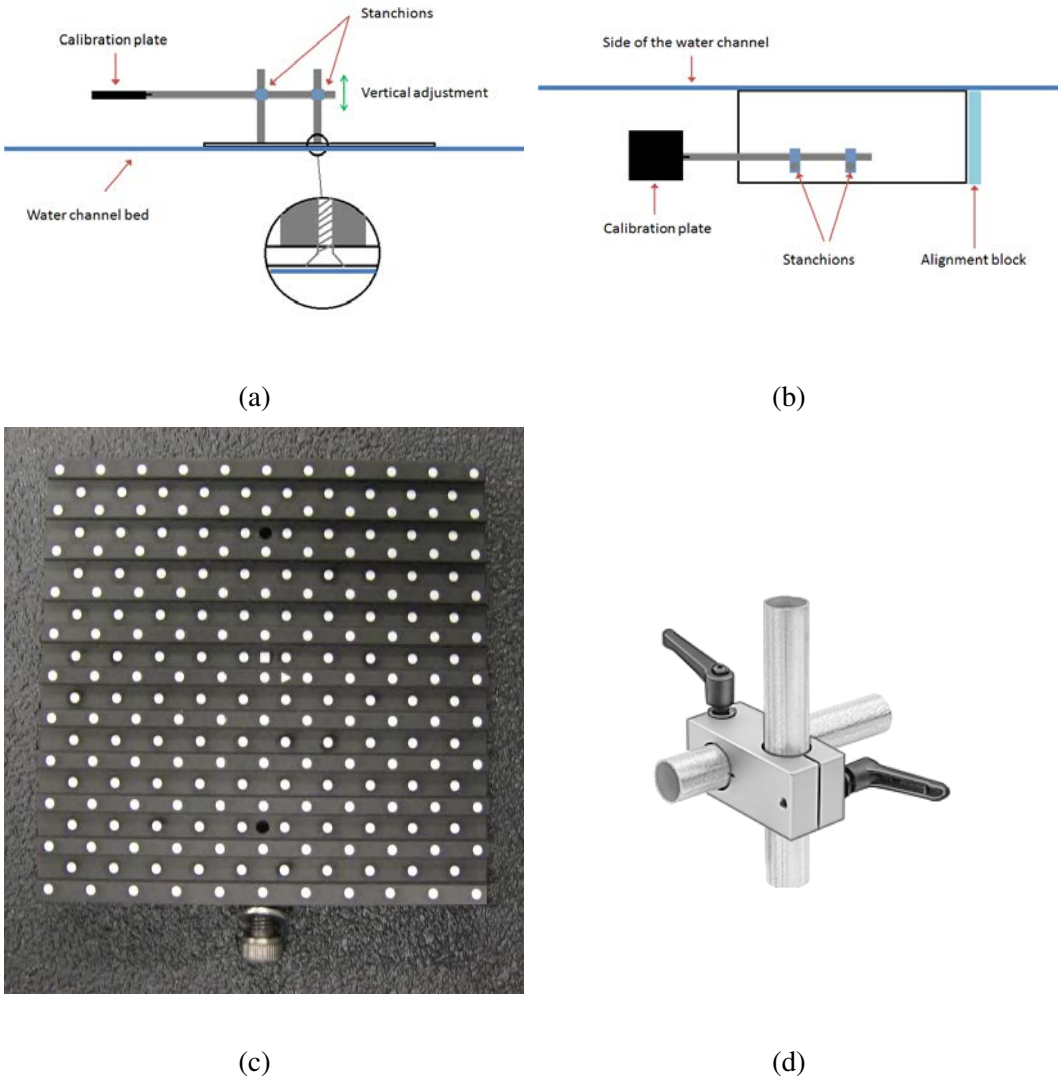

(a) (b)

(c) (d)

Figure 2.13: Calibration mechanism for 2-D PIV measurements for the 3-D volume reconstruction. (a) side view of the mechanism, (b)top view of the mechanism, (c) LaVision calibration plate type 20, (d) Stanchion cross clamps used to hold horizontal and vertical shafts.

velocity was 0.4%.

Longo et al. [44] conducted PIV measurements in multiple vertical and horizontal planes and used Tecplot software package to generate the 3-D rectangular grid and linearly interpolate the 2-D data onto this grid. Once all of the data from both PIV configurations (vertical and horizontal planes) was interpolated onto this common grid, they computed an average from the redundant velocity field data to represent the 3-D information at each grid point.

In the present study, high resolution PIV measurements with high density of 2-D images in the desired volumetric flow field were conducted and high-order interpolation method were used to reduce the uncertainties in the reconstruction. Using the two-dimensional phase-averaged velocities in streamwise and transverse cross-flow planes, volumetric reconstructions of the flow field were obtained by emplying a code written in MATLAB. Reconstruction of the PIV data was accomplished using tri-quadratic interpolation onto a uniform grid of spacing $\Delta x/c = \Delta y/c = \Delta z/c = 0.0195$, as shown in Figure 2.15. The interpolation method and formulations are described in Appendix B. The final grid size was $128 \times 101 \times 51$ for the airfoil and $200 \times 128 \times 100$ for $sAR = 2$ wing. The 3-D volume reconstructed velocity field was validated by checking the differences of the redundant cmponent of velocity (U_y) between horizontal and vertical planes and also examining the divergence of the reconstructed flow field as discussed in 4.1.2.

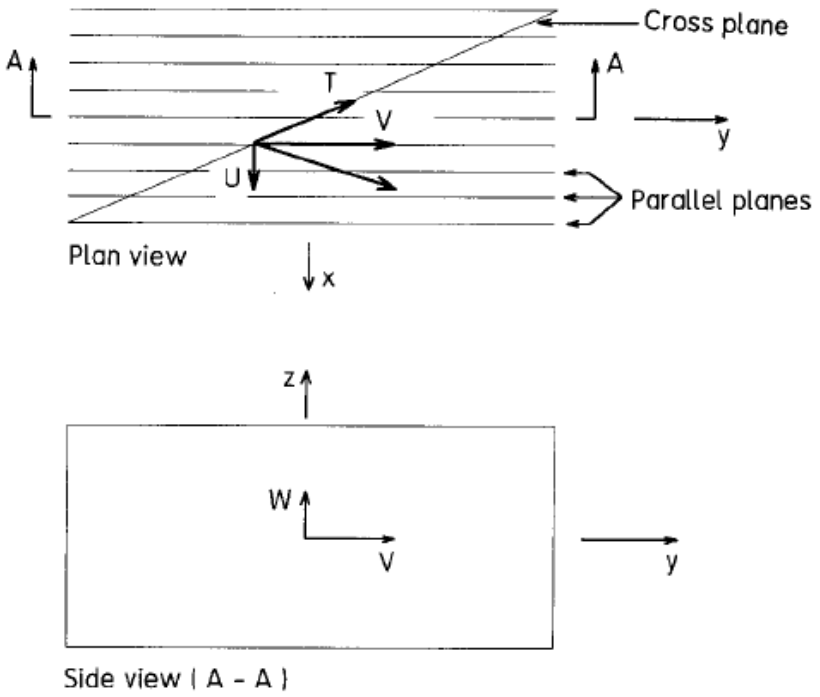

Figure 2.14: Plan and side view of the parallel and transverse planes of 3-D reconstruction by Robinson and Rockwell [54]. The coordinate system and the corresponding velocity components are illustrated.

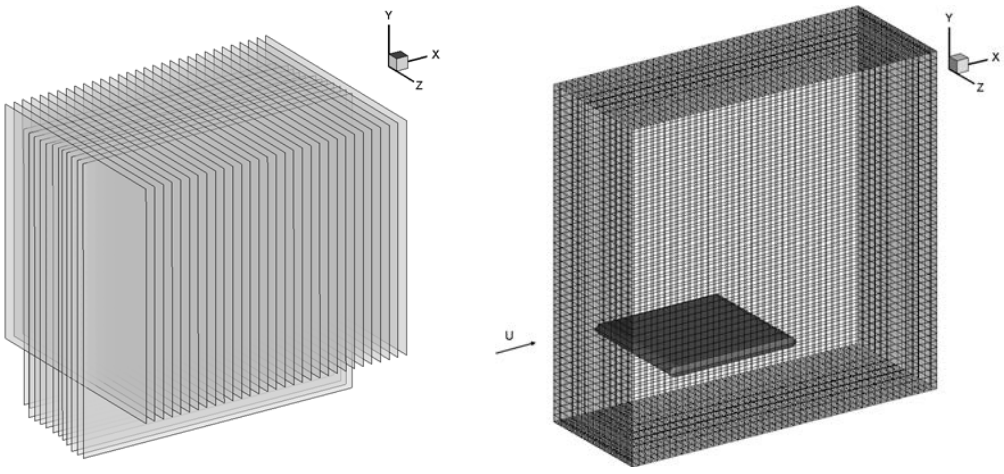

(a) (b)

Figure 2.15: a) Horizontal and vertical PIV planes, b) The flow volume reconstructed from horizontal and vertical PIV planes. The orientation of the reconstructed data is such that the laser-illuminated region is above the plate, and the plate casts a shadow in the region beneath it.

2.2.5 Surface Pressure Measurements

Phase-averaged pressure measurements were conducted by James Akkala [12] on the surface of the airfoil using flush-mounted pressure taps in order to estimate the vorticity flux from the surface of the wing due to the pressure gradients set up by the leading-edge vortex. Pressure taps of diameter 1.6 mm (1/16”) were mounted around the mid-span location of the airfoil, beginning at 3.2 mm from the leading edge with chordwise spacing of 1.6 mm over a chordwise distance of 22.2 mm (7/8”), and with chordwise spacing of 6.4 mmm (1/4”) over the remainder of the chord length, as shown in Figure 2.16. Surface pressures were measured through one tap at a time with a Kistler 4264A piezoresistive differential pressure transducer, with the remaining taps filled flush to the airfoil surface, and

phase-averaged over 50 oscillation cycles. Because the plate was thin, the pressure measurement tube emerged from the opposite side of the plate. One of the key objectives of this study is to quantify the fraction of circulation entrained into the leading edge vortex from the leading edge shear layer that is lost by annihilation through interaction of the leading-edge vortex with the secondary (opposite-sign) vorticity generated on the surface of the plate. It is important to characterize the dynamic response of the pressure transducer since the pressure is fluctuating and the resonant frequency of the pressure transducer system is significantly lower in water than it is in air. To determine the frequency response of the pressure transducer and attached tubing, the apparatus shown in Fig. 2.17(a) was used. The sealed canister sustained a pressure in a water environment so that the pressure transducer and tubing can be filled with water simulating the experimental measurement environment. A syringe was used to inject air into the canister in order to increase the pressure, and a bubble positioned on top of a hypodermic tube sustained the pressure. Bursting of the bubble created a step function in pressure. The step response of the pressure transducer was used to determine the transfer function of a second-order linear system as done by Green and Smits [30]. Fig 2.17(b) shows the signal produced by the Kistler pressure transducer along with the model response, and Fig. 2.17(c) contains the resulting bode diagram. For the present configuration, the undamped natural frequency was found to be $\omega_n = 48.9 rad/s$ and the damping ratio was $\zeta = 0.235$.

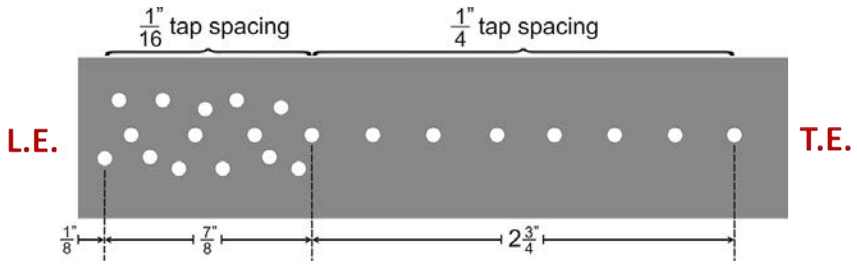

Figure 2.16: Locations of pressure taps on the surface of the airfoil. A narrow spanwise slice of the airfoil is shown.

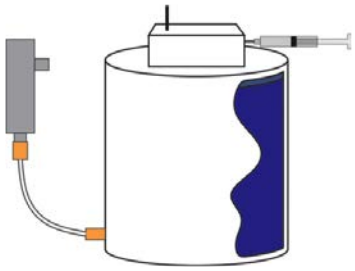

(a)

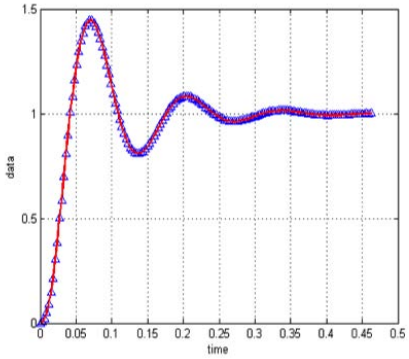

(b)

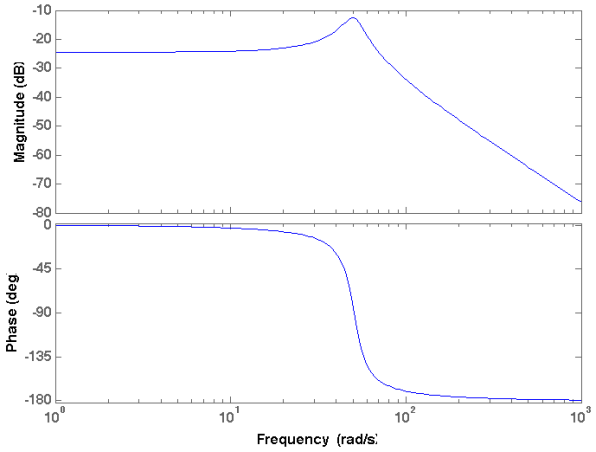

(c)

Figure 2.17: a) Apparatus for determination of pressure measurement system frequency response, b) step response of the Validyne DP-103 pressure transducer. Symbols show the pressure transducer output signal, and the line shows the optimum second-order model response. c) Bode diagram for the model response shown in Fig. 2.17(b).

CHAPTER 3
FLOW EVOLUTION FOR A NOMINALLY 2-D PLUNGING AIRFOIL

3.1 Vorticity Distributions Near the Airfoil

The evolution of the flow field with variation in Strouhal number, plunge amplitude, and phase is shown in Figs. 3.2 through 3.15. The wake structures was visualized by the spanwise vorticity distribution and the the integral Γ_2 parameter as an alternative and somewhat objective means of identifying vortex boundaries, which was independently developed by Graftieaux et al. [28] and Sousa [57]. The Γ_2 field is defined as:

$$\Gamma_2(P) = \frac{1}{N} \sum_{S} \frac{\left[PM \wedge (U_M - \bar{U}_P)\right] \cdot z}{\|PM\| \cdot \|U_M - \bar{U}_P\|} \tag{3.1}$$

where P is a fixed point, and M is a point within a two-dimensional area S surrounding P, and N is the number of points M within the area. U_M is the velocity vector at the point M, and z is the unit vector normal to the imaging plane. For each point P, the eight neighboring points were used to compute the Γ_2 fields, as recommended by Baik et al. [4]. Graftieaux et al. [28] recommended a threshold of $\Gamma_2 = 0.65$ to define vortex boundaries, and showed that the Γ_2 field displays approximately an axisymmetric top-hat distribution in the vicinity of a vortex such that the boundary is quite insensitive to the value of the threshold. Since the denominator of Equation 3.1 is very small where the streamlines have small curvature, the Γ_2 field tends to be noisy in the irrotational regions of the flow. To remove this noise,

A version of this Chapter has been published in Experiments in Fluids Journal [23].

the Γ_2 calculation was modified by setting to zero the values in the regions where the vorticity magnitude was less than a threshold of 4 s^{-1}. Leading-edge vortex trajectories were obtained by tracking the point of maximum vorticity magnitude.

The flow is characterized using isocontours of vorticity (filled color contours) with superimposed contours of $\Gamma_2 = \pm 0.65$ (black lines). Red shades indicate positive (counter-clockwise) vorticity, and blue shades indicate negative (clockwise) vorticity. Solid contours of Γ_2 represent positive values and dashed lines represent negative values, which correspond to the sign of the vorticity contained within the contour. The contour legend shown in Fig. 3.2 applies to all of the vorticity contour plots presented in this paper.

Typical uncertainty of the in-plane velocity components (u and v) was approximately 2% while typical uncertainty in the out-of-plane of vorticity (ω_z) were estimated to be 3%. The uncertainties in the velocity and vorticity are based only on PIV measurement error, assuming a typical 0.1 pixel uncertainty in the displacement computed from the cross-correlation analysis (e.g. Huang et al., 1997; Westerweel, 2000). The 2% velocity uncertainty is based upon the free-stream velocity, and the 3% vorticity uncertainty is obtained by propagating the velocity uncertainty through the central difference equation used to compute the vorticity field, and evaluating at a typical peak vorticity value in the LEV, assuming that the uncertainty is dominated by random errors. A detailed discussion on error analysis is presented in Appendix A. Random measurement errors should decrease as $1/\sqrt{N}$ when averaging over N velocity fields; however, the flow field variability in this transitional flow is generally much greater than the measurement uncertainty. To estimate convergence of the mean as it relates to the present study, we considered the leading-edge

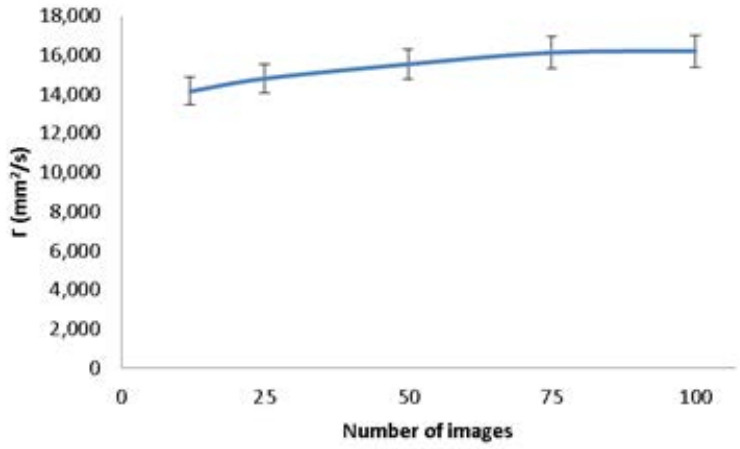

Figure 3.1: Small uncertainty in circulation by taking average of 12, 25, 50, 75, and 100 images for circulation measurements.

vortex circulation in the mean flow with increasing numbers of velocity fields in the average which shows that convergence is achieved with 100 velocity fields as shown in Figure 3.1.

3.1.1 Overview of Flow Evolution: $St = 0.2$

To provide a baseline for the investigation of parameter variations, Fig. 3.2 shows the evolution of the vorticity distribution generated by the plunging plate for $St = 0.2$ and $h_0/c = 0.3$, which corresponds to $k = \pi/3 = 1.05$. At the top of the downstroke (Fig. 3.2(a)) the vorticity field downstream of the panel consists of multiple clockwise vortex structures, as indicated by the Γ_2 contours (which match well with local vorticity concentrations). The compact discrete vortices were shed from the trailing edge throughout the preceding upstroke, and the large, diffuse structure is the leading edge vortex generated

one full cycle earlier during the preceding downstroke. Despite that the vorticity shed from the leading edge sometimes forms more than one vortex, and that from the trailing edge often resembles an unstable shear layer rather than a single discrete vortex, we will use the abbreviations LEV and TEV to denote the vortex systems shed from the leading and trailing edges, respectively. Figure 3.3 showes the velocity vector fields for the same case with $St = 0.2$ and $h_0/c = 0.3$ which are the zoomed-in pictures of pictures in Figure 3.2.

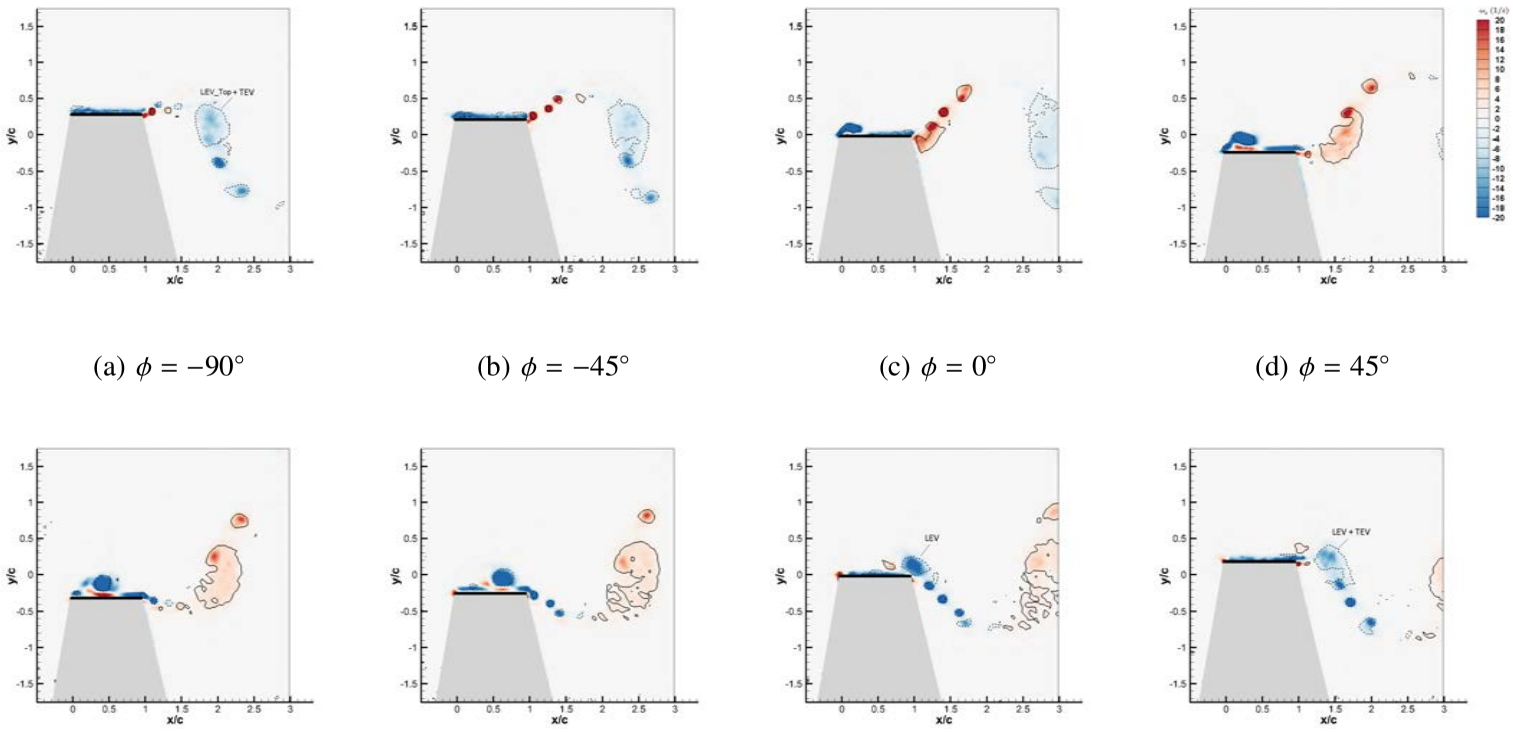

(a) $\phi = -90°$ (b) $\phi = -45°$ (c) $\phi = 0°$ (d) $\phi = 45°$

(e) $\phi = 90°$ (f) $\phi = 135°$ (g) $\phi = 180°$ (h) $\phi = 225°$

Figure 3.2: Evolution of spanwise vorticity with phase for $St = 0.2$, $h_0/c = 0.3$, $k = 1.05$.

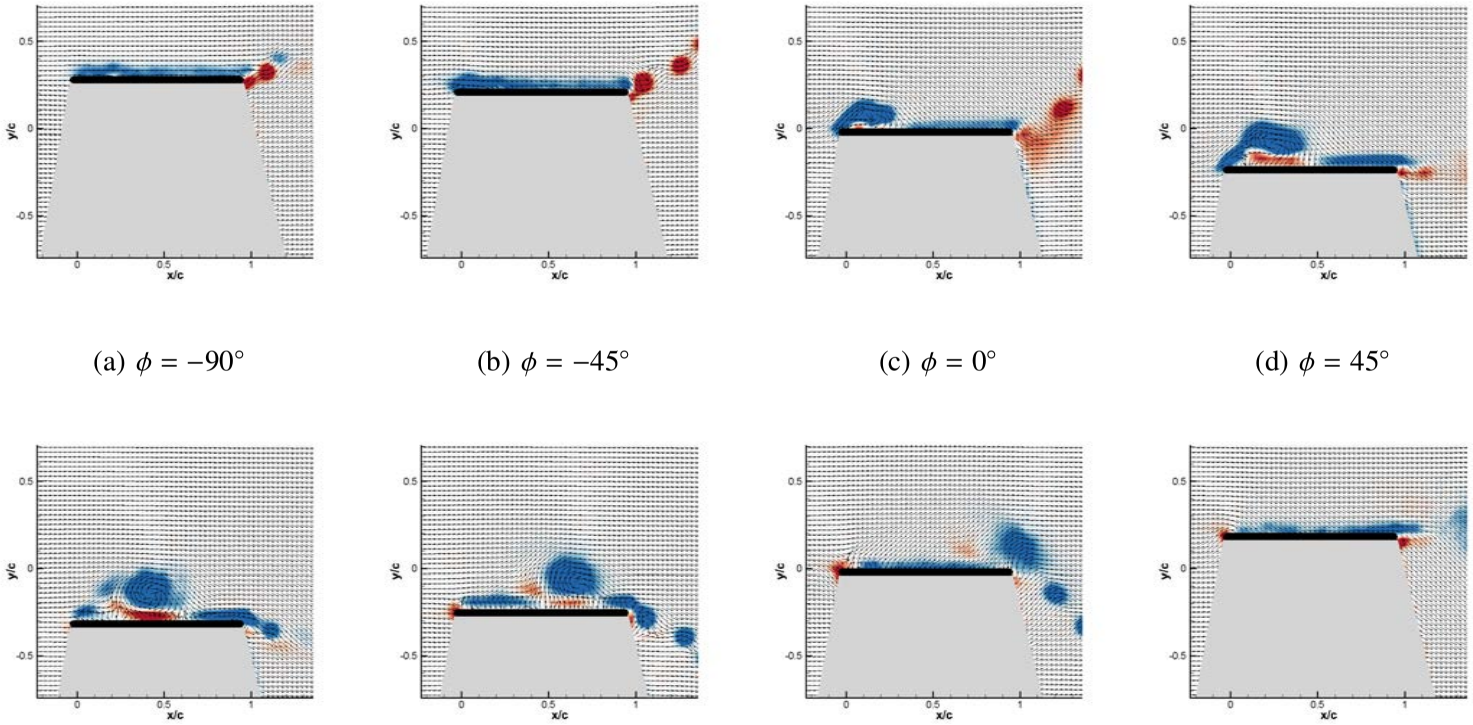

(a) $\phi = -90°$ (b) $\phi = -45°$ (c) $\phi = 0°$ (d) $\phi = 45°$

(e) $\phi = 90°$ (f) $\phi = 135°$ (g) $\phi = 180°$ (h) $\phi = 225°$

Figure 3.3: Evolution of spanwise vorticity with phase combined with velocity vector fields for $St = 0.2$, $h_0/c = 0.3$, $k = 1.05$.

Early in the downstroke, (Fig. 3.2(b)), multiple new counter-clockwise vortex structures are similarly shed from the trailing edge until $\phi \approx 0°$, where the counter-clockwise LEV beneath the plate (not yet visible) reaches the trailing edge. The initiation of LEV generation on the top surface begins somewhat later than shedding of vorticity from the trailing edge, as it is first clearly present at $\phi = 0°$. Interaction between the LEV and the top surface of the plate results in the generation of a region of counter-clockwise vorticity between the LEV and the plate. As previously observed by Lewin and Haj-Hariri [43], in the phase-averaged representation of the flow this counter-clockwise vorticity appears to participate in the separation of the LEV from the shear layer as it is drawn forward and ultimately penetrates the shear layer. This is illustrated in Figs. 3.2(d) through 3.2(f).

Experiments were repeated at $St = 0.2$, with values of $h_0/c = 0.2$ ($k = \pi/2 = 1.57$) and 0.4 ($k = \pi/4 = 0.785$). Selected phases are shown in Fig. 3.4, which demonstrates that the number of discrete structures shed from the trailing edge increases with plunge amplitude. In both cases, the evolution of the flow field was qualitatively similar to that at $h_0/c = 0.3$; however, the convection rate of the LEV ($d(x_c/c)/d\phi$, where x_c is the streamwise position of the vorticity peak in the LEV) is positively correlated with plunge amplitude. The nature of interactions between leading- and trailing-edge vortices are therefore primarily dependent on the plunge period at $St = 0.2$ without significant influence of the plunge amplitude, implying that vortex interactions are primarily dependent on reduced frequency.

For all of the amplitudes investigated at $St = 0.2$, the LEV convects over the full chord length and interacts with trailing-edge structures shed during the subsequent strokes.

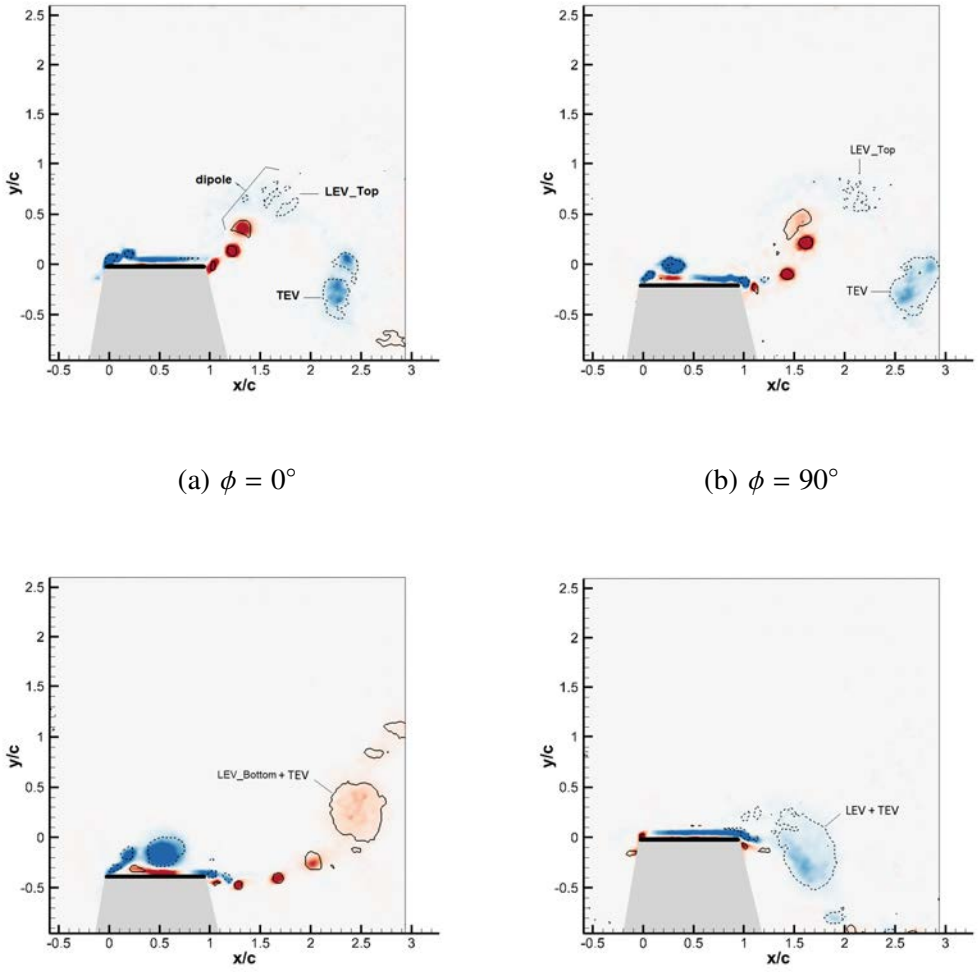

(a) $\phi = 0°$

(b) $\phi = 90°$

(c) $\phi = 90°$

(d) $\phi = 180°$

Figure 3.4: Selected phases at $St = 0.2$ for $h_0/c = 0.2$, $k = 1.57$ (a and b) and $h_0/c = 0.4$, $k = 0.785$ (c and d).

As Fig. 3.4 shows, the phase at which this occurs and the nature of the interaction depends on h_0/c. At $h_0/c = 0.2$, the LEV generated during the downstroke reaches the trailing edge as the nascent (opposite-sign) trailing edge structures begin to shed at the beginning of the subsequent downstroke (i.e. a full cycle later), and consequently there is a strong interaction between opposite-sign leading- and trailing-edge structures as shown in Fig. 3.4(a). This results in a wide wake consisting of dipoles formed from leading- and trailing-edge vorticity. Lua et. al. [46] observed a similar sequence of leading- and trailing-edge vortex shedding at $Re_c = 1000$, which they called a *neutral* wake. However, whereas strong asymmetries exist in the dipoles observed here, Lua et. al. [46] observed only small differences in the vortex strengths, and the distribution of the vortices was such that stronger interactions were formed between like-signed vortices instead of forming dipoles. At $h_0/c = 0.4$, the leading edge vortex passes the trailing edge at a phase angle of approximately 180° along with like-signed trailing edge vorticity shed during the subsequent upstroke.

Fig. 3.5 shows the vorticity field evolving downstream of the plate for $St = 0.2$ and $\phi = 135°$ at the three amplitudes discussed above. The consequences of LEV interaction with the trailing edge structures are apparent by comparing the three vorticity fields. At $h_0/c = 0.2$ ($k = 1.57$), the LEV forms the asymmetric dipole with the much stronger TEV structure as described above, whereas for the higher amplitudes, the LEV is found among the like-signed TEV structures.

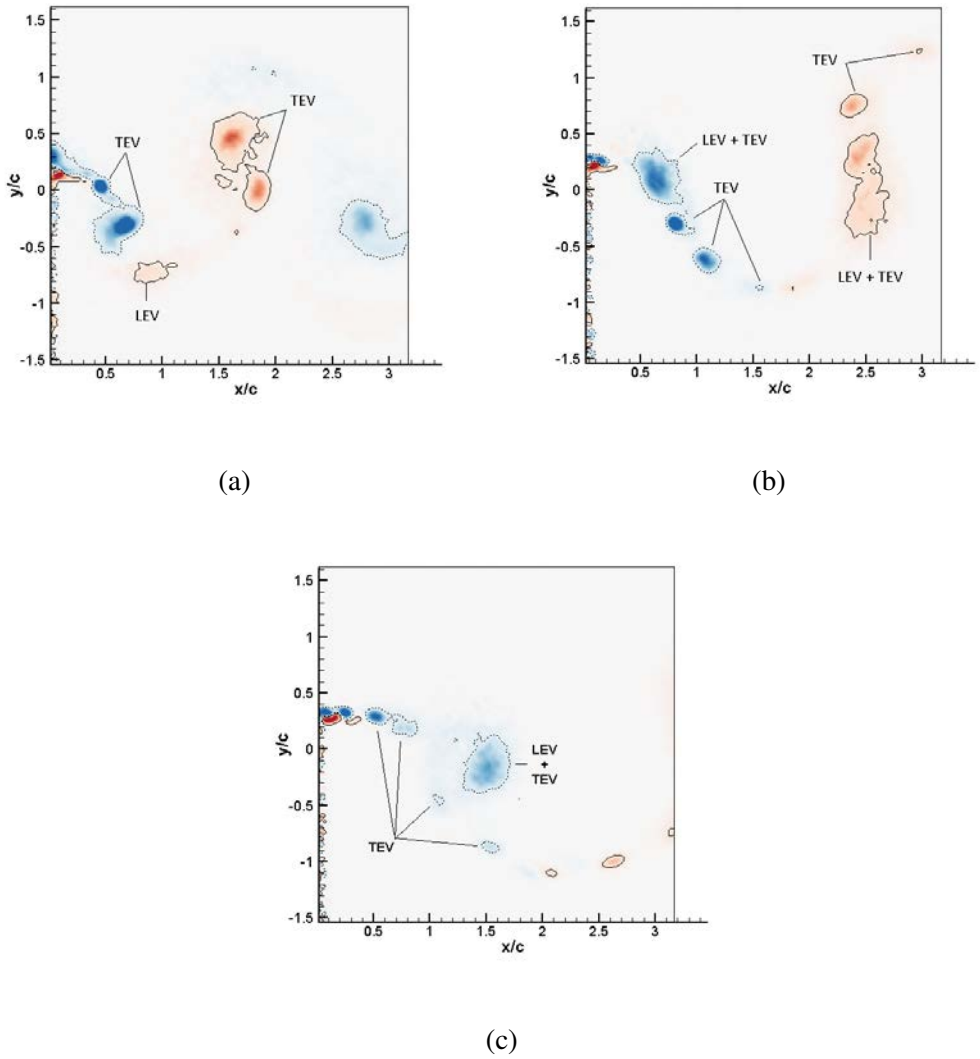

(a) (b)

(c)

Figure 3.5: Wake vorticity distributions downstream of the plate at $\phi = 135°$ for $St = 0.2$. (a) $h_0/c = 0.2$, $k = 1.57$; (b) $h_0/c = 0.3$, $k = 1.05$, (c) $h_0/c = 0.4$, $k = 0.785$.

3.1.2 $St = 0.1$ and 0.3

Fig. 3.6 shows the flow field at $\phi = 90°$ for each of the amplitudes when the Strouhal number is reduced to 0.1. A fine-scale Kármán-like vortex street, shedding from the blunt trailing edge, is observed in the wake. In contrast to $St = 0.2$, where formation of a single leading edge vortex structure is typical, the increased convection rate for the cases with $St = 0.1$ results in the formation of multiple LEV structures. Rival et. al. [52] showed that pinch off occurs at sufficiently low Strouhal numbers ($St = 0.08$, $h_0/c = 0.5$, $k = 0.25$) and the dimensionless formation time $\hat{T}$, as defined by Dabiri [20], falls into a range of $4.4 < \hat{T} < 5.0$; agreeing well with the concept of an optimal vortex formation time.

Fig. 3.7 shows the evolution of vorticity for $St = 0.3$ and $h_0/c = 0.3$. The reduced frequency, $k = \pi/2 = 1.57$ matches that for $St = 0.2$ and $h_0/c = 0.2$, and the flow field exhibits a similar wide wake with asymmetric dipole structure as that observed for $St = 0.2$, $k = 1.57$, again emphasizing the importance of reduced frequency to the flow structure. A comparison of the corresponding phases in Figs. 3.4a and b with 3.7b and c reveals a striking similarity in the vorticity distributions.

Fig. 3.8 shows the vorticity field at $\phi = 90°$ for $St = 0.3$ with $h_0/c = 0.2$ ($k = 2.36$) and 0.4 ($k = 1.18$). Whereas at this phase angle, the LEV is near the leading edge in both cases, at $h_0/c = 0.2$, the LEV moves relatively little over the subsequent cycle due to the reduced oscillation period. This is evident in Fig. 3.8(a) where a diffused and distorted LEV, shed in the previous cycle, can be observed passing the trailing edge. In addition, two concentrated vortex structures are shed from the trailing edge at $k = 2.36$; however, there are several at $k = 1.18$. For all three amplitudes at $St = 0.3$, the LEV was found to detach

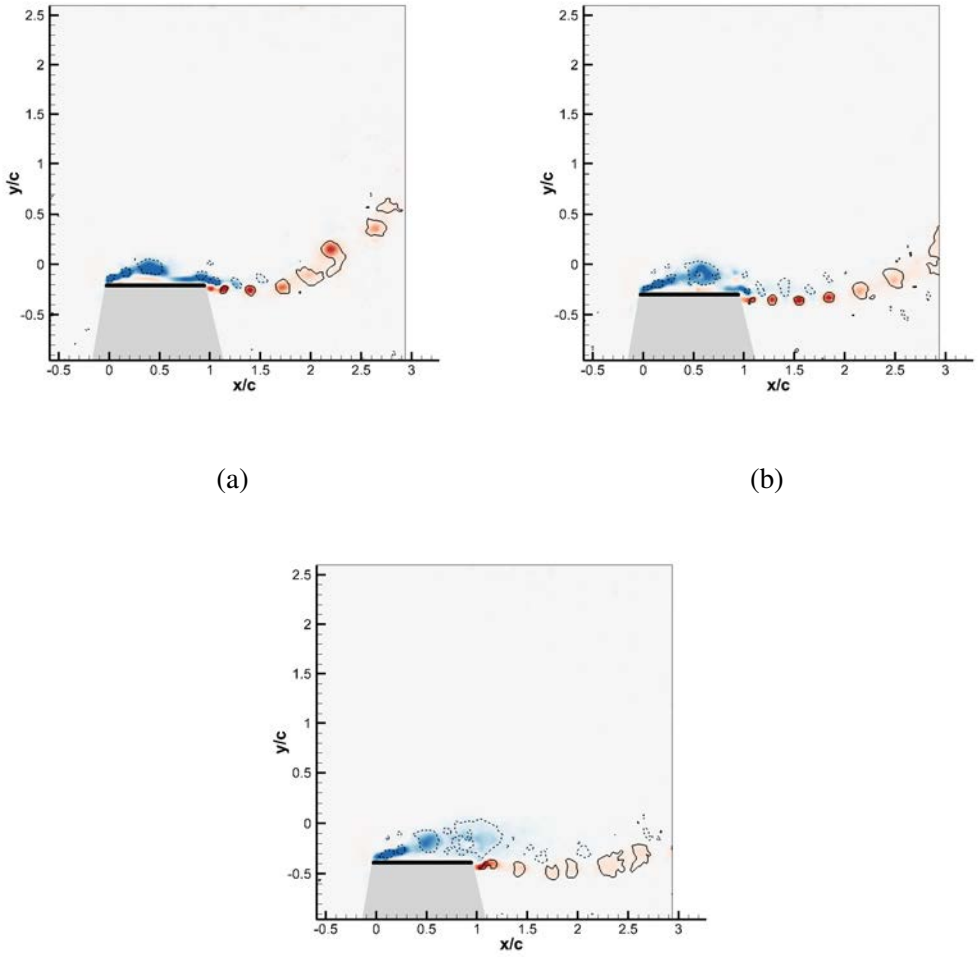

(a) (b)

(c)

Figure 3.6: The vorticity distribution near the plate for $St = 0.1$ and $\phi = 90°$. (a) $h_0/c = 0.2$, $k = 0.785$; (b) $h_0/c = 0.3$, $k = 0.524$; (c) $h_0/c = 0.4$; $k = 0.393$.

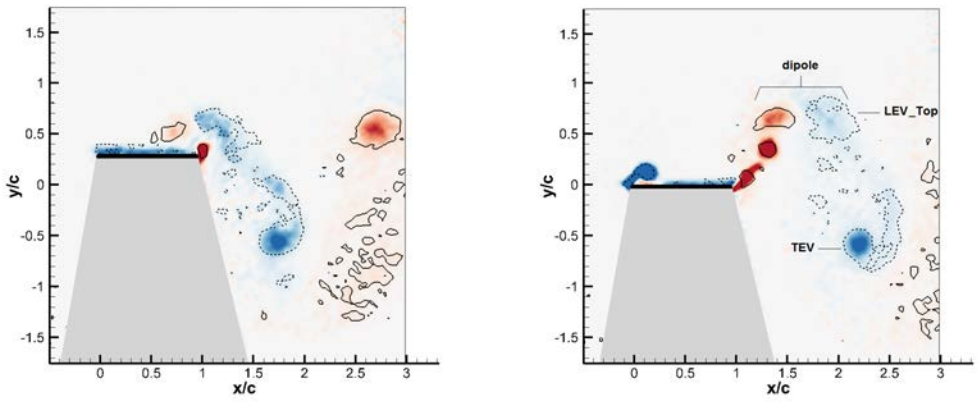

(a) $\phi = -90°$

(b) $\phi = 0°$

(c) $\phi = 90°$

(d) $\phi = 180°$

Figure 3.7: Evolution of spanwise vorticity with phase for $St = 0.3$, $h_0/c = 0.3$, $k = 1.57$.

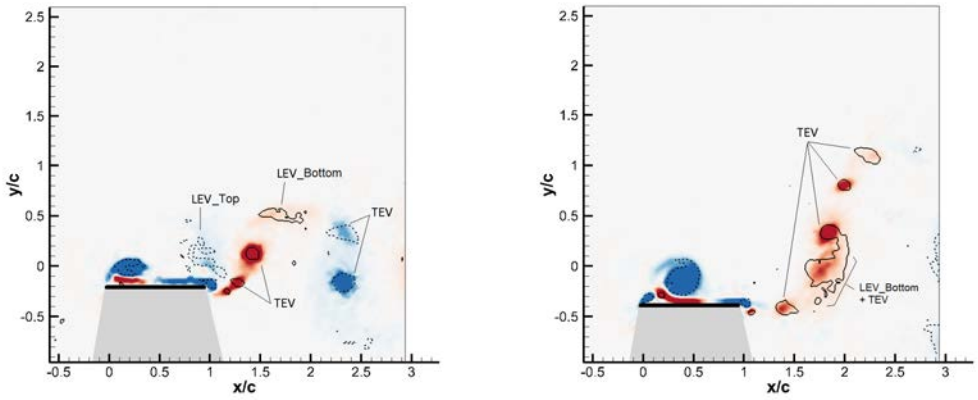

(a) $\phi = 90°$ (b) $\phi = 90°$

Figure 3.8: Vorticity distributions for $St = 0.3$ and a) $h_0/c = 0.2$, $k = 2.36$; b) $h_0/c = 0.4$, $k = 1.18$.

from its forming shear layer at approximately 0 degrees, concomitant with the penetration of the opposite-sign vorticity.

The resulting wake patterns are highly dissimilar with varying amplitude, as shown in Fig. 3.9. Whereas at $h_0/c = 0.2$, the wake rapidly organizes into a reverse Kármán street with vortices only slightly-displaced from the symmetry plane, at $h_0/c = 0.3$, the broad dipole wake persists further downstream, and at $h_0/c = 0.4$, since the LEV is now integrated within the multiple trailing-edge structures, the wake again appears to be gradually evolving into a reverse Kármán -type structure.

3.1.3 $St \geq 0.4$

Increasing the Strouhal number to 0.4, some significant differences are observed on the qualitative structure and evolution of the vorticity field that suggest an increased

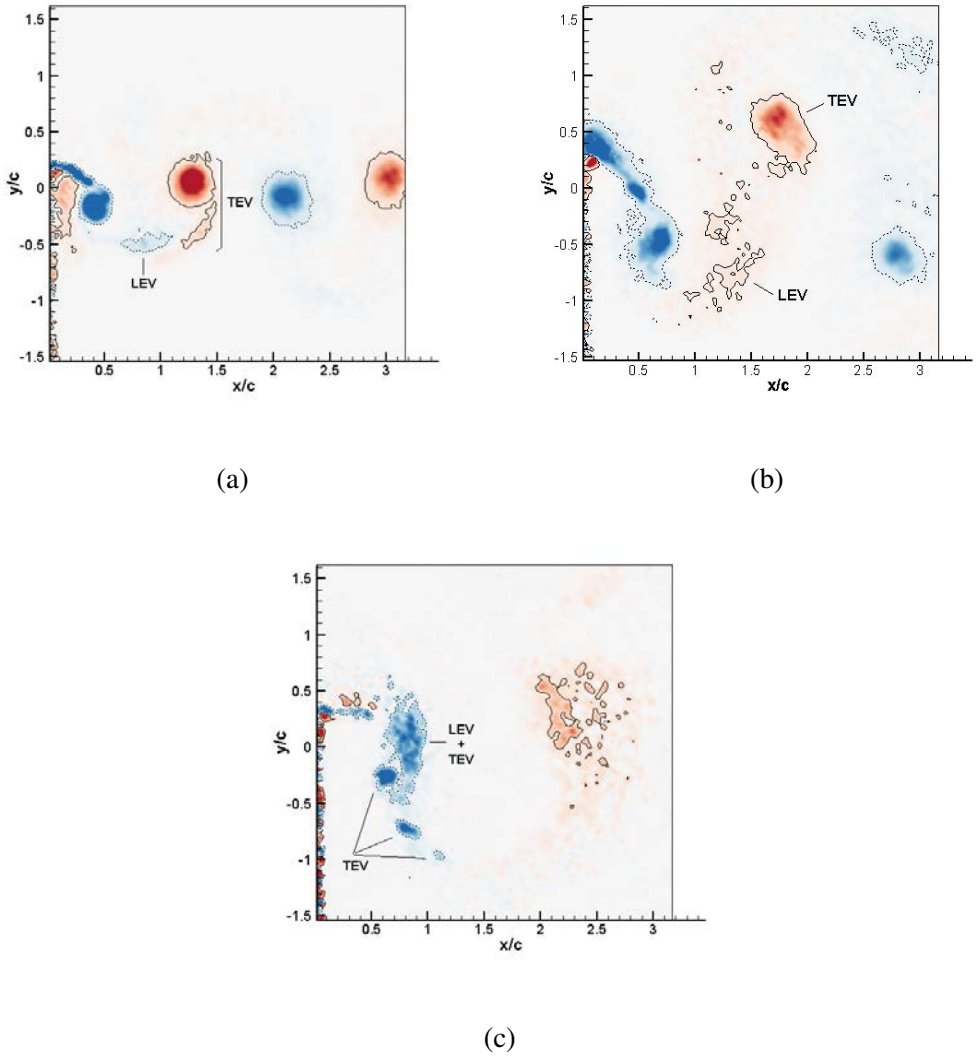

Figure 3.9: Wake vorticity distributions for $St = 0.3$ at $\phi = 135°$, for (a) $h_0/c = 0.2$, $k = 2.36$; (b) $h_0/c = 0.3$, $k = 1.57$; (c) $h_0/c = 0.4$, $k = 1.18$.

influence of Strouhal number, in this range. Fig. 3.10 shows the evolution of the vorticity field for $St = 0.4$, $h_0/c = 0.3$, and $k = 2.09$. One important difference is that the LEV structure is now apparent at $\phi = -45°$, whereas it was not observed until $\phi = 0°$ in all previous cases – which included a higher value of k for $St = 0.3$ and $h_0/c = 0.2$, supporting that this is not a reduced frequency effect. Rather, this may be attributed to the higher effective angle of attack ($\tan^{-1}(fh_0/U)$) corresponding to the increased Strouhal number. The advancement of LEV generation at $St = 0.4$ was also observed for $h_0/c = 0.2$ and 0.4. In addition, trailing edge vorticity now forms a single large vortex rather than multiple discrete structures. The decrease in the number of trailing edge structures was attributed to reduced frequency in the previously-examined cases; however, the reduction appears to be augmented at $St = 0.4$ when compared to Fig. 3.8(a) where $St = 0.3$, $h_0/c = 0.2$ and $k = 2.36$, yet two distinct TEV structures are observed. Another significant difference observed under these conditions is that the LEV is ejected normal to the plate surface upon generation of a new LEV on the subsequent cycle; however, this phenomenon wasn't universally observed at higher Strouhal numbers.

The convection rate (with respect to phase) of the LEV at $St = 0.4$ is markedly lower than that for the lower Strouhal numbers at similar reduced frequencies. This is best illustrated by Fig. 3.11 where $k = 1.57$, matching the reduced frequencies of the lower-Strouhal-number cases shown in Figs 3.4a and b, and 3.7. In Fig. 3.11, the LEV – which becomes quite diffuse and elongated as it persists on the upper surface of the plate during the upstroke – does not fully convect beyond the trailing edge. Rather, the nascent TEV structure which begins to form at $\phi \approx 270°$ divides most of the LEV structure from the

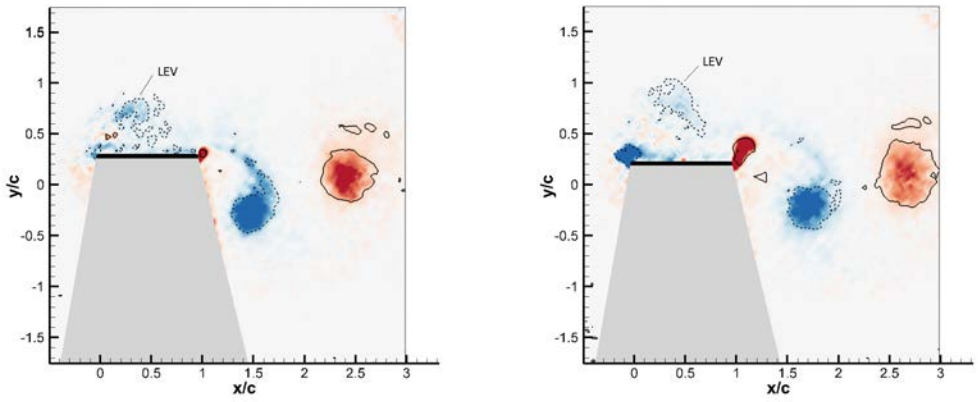

(a) $\phi = -90°$

(b) $\phi = -45°$

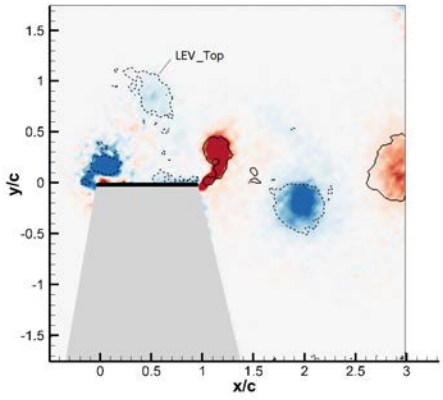

(c) $\phi = 0°$

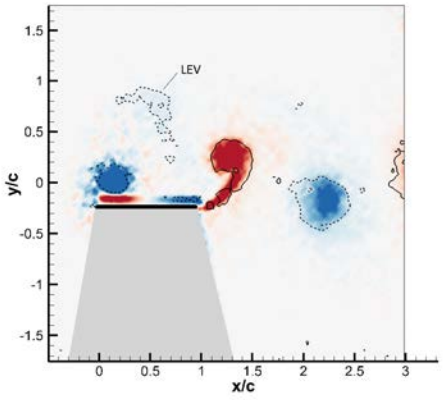

(d) $\phi = 45°$

Figure 3.10: Evolution of spanwise vorticity with phase for $St = 0.4$, $h_0/c = 0.3$, $k = 2.09$.

previously-shed like-signed trailing edge structures. As a result, the dipole formed by the weak LEV and the primary TEV structure is oriented upstream at $\phi = 90^\circ$ rather than in the transverse direction as is the case for $k = 1.57$ when $St = 0.2$ and 0.3.

Wake vorticity distributions for $St = 0.4$ are given in Fig. 3.12. For $h_0/c = 0.2$ and 0.3, the wake rapidly organizes into a reverse Kármán vortex street. However, as with the wakes for $St = 0.2$ and 0.3, shown in Figs. 3.5 and 3.9, respectively, when $h_0/c = 0.4$ such that $k = 1.57$, a pair of dipoles are formed in the wake, again making the wake very broad.

Fig. 3.13 shows vorticity distributions for $St = 0.5$, $h_0/c = 0.2$, and $k = 3.93$, which is largely representative of all three amplitudes. In general, the patterns are similar to $St = 0.4$, with reduced LEV convection and more concentrated leading- and trailing-edge vortex structures. At all plunge amplitudes, the shear layers emerging from the leading and trailing edges accumulate in single leading- and trailing-edge vortices which are approximately stationary during the upstroke and downstroke in which they are formed. This results in a strong interaction between the LEV and the plate during the subsequent stroke in which the LEV is flattened and dissipated. Due to the limited streamwise motion of the LEV, it appears that the LEV vorticity makes little to no contribution to the vorticity in the wake of the plate. In fact, as Fig. 3.13 shows, the LEV partially circumnavigates the leading edge at $\phi = 0^\circ$ and 180°, as also observed by Lewin and Haj-Hariri [43]. Circumnavigation of the LEV was also observed at $h_0/c = 0.3$ but not at $h_0/c = 0.4$. Fig. 3.14 shows vorticity distributions in the wake for all three plunge amplitudes at $St = 0.5$. It is evident that the wake rapidly evolves into a reverse Kármán vortex street for all cases.

At $St = 0.6$, the flow field is qualitatively similar to that at $St = 0.5$ except that a

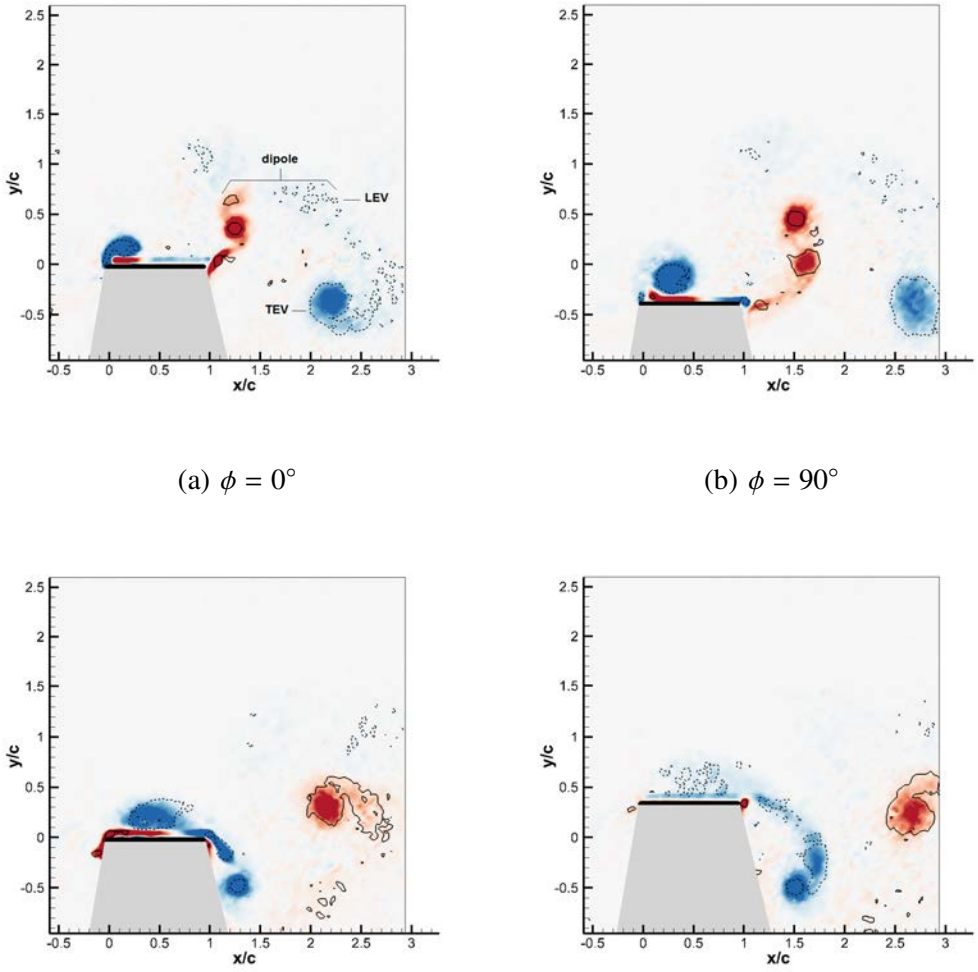

(a) $\phi = 0°$ (b) $\phi = 90°$

(c) $\phi = 180°$ (d) $\phi = 270°$

Figure 3.11: Wake vorticity distributions for $St = 0.4$, $h_0/c = 0.4$, $k = 1.57$.

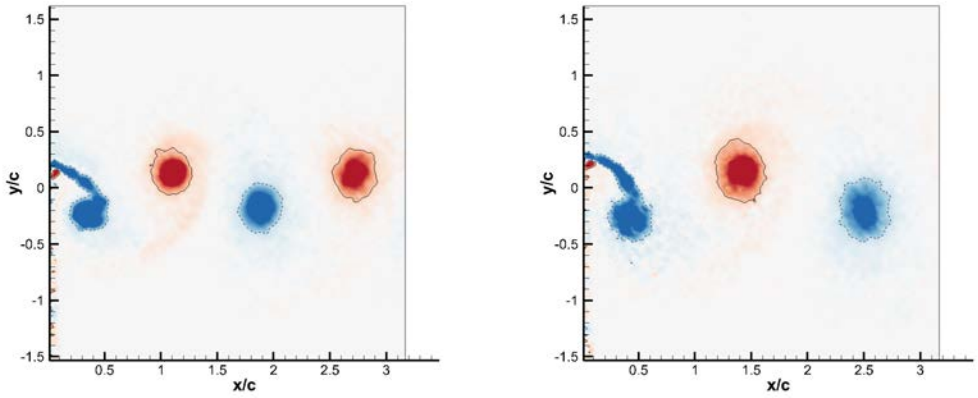

(a) (b)

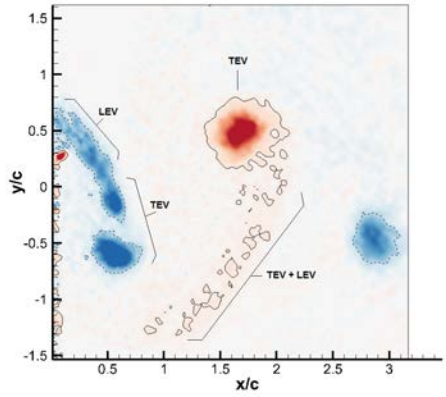

(c)

Figure 3.12: Wake vorticity distributions for $St = 0.4$ at $\phi = 135°$, for (a) $h_0/c = 0.2$, $k = 3.14$; (b) $h_0/c = 0.3$, $k = 2.09$; (c) $h_0/c = 0.4$, $k = 1.57$.

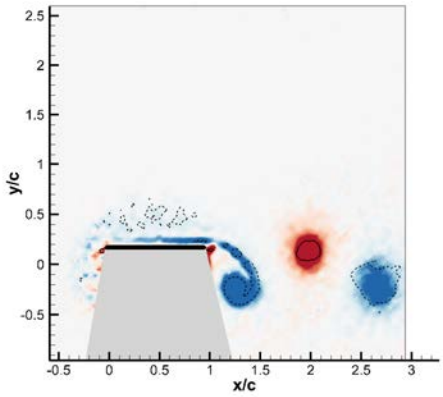

(a) $\phi = -90°$

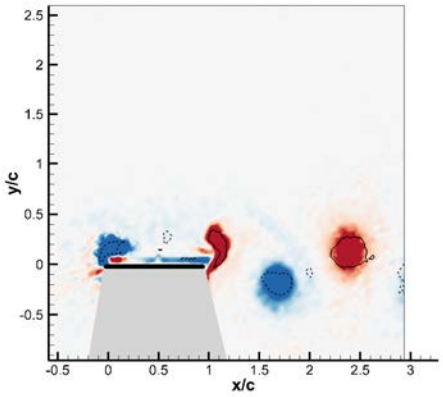

(b) $\phi = 0°$

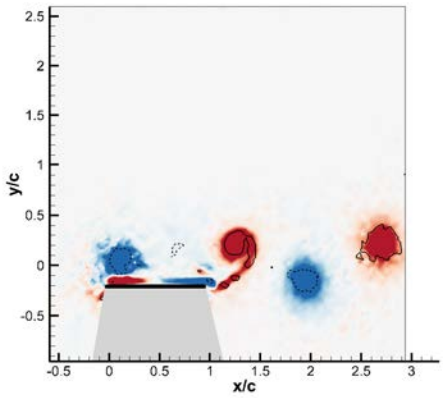

(c) $\phi = 90°$

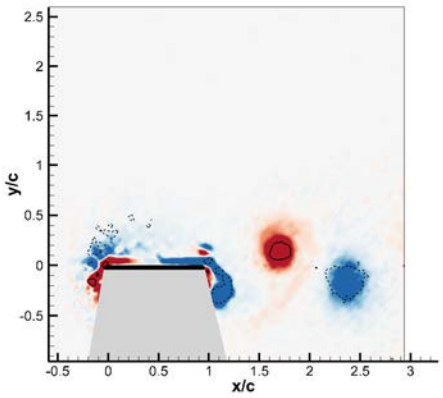

(d) $\phi = 180°$

Figure 3.13: Vorticity distributions at $St = 0.5$, $h_0/c = 0.2$, $k = 3.93$.

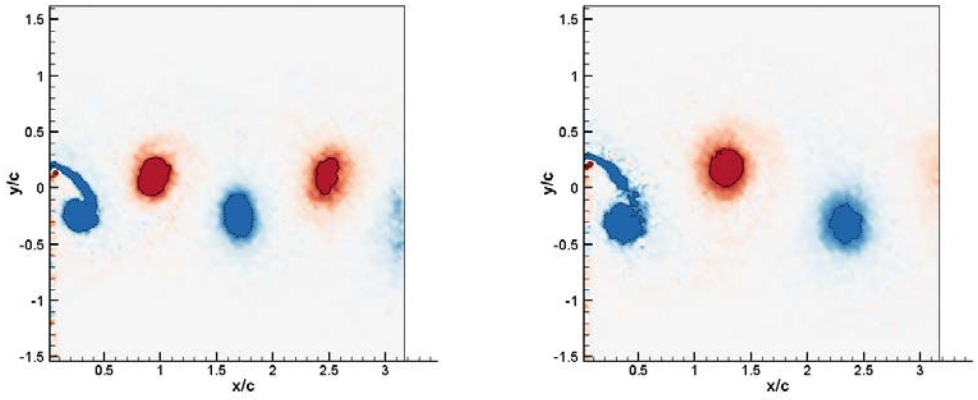

(a)

(b)

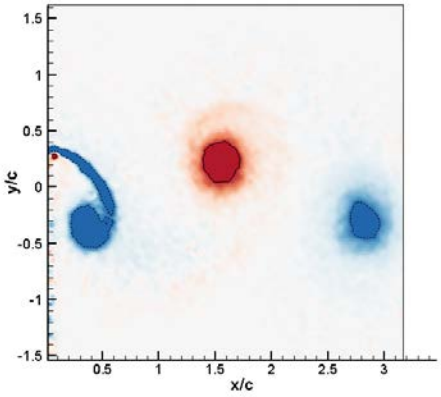

(c)

Figure 3.14: Wake vorticity distributions for $St = 0.5$ at $\phi = 135°$, for (a) $h_0/c = 0.2$, $k = 3.93$; (b) $h_0/c = 0.3$, $k = 2.62$; (c) $h_0/c = 0.4$, $k = 1.96$.

significantly-deflected wake appears at $h_0/c = 0.4$ as first reported by Jones et. al. [37]. Fig. 3.15 shows the vorticity field for $St = 0.6$ with $h_0/c = 0.2$ ($k = 4.71$) and $h_0/c = 0.4$ ($k = 2.36$) in the vicinity of the plate and in the wake.

3.2 Interaction Between the LEV and the Airfoil Surface

Figure 3.16 shows phase-averaged vorticity distributions using time-resolved PIV for the case of $h_o/c = 0.3$, $St = 0.3$, $k = 1.57$. Of particular interest is the mechanism by which the LEV detaches from the shear layer, and the nature of the interaction between the LEV and the secondary vorticity. The vorticity field shows as the plate accelerates, the shear layer injects a significant amount of vorticity to the top of the plate, which rapidly forms into the LEV (3.16(a), 3.16(b), 3.16(c), and 3.16(d)). The LEV grows in size and strength and separates from the boundary layer vortex (3.16(e)). Then the LEV generates opposite-sign vorticity (secondary vorticity) on the surface of the plate due to the pressure gradient setup by the LEV (3.16(f)). The LEV and secondary vorticity continue to grow (3.16(g), 3.16(h), and 3.16(i)) until the feeding shear layer starts to weaken (3.16(i)). When the source of vorticity for the LEV is gone, the LEV detaches from the shear layer (3.16(j)) and starts to advect along the chord length (3.16(k) and 3.16(l)). At this time, the opposite-sign vorticity starts to lift up from opposite-sign vortex layer and spill out into the external flow (3.16(k) and 3.16(l)).

The existence ofsecondary vorticity is evidently a common phenomenon occurring in a wide variety of applications when a vortex interacts with a wall ([21]). In general, a boundary-layer eruption occurs in such circumstances in the form of a thin spire containing

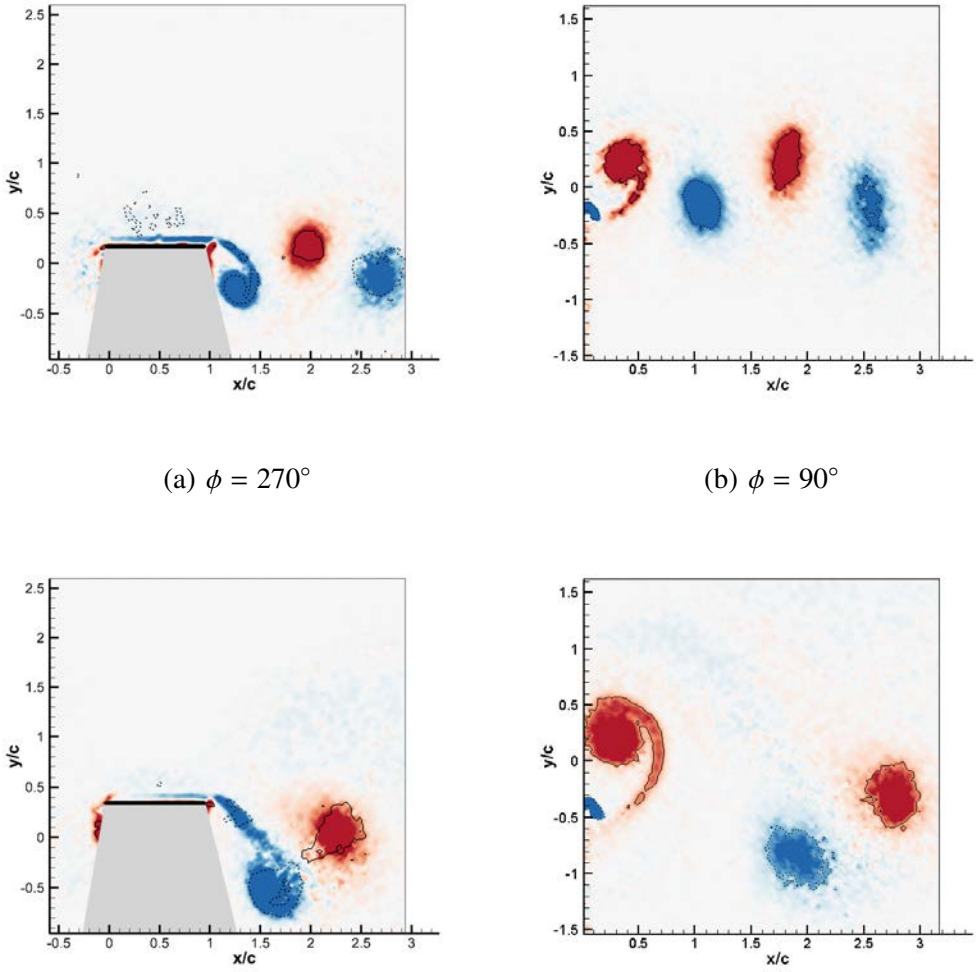

(a) $\phi = 270°$ (b) $\phi = 90°$

(c) $\phi = 270°$ (d) $\phi = 90°$

Figure 3.15: Vorticity distribution at $St = 0.6$, for (a) $h_0/c = 0.2$ near the panel and (b) in the wake, and (c) $h_0/c = 0.4$ near the panel and (d) in the wake.

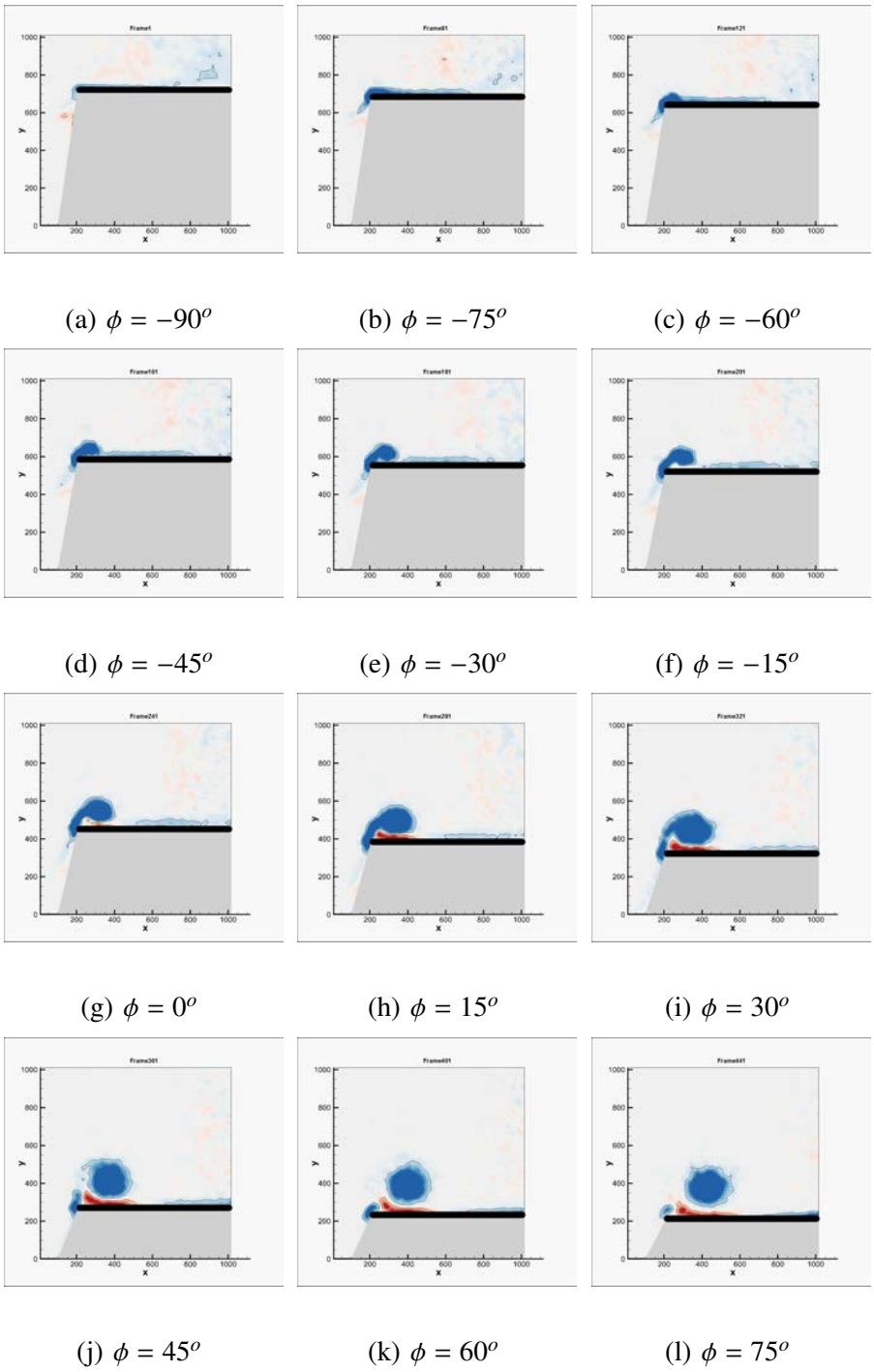

(a) $\phi = -90^o$ (b) $\phi = -75^o$ (c) $\phi = -60^o$

(d) $\phi = -45^o$ (e) $\phi = -30^o$ (f) $\phi = -15^o$

(g) $\phi = 0^o$ (h) $\phi = 15^o$ (i) $\phi = 30^o$

(j) $\phi = 45^o$ (k) $\phi = 60^o$ (l) $\phi = 75^o$

Figure 3.16: A time sequence of the averaged vorticity contours for $h_o/c = 0.3$, $St = 0.3$, $k = 1.57$.

significant levels of vorticity, which usually rolls up into a secondary vortex (Visbal [65]). As discussed in many previous studies, it has been believed that this opposite-sign vorticity is responsible for LEV detachment from its feeding shear layer which prevents it from achieving further circulation. A dominant concept is the eruption of the wall boundary layer leading to secondary vortex, originally calculated by Walker (1978) for a vortex along a wall. Acharya and Metwally (1992) stated that, "[the secondary vorticity] cuts off the dynamic-stall vortex from its source of vorticity ". As observed by Lewin and Haj-Hariri [43], for an airfoil of elliptical cross section plunging at $Re_c = 500$ the counter-clockwise vorticity appears to participate in the separation of the LEV from the shear layer as it is drawn forward and ultimately penetrates the shear layer. However, the interaction appears to be more complicated at higher Reynolds numbers. Visbal [64] numerically showed that in addition to the primary leading edge vortical structures, another distinct feature is the ejection of secondary vorticity due to the ensuing vortexsurface interaction. This ejected vorticity is quite prominent between the two primary dynamic-stall vortices, and eventually completely surrounds the leading vortex. Further downstream, this secondary vorticity becomes less apparent due to spanwise instability effects, as discussed later. Recently, Rival et al. [53], argued that there are two mechanisms that are responsible for the LEV detachment process: a) the eruption layer (opposite-sign vorticity) as discussed, and b) flow reversal from the trailing edge. The former affected by the vortex growth rate and thus also the feeding shear layer. The latter dictates the overall maximum circulation of the LEV and forces a rapid cut-off once the rear stagnation point passes off of the trailing edge, changing the topology of the flow field. In our study, the chord length compared to the

convective length scale (UT or U/f) is sufficiently large, therefore the flow reversal from the trailing edge was not observed. It is not clear if the eruption of opposite-sign vorticity is responsible for the LEV detachment or if it is simply concurrent with the weakening of the shear layer at the end of the stroke. It was shown by Wojcik and Buchholz [77, 78] that, for a rotating blade in which a stable leading-edge vortex is formed, entrainment of the opposite-sign vorticity is a significant mechanism for the regulation of vortex strength.

Evolution of the instantaneous time-resolved flow field (real flow behavior) was examined to determine the mechanisms of vorticity transport governing the development and strength of the leading edge vortex. The instantaneous vorticity field for the case of $h_o/c = 0.3$, $St = 0.3$, $k = 1.57$ is shown in Figure 3.17. Time-resolved PIV measurements in the two-dimensional chordwise plane revealed an important difference between the instantaneous and phase-averaged realizations of the leading-edge vortex development. As shown in Figure 3.17, the evolution of the phase-averaged vorticity field is such that the secondary vorticity (red) grows throughout the downstroke, remains as a simply-connected structure, and is drawn upstream by the induction of the leading-edge vortex, ultimately penetrating the shear layer at around $\phi = 55$ degrees as the shear layer weakens. A similar evolution was observed by Lewin and Haj-Hariri [43] in the instantaneous vorticity field of a plunging elliptical airfoil at $Re = 500$. However, in the present case, the interaction between the leading-edge vortex and secondary vorticity is much more complex. Individual frames reveal small packets of secondary vorticity (shown by green arrows) being entrained by the leading-edge shear layer, and drawn into the leading-edge vortex throughout the downstroke, but with the greatest rate of entrainment observed later in the stroke,

where the penetration is observed in the mean vorticity field. The observation of this entrainment suggests that resulting annihilation within the leading-edge vortex may provide an important mechanism regulating leading-edge vortex strength. Visbal [64] also noted similar entrainment on a plunging airfoil when the Reynolds number was large enough for the flow to be transitional. Wojcik and Buchholz [77, 78] observed similar entrainment on a rotating flat plate at high angle of attack, and performed a vorticity flux analysis within the leading-edge vortex revealing that the entrainment is an important sink of vorticity to balance the leading-edge shear layer flux, and thus maintain a bounded leading-edge-vortex circulation in that case. Although, the instantaneous flow fields represent the real physics, in the next chapter, we perform a vorticity transport analysis of phase-averaged flow field for the 2-D plunging airfoil to better understand the role of this secondary vorticity on the LEV circulation.

3.3 Advection of Leading Edge Vortex Structures

Section 3.1 demonstrated that the qualitative behavior of wake structures depends primarily on reduced frequency with a secondary influence of Strouhal number. In this section, we examine that assertion in more detail by investigating the LEV streamwise position as a function of time, phase, Strouhal number, and reduced frequency. The contribution of the LEV to the wake circulation and structure depends on the convection rate of the LEV since that affects the deterioration of the LEV through its interaction with the plate, and how the LEV interacts with vorticity shed from the trailing edge.

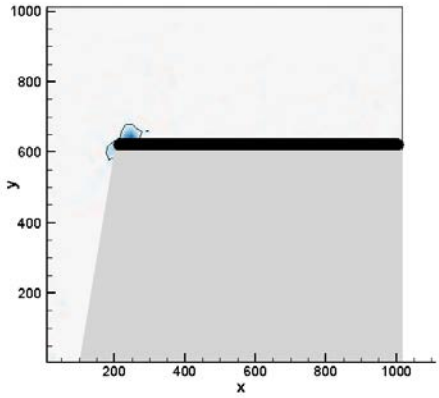

(a) $\phi = -45^o$

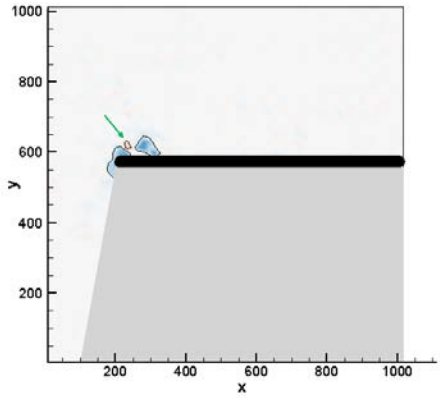

(b) $\phi = -30^o$

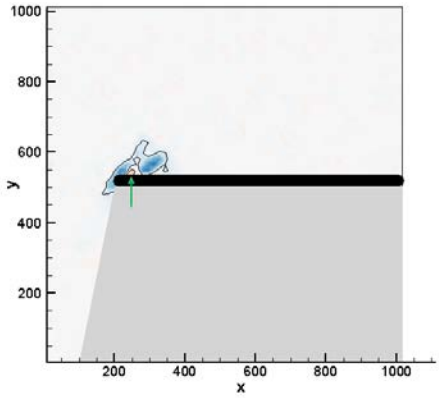

(c) $\phi = -15^o$

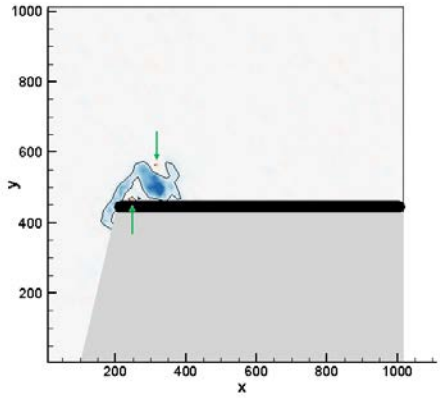

(d) $\phi = 0^o$

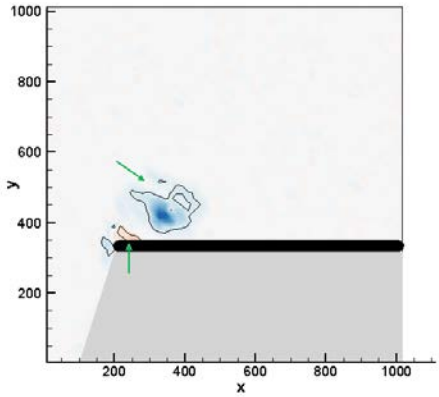

(e) $\phi = 30^o$

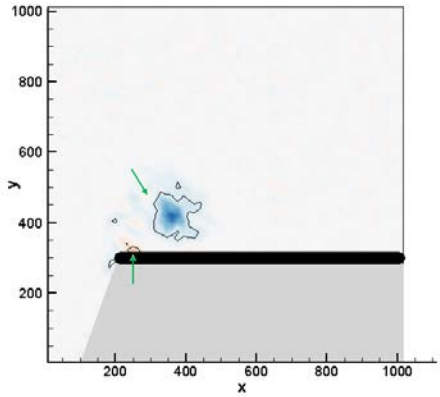

(f) $\phi = 45^o$

Figure 3.17: A time sequence of the instantaneous vorticity contours for $h_o/c = 0.3$, $St = 0.3$, $k = 1.57$.

3.3.1 Leading Edge Vortex Trajectories

Fig. 3.18(a) shows the streamwise positions of leading edge vortex cores as a function of phase angle for the three plunge amplitudes and $0.2 \leq St \leq 0.5$. Strouhal number and amplitude values are indicated by symbol shape and line type, respectively, whereas symbol color has been used to define reduced frequency ranges (green: $k \leq 1.17$, red: $k = 1.57$, light blue: $1.96 \leq k \leq 2.36$, dark blue: $k \geq 2.62$). The results for St=0.1 and 0.6 have not been included here, since for $St = 0.1$, there are multiple weak LEV structures which rapidly leave the field of view, and for $St = 0.6$ the LEV is essentially stationary, similar to $St = 0.5$. The location of maximum vorticity value within the LEV has been identified manually and used to track the vortex cores so that the qualitative observations about LEV behavior can be further clarified and quantified.

Fig. 3.18(a) clearly shows the importance of reduced frequency to the trajectories of the LEV structures. With only a couple of exceptions (one in the top three trajectories and one in the bottom three), the trajectories are ordered monotonically from the lowest reduced frequency ($k = 0.785$) at the top to the highest ($k = 3.14$) at the bottom. Whereas, during the downstroke, the LEV did not pass the mid-chord point for any of the parameter combinations shown, the LEV celerity in the low-reduced-frequency cases (light blue) increased significantly during the upstroke. A notable increase was also observed for the cases in which $k = 1.57$ (red) although those LEVs did not pass the trailing edge by the end of the upstroke. Although the impact of Strouhal number is not easily observed in the LEV trajectories, its effect can be seen by comparing the positions of the LEV's for the $k = 1.57$ cases during the upstroke. Whereas the LEV's for $St = 0.2$ and 0.3 generally follow a

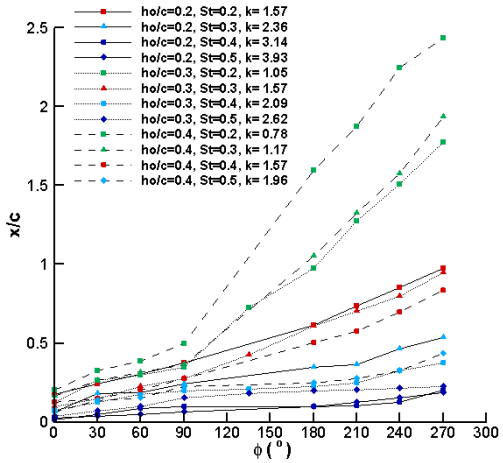

(a)

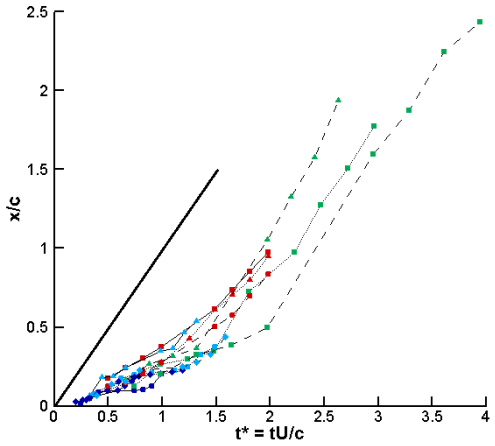

(b)

Figure 3.18: LEV trajectories as a function of a) phase angle and b) dimensionless time. The line in (b) indicates the free-stream velocity.

similar trajectory, the LEV at $St = 0.4$ lags the other two cases by $x/c \approx 0.1$ throughout the upstroke.

The trajectory data are plotted in Fig. 3.18(b) as a function of dimensionless time $t^* = tU/c$. The convective time scale c/U is the same in all cases so t^* is proportional to dimensional time where $t^* = 0$ corresponds to $\phi = -90°$. The LEV convective velocities are similar during the downstroke, and move at approximately $0.35U$. Consideration of Figs 3.18(a) and 3.18(b) shows that during the upstroke, for $k \leq 1.17$, the LEV convection speed is very similar to the free stream velocity.

Figure 3.19 shows the streamwise position of the LEV at $\phi = 270°$ as a function of both Strouhal number and reduced frequency, illustrating that reduced frequency is a superior similarity variable for the LEV position, and Fig. 3.19(b) reveals an approximately binary outcome. For high reduced frequencies and Strouhal numbers, both plots show that the LEV position is relatively insensitive to the forcing frequency. For $k \gtrapprox 2$, the LEVs are "trapped" on the plate surface, leading to their ultimate obliteration through interaction with the plate surface; whereas for $k \lessapprox 2$, the LEVs are eventually shed into the wake and the position is highly sensitive to reduced frequency.

3.3.2 The Physics Governing Vortex Trajectories

Fig. 3.18(a) shows that, for $0° \leq \phi \leq 90°$ – in which the LEV is being formed during the downstroke – the convection velocity of the LEV varies little throughout the parameter range investigated here; however, during the upstroke ($90° < \phi < 180°$), during which time the LEV is either ejected into the wake or destroyed through its interaction

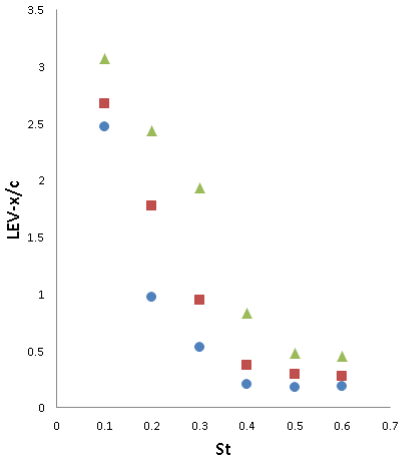

(a)

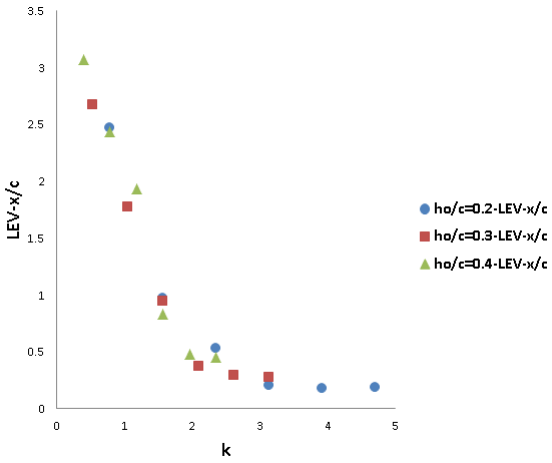

(b)

Figure 3.19: LEV location at $\phi = 270°$ vs. (a) Strouhal number, (b) Reduced frequency.

with the plate, the convection velocity is much more sensitive to reduced frequency. The convection velocity is governed, at least in part, by the competition between the free-stream velocity and the induced velocity field imparted on the vortex through its interaction with the surface of the plate. Modeling this interaction as a compact vortex interacting with an infinite wall, the convection velocity is given as Doligalski et. al. [21]:

$$V_c = U - \frac{\Gamma}{4\pi a} \tag{3.2}$$

where U is the free-stream velocity, Γ is the vortex circulation, and a is its distance from the wall. Fig. 3.20(a) shows the circulation of the LEV as a function of Strouhal number at $\phi = 90°$ – the phase at which the LEV is typically near its maximum circulation – revealing a significantly increased sensitivity for each plunge amplitude in the range $0.3 < St < 0.5$. The relationship between circulation and Strouhal number qualitatively resembles the arctangent function governing effective angle of attack, as discussed in Section 3.1.3, suggesting that effective angle of attack is an important parameter governing LEV strength. Referencing Fig. 3.18(a), it is apparent that at all but the lowest Strouhal numbers, the LEV is located well within the streamwise extent of the airfoil at $\phi = 180°$. Evaluating the circulation and wall-normal distance, a (using the point of maximum vorticity) at $\phi = 180°$, the convection velocities were evaluated according to Equation 3.2. The results are given in Fig. 3.20(b) as a function of Strouhal number. A rapid drop in predicted convection velocity is evident between $St = 0.3$ and 0.4, concomitant with the rise in circulation.

This result suggests that Strouhal number should be more important in governing

For the cases in which the LEV had convected near or beyond the trailing edge at $\phi = 180°$, data from an earlier phase was used to perform the calculation. These cases include: $St = 0.2$, $h_0/c = 0.3$ ($\phi = 135°$); $St = 0.2$, $h_0/c = 0.4$ ($\phi = 90°$); and $St = 0.3$, $h_0/c = 0.4$ ($\phi = 90°$).

the celerity of the leading-edge vortex as its value increases beyond approximately 0.4. While we have noted qualitative differences in vortex structure that can be attributed to Strouhal number, the interactions between leading- and trailing-edge vortices, and the resulting wake structures, have been primarily dependent on reduced frequency – even at higher values of Strouhal number. This apparent contradiction can be resolved by considering Figure 3.20(c), which contains the celerity data from Figure 3.20(b) plotted against reduced frequency. Despite the Strouhal-number-related features in the circulation curves for each plunge amplitude, the data do collapse reasonably well onto a line reflecting an inverse relationship between LEV celerity and reduced frequency.

Actual LEV convection velocities were estimated from the measured position data, using forward differences, at phases matching the ones given in Fig. 3.20(c). The results are given in Fig. 3.20(d). While significant differences exist between the magnitudes of the predicted and measured LEV convection velocities, the trends are quite similar. It is very interesting that the measured celerity values drop very rapidly in the range $1.5 < k < 2$, reflecting the bimodal behavior of the LEV position illustrated in Figure 3.19(b).

3.4 Classification of Vortex Shedding Patterns

In Section 3.1, it was shown that the interactions of vortices generated by the plunging plate, and the resulting wake patterns were governed primarily by reduced frequency. However, for $St \gtrapprox 0.4$, some significant Strouhal-number-governed modifications were observed in the formation and structure of the vortices. In the following discussion, we further quantify the effect of Strouhal number on the leading edge vortex, and ultimately

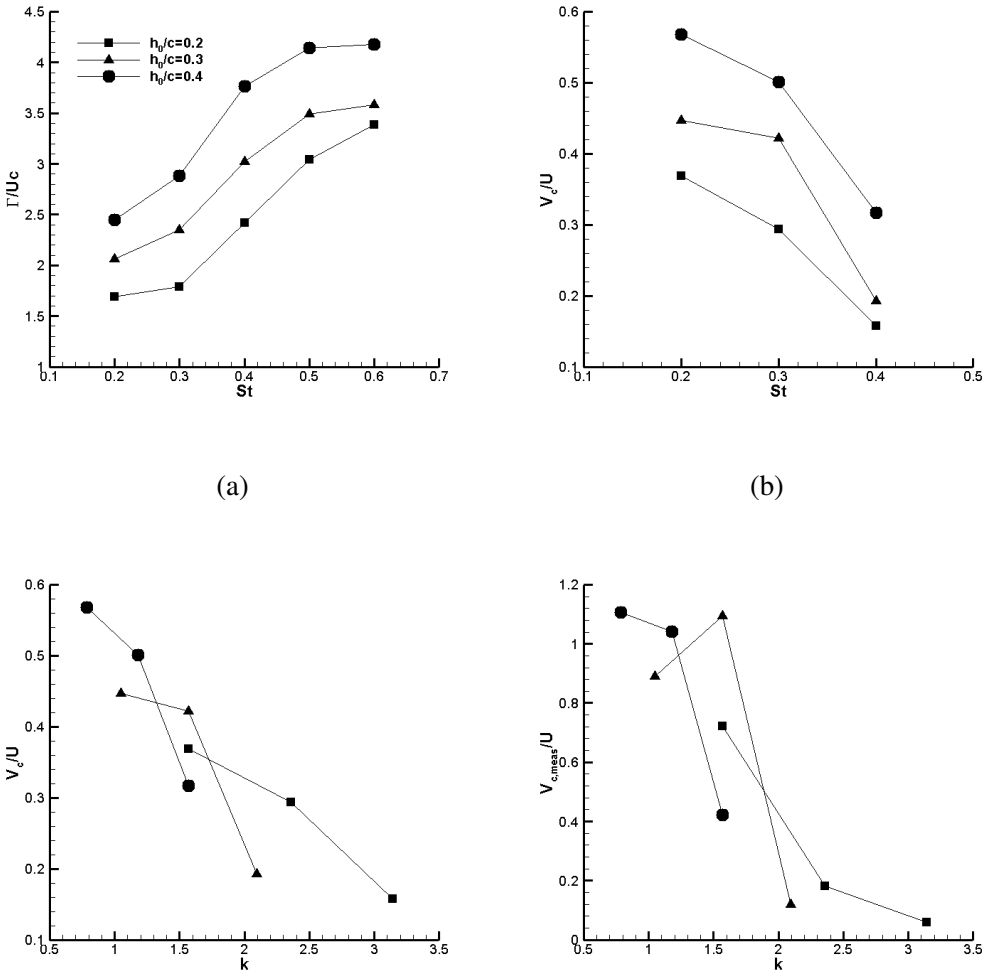

Figure 3.20: a) LEV circulation at $\phi = 90°$ as a function of Strouhal number, b) LEV convection velocities computed using Equation 3.2, (c) the same data plotted as a function of reduced frequency, d) LEV convection velocities estimated from measured vortex trajectories.

reconcile these results with the observations of the reduced-frequency dependence of the wake patterns. A wake structure classification scheme is subsequently introduced which is then compared with observations of the flow evolution in other studies.

3.4.1 Definition of Wake categories

Consolidating the observations reported in Section 3.1, we find that the wake patterns can be classified according to the following categories, primarily determined by k:

Category 1: Vortex shedding is synchronized such that the leading-edge vortex merges with the like-signed trailing-edge structures created in the subsequent stroke. This type of interaction was found for $0.52 \leq k \leq 1.18$. Figs. 3.5(b) and 3.5(c) contain examples showing how the placement of the LEV within the discrete TEV structures can vary with k at $St = 0.2$.

Category 2: With increasing reduced frequency, the LEV convects a shorter distance during a cycle such that it reaches the trailing edge at a later phase, having been weakened through diffusion and interaction with the plate. In Category 2 wakes, the resulting weak LEVs pass the trailing edge *after* the like-sign trailing edge vortex system is shed in the subsequent stroke, and interact with the following stronger, opposite-signed TEV structures to form a dipole that results in a wide wake. This type of wake was observed for $k = 1.57$. This is similar to previously observed wakes referred to as *neutral* wakes Lewin and Haj-Hariri [43] or 2-P wakes Williamson and Roshko [75]. Since the dipoles are highly asymmetric in the present case, the vorticity distribution in the wake suggests positive mean thrust. Examples of this type of wake

structure are shown in Figs. 3.5(a), 3.7, 3.9(b), 3.11, and 3.12(c).

Category 3: For $St = 0.3$ and $h_0/c = 0.2$ ($k = 2.36$), the LEV is further delayed (with respect to the phase of oscillation) so that it passes the trailing edge after the opposite-sign TEV system one full cycle after its own generation, as shown in Figs. 3.8(a) and 3.9(a). Rather than forming an asymmetric dipole wake, the LEV rapidly dissipates, leaving a dominant reverse Kármán vortex wake formed primarily by the TEV. At $St = 0.6$ and $h_0/c = 0.4$, the reduced frequency is the same; however, this type of wake evolution is not observed since the LEV does not pass the trailing edge.

Category 4: A reverse Kármán vortex street is formed consisting either of only vorticity shed from the trailing edge (since the LEV is essentially obliterated through its interaction with the plate), or a weak LEV is released into the wake more than one full cycle after its generation. This occurs for all conditions observed with $k \geq 1.96$ (which, in the present data set is only obtained for $St \geq 0.4$). At $St = 0.6$ with $h_0/c = 0.4$, the TEV structures are deflected transversely such that an asymmetric wake is formed (Figs. 3.15(c) and 3.15(d)).

These categories and the parameters for which they occur are summarized, for the present data set, using the solid black symbols in Fig. 3.21. Lines of constant reduced frequency are drawn in addition to the Strouhal number represented on the abscissa, so that the dependence on each parameter can be evaluated. It is evident that all of the category 1 wakes occur to the left of the k=1.5 line, where the maximum Strouhal number investigated here is 0.3. As noted above, the three cases at $k = 1.57$ all exhibit category 2 wakes. Only

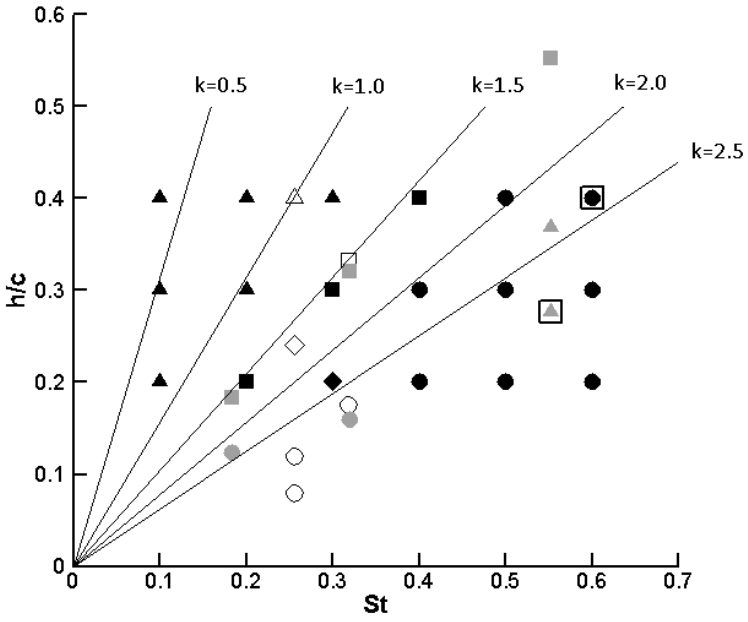

Figure 3.21: Wake pattern classification as function of Strouhal number, plunge amplitude, and reduced frequency. Symbol shapes indicate category number: category 1 (▲), category 2 (■), category 3 (◆), category 4 (●), and a large open square associated with any of these symbols indicates a deflected wake. Black symbols represent the present results, gray symbols represent the results of Lua et. al. [46], and open symbols represent the results of Lewin and Haj-Hariri [43].

one instance of a category 3 wake is observed in our data, which occurs for $St = 0.3$ and $h_0/c = 0.2$.

As h_0/c is reduced from 0.3 to 0.2 at $St = 0.2$, the category increases from 1 to 2 and categories 1, 2, and 3 are present at $St = 0.3$, corresponding to $h_0/c = 0.4$, 0.3, and 0.2, respectively. However, at $St = 0.4$, there is a jump from category 2 to 4 at $St = 0.4$, with a reduction in amplitude from $h_0/c = 0.4$ to 0.3. This appears to cause a breakdown in the pattern established at lower Strouhal numbers, in which we might expect to see category 3 wakes within a range of approximately $1.57 < k < 2.5$. However, category 4 wakes are universally observed at the higher Strouhal numbers. Given that there is only one occurrence of a category 3 wake within our data set suggests that it is not stable for a very large region within the parameter space.

3.4.2 Generalization of Wake Categories

Previous studies of the wake structures formed by NACA 0012 and elliptical airfoils with pure plunge kinematics have been conducted by Lai and Platzer [40], Lewin and Haj-Hariri [43], and Lua et. al. [46]. These studies focus primarily on Reynolds numbers between 500 and 1000, which is significantly lower than the present case. Previous studies Buchholz and Smits [14, 65] noted fundamental differences in flow structure and aerodynamic performance when Reynolds number was varied from $O(10^3)$ to $O(10^4)$, so it is of interest to examine the applicability of the wake categories presented here over a similar range of Reynolds numbers. Since Lewin and Haj-Hariri [43] and Lua et. al. [46] also reported that wake structure was dependent on the nature of the interaction between

leading- and trailing-edge vortices, the classification system presented in Section 3.4.1 has been applied to the flow fields presented in those studies – to the extent that the wake classifications could be determined from the figures – and the results are shown with the current data in Fig. 3.21.

Agreement between the present work and the two prior studies is very good for $k \lessapprox 1.57$ among the points shown in Fig. 3.21. For $k < 1.5$, the one data point shown from Lewin and Haj-Hariri [43] ($St = 0.256$, and $h_0/c = 0.4$) is a category 1 wake, consistent with the present results. Both of the prior studies examined points with $k \approx 1.57$, and all but one were found to produce category 2 wakes, also consistent with the wake evolution observed in the present study. One of the points from Lua et. al. [46] ($St = h_0/c = 0.552$) is of higher amplitude than that investigated in this study and a category 2 wake is still observed. The one point near this line that is category 3 (Lewin and Haj-Hariri [43] $St = 0.256$, $h_0/c = 0.24$) is also close to the only category 3 point observed in the present study.

For $k > 1.57$, most of the data obtained from the prior studies are for $h_0/c < 0.2$. For $k > 1.57$ and $h_0/c < 0.2$, category 4 wakes are universally observed, supporting that, at at the lower Reynolds numbers, the proposed wake classification and the importance of reduced frequency persists at $h_0/c < 0.2$. Only two previous data points are presented for $k > 1.57$ and $h_0/c > 0.2$ (from Lua et. al. [46]), and both of these points indicate category 1 wakes – clearly distinct from the category 4 wakes for that parameter range in the present study.

Two additional wakes from Lua et. al. [46] were characterized but not shown in Fig.

3.21 because they correspond to values of h_0/c much larger than the others. The first point, at $(St, h_0/c, k) = (0.32, 1.6, 0.314)$, convects very quickly, forming a vortex dipole with the trailing edge vortex shed in the same stroke. This observation supports the existence of at least one additional wake category for reduced frequencies below the values investigated in the present study. The second point, which is at $(St, h_0/c, k) = (0.552, 1.104, 0.785)$ exhibits a category 1 wake. This is consistent with the results of the present study for similar reduced frequencies; however, it is noteworthy that (as noted above), for the same Strouhal number, the evolution of most of the other wakes reported by Lua et. al. [46] at $h_0/c < 0.4$ fall into category 1. Taking into account the insight provided by Fig. 3.20, this suggests that the differences in behavior noted here between the observations of Lua et. al. [46] and the present work are caused by different trends in LEV circulation. Given that the wakes recorded by Lua et. al. [46] at $St = 0.552$ with amplitudes of $h_0/c = 0.276$ and 0.368 are within the range of forcing parameters investigated in the present study, the differences must be attributed to either Reynolds number or airfoil shape. In a recent study on leading edge vortex formation and detachment, Rival et. al. [53] demonstrated that leading edge shape can have a significant impact on vortex circulation, with a general trend toward leading edges with high curvature generating larger circulation than those with lower curvature (i.e. NACA 0012). This result suggests a lower circulation for the elliptical airfoil, and thus a faster convection rate, supporting the category 1 result for those wakes. On the other hand, Visbal [65] observed significant differences in flow evolution between $Re_c = 10^3$ and 10^4 at $k = 0.25$, including a lack of transitional effects at the lower Reynolds number, and generation of multiple leading edge vortex structures at the higher

Reynolds number. While it is difficult to extrapolate these results to the significantly higher reduced frequencies noted here ($k > 2$), it is anticipated that Reynolds number could have a significant impact on vortex generation and evolution.

CHAPTER 4
3-D ANALYSIS OF FLOW EVOLUTION AND VORTICITY TRANSPORT ON THE 2-D PLUNGING AIRFOIL

4.1 Flow Volumetric Reconstruction

4.1.1 3-D Evolution of Flow Field

The evolution of the flow field for $k = 1.05$, $St = 0.2$, $h_0/c = 0.3$ is shown in Figures 4.1 through 4.4 within the spanwise extent $\Delta z/c = 1.0$ near the mid-span of the airfoil. Each reconstruction is phase-averaged from 100 velocity fields. The plotted quantity is an isosurface of vorticity magnitude $|\vec{\omega}| = 10\ \mathrm{s}^{-1}$ colored by the sign of ω_z (red is positive and blue is negative). The focus was on the leading edge vortex structure. This particular case is a Category 1 flow in which the leading-edge vortex is generated and traverses the entire chord of the plate within one plunge cycle, and is shed into the wake with the like-signed trailing edge vorticity.

Figures 4.1 through 4.4 show that the LEV structure is qualitatively two-dimensional during its traversal over the chord, but develops a spanwise instability once it is shed into the wake (Figure 4.4(a)), which leads to a rapid dissipation in the structure. As the plate starts moving down (Figure 4.1(a)), multiple positive vortex structures shed from the trailing edge and the first structure shows some instability in spanwise direction as shown in Figure and 4.1(b). The LEV formation on the top surface begins at $\phi = -22.5°$ (not shown here), similar to the 2-D results. There is evidence of the generation of a positive (red) secondary vortex due to the interaction of the LEV with the surface of the airfoil in Figures 4.2(a) through 4.3(a). The initiation of LEV instability in spanwise direction can be

observed in top view of Figure 4.2(b). Also, TEV structures start to roll around each other and dissipate in the wake. At $\phi = 90°$ the LEV has separated from shear layer and started to advect downstream. By the time the vortex reaches the trailing edge (Figure 4.4(a)), very little secondary vorticity is apparent, as indicated by the isosurface. The instability in the LEV and TEV structures is more clear in the wake of Figure 4.4(a).

4.1.2 Validation of 3-D Volume Reconstruction

Uncertainty analysis of two-dimensional PIV measurements was discussed in Section 3.1. In order to assess the uncertainties associated with the 3-D volume reconstruction process described in Section 2.2.4.2, two approaches were considered. The first was to compare the $y-$component of velocity which is measured in both vertical and horizontal planes ($y-z$ planes and $x-y$ planes respectively). It was important to understand how this redundant component of velocity changes between planes, and if we can rely on the out-of-plane component measured from PIV in the normal direction. Figure 4.5 shows the ratio of difference between U_y values of the vertical planes and horizontal planes to the free-stream velocity multiplied by 100, as shown in equation 4.1 for the nominally two-dimensional plunging plate at $St = 0.2$, $h_0/c = 0.3$, $k = 1.05$, $\phi = 45°$.

$$\delta U_y = \frac{(U_y)_{z-planes} - (U_y)_{x-planes}}{U_\infty} \times 100 \tag{4.1}$$

This phase was selected because the LEV has its maximum strength. The maximum difference between the magnitude of U_y of horizontal and vertical planes is about 3% of the free stream velocity in the region close to the leading edge.In the present study, the U_y values of reconstructed flow field were calculated by taking the average of its value from the hor-

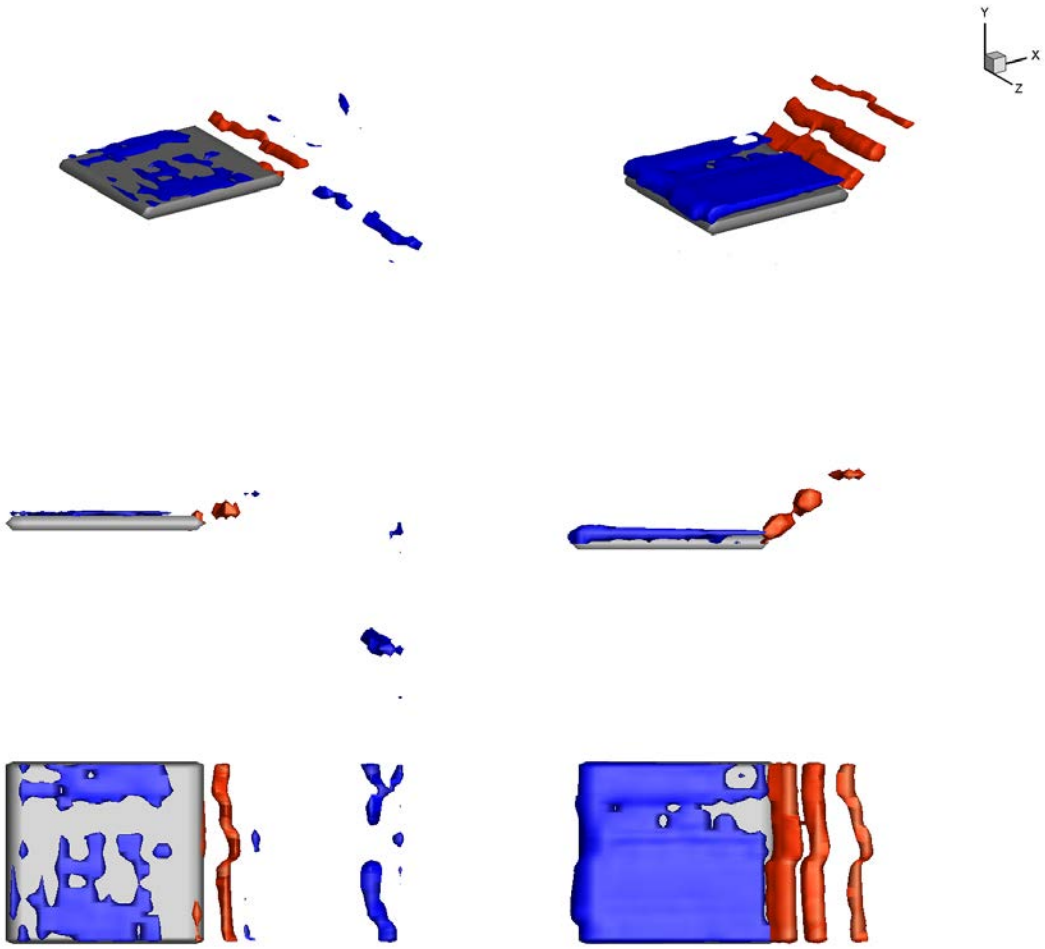

(a) (b)

Figure 4.1: Evolution of the vorticity field on the central portion of the nominally two-dimensional plunging plate at $St = 0.2$, $h_0/c = 0.3$, $k = 1.05$, a) $\phi = -90°$ and b) $\phi = -45°$. First row: isometric view, second row: side view, third row: top view.

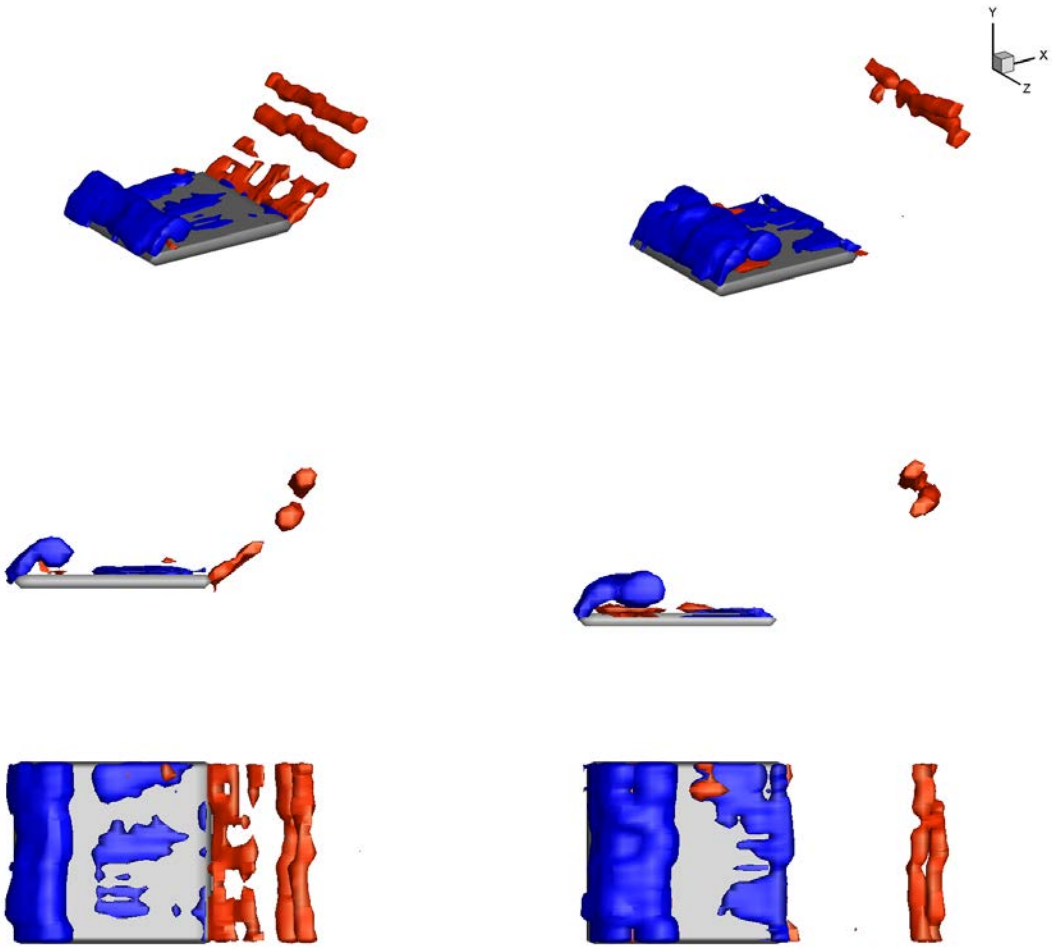

(a) (b)

Figure 4.2: Evolution of the vorticity field on the central portion of the nominally two-dimensional plunging plate at $St = 0.2$, $h_0/c = 0.3$, $k = 1.05$, a) $\phi = 0°$ and b) $\phi = 45°$. First row: isometric view, second row: side view, third row: top view.

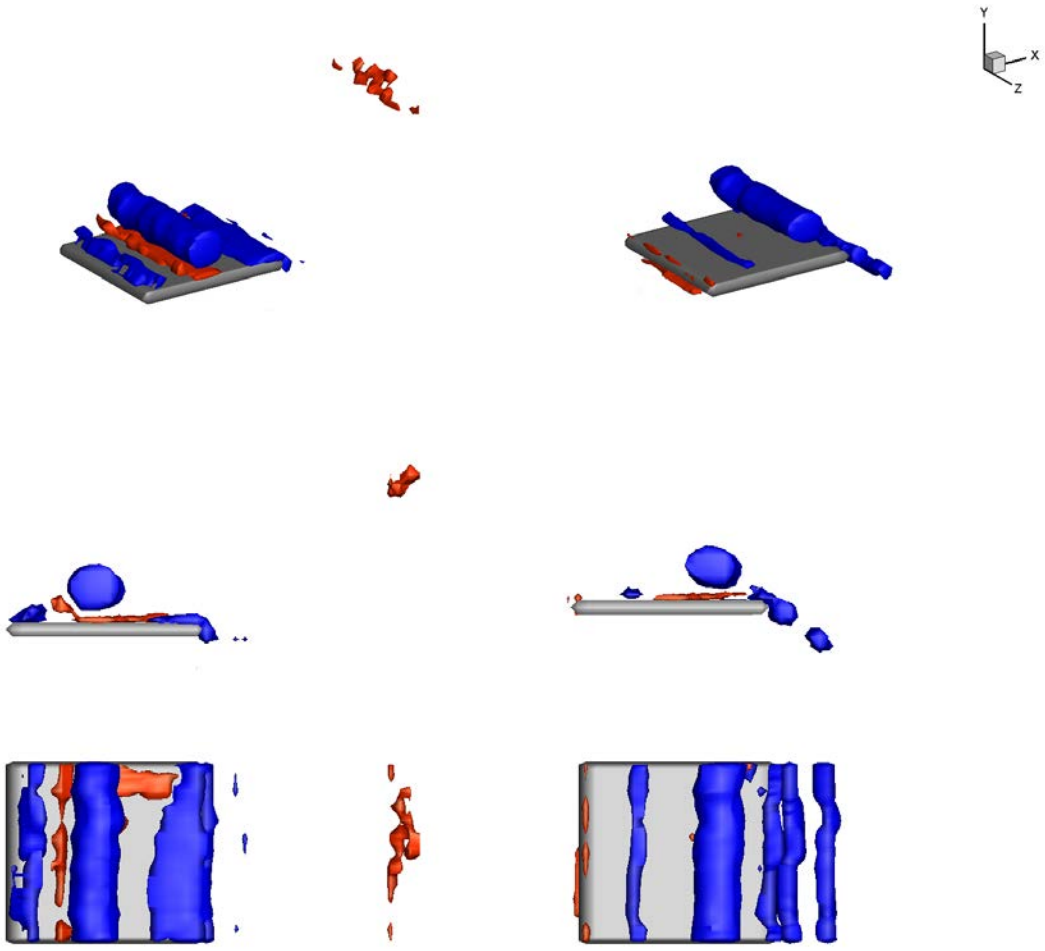

(a) (b)

Figure 4.3: Evolution of the vorticity field on the central portion of the nominally two-dimensional plunging plate at $St = 0.2$, $h_0/c = 0.3$, $k = 1.05$, a) $\phi = 90°$ and b) $\phi = 135°$. First row: isometric view, second row: side view, third row: top view.

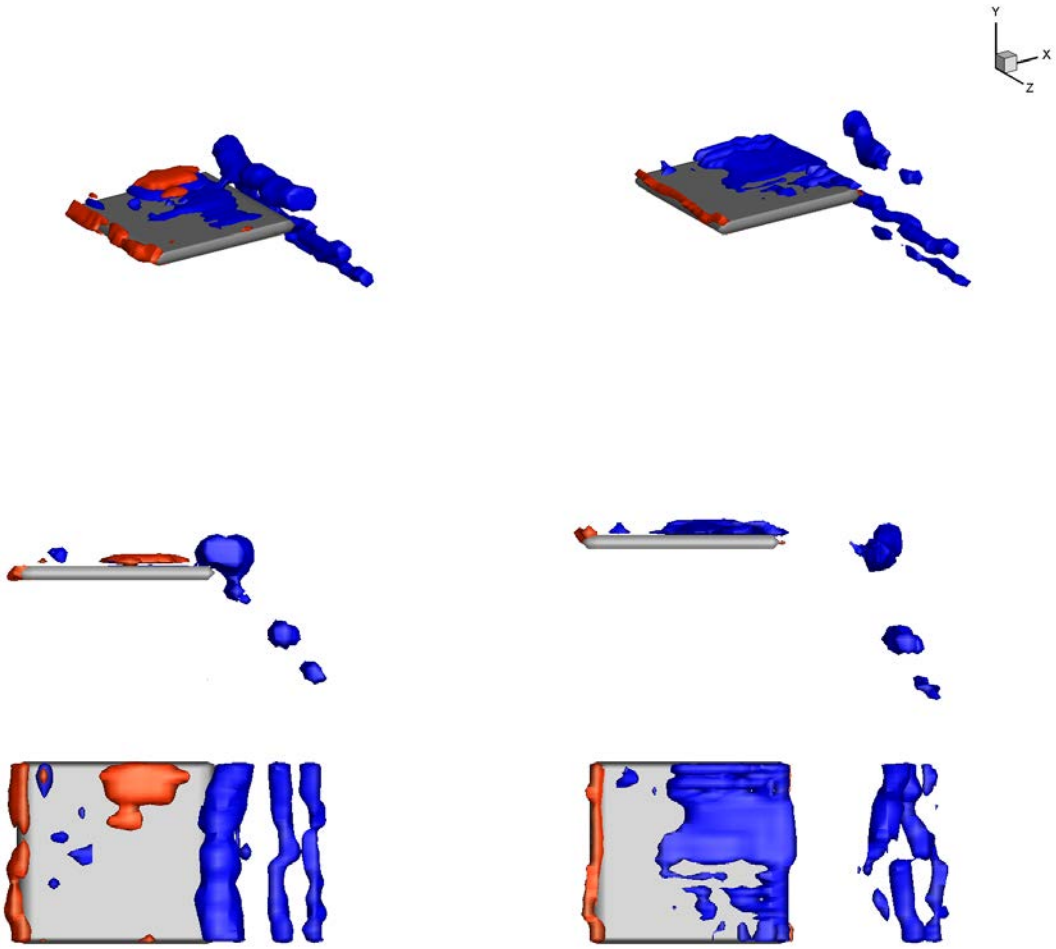

(a) (b)

Figure 4.4: Evolution of the vorticity field on the central portion of the nominally two-dimensional plunging plate at $St = 0.2$, $h_0/c = 0.3$, $k = 1.05$, a) $\phi = 180°$ and b) $\phi = 225°$. First row: isometric view, second row: side view, third row: top view.

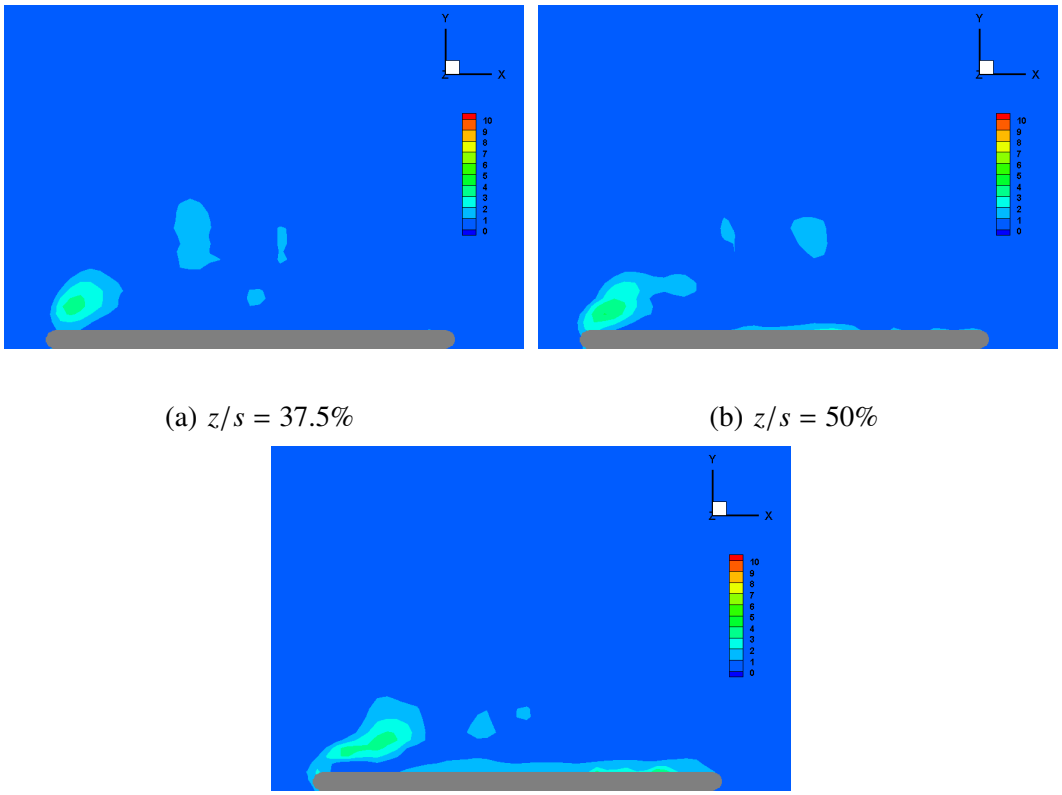

(a) $z/s = 37.5\%$ (b) $z/s = 50\%$

(c) $z/s = 62.5\%$

Figure 4.5: The percentage of δU_y as shown in equation 4.1 for the nominally two-dimensional plunging plate at $St = 0.2$, $h_0/c = 0.3$, $k = 1.05$, $\phi = 45°$, with superimposed contours of spanwise vorticity (black lines- solid lines show positive and dash lines show the negative vorticity) at different spanwise locations.

izontal and vertical planes. Therefore, the representative uncertainty of the reconstructed velocity was not greater than 3%.

The second approach to validate the reconstruction was to investigate whether the continuity in the reconstructed flow field is satisfied or not. To examine this, the following terms was computed:

$$\left(\frac{\partial u}{\partial x}+\frac{\partial v}{\partial y}+\frac{\partial w}{\partial z}\right)\overset{?}{\ll}\left(|\frac{\partial u}{\partial x}|+|\frac{\partial v}{\partial y}|+|\frac{\partial w}{\partial z}|\right) \tag{4.2}$$

The left-hand-side of equation 4.2 is the continuity equation for an incompressible flow which is ideally zero. To find out how close to zero the continuity of reconstructed velocity field is, it has been compared to the right-hand-side of equation 4.2 which is the summation of magnitude of velocity derivatives. Figure 4.6 reveals that the maximum value of the continuity term is approximately 1% of the maximum of the summation of magnitude of velocity derivatives for the case of $St = 0.2$, $h_0/c = 0.3$, $k = 1.05$ at $\phi = 45°$. Repeating these approaches for other cases reperesented similar uncertainties in the flow field.

4.2 Analysis of Vorticity Transport in the LEV

A three-dimensional vorticity transport analysis was conducted on the spanwise symmetry plane of the two-dimensional airfoil, in which the terms of the vorticity transport equation were evaluated and integrated over the boundaries and internal region of a rectangular, planar control volume, as shown in Figure 4.7:

$$\frac{\mathrm{d}\Gamma}{\mathrm{d}t}=-\int_{A_z}u_z\frac{\partial\omega_z}{\partial z}\,dA_z+\int_{A_z}\left(\omega_y\frac{\partial u_z}{\partial y}+\omega_x\frac{\partial u_z}{\partial x}\right)dA_z+\int_{1\text{ to }3}u_n\,\omega_z\,dL+\int_4-\nu\left(\frac{\partial\omega_z}{\partial y}\right)dL \tag{4.3}$$

The spatial and temporal derivatives were approximated using central differences and forward differences respectively. The left hand side is the rate of change of circulation in the control volume. On the right hand side, the terms describe (from left to right) the contribution due to the spanwise convection of a spanwise gradient in spanwise vorticity, the tilting of vorticity from the y- and x-directions into the z-direction, convection of vorticity

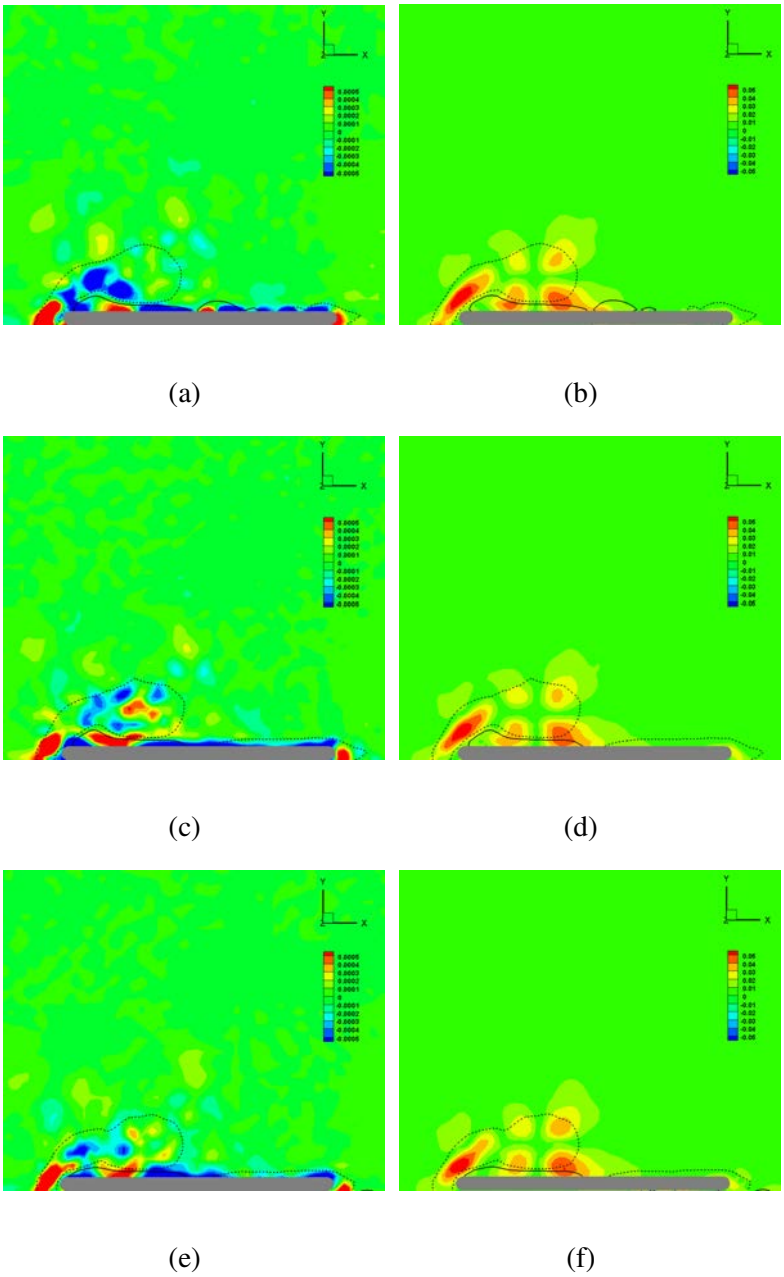

(a) (b)

(c) (d)

(e) (f)

Figure 4.6: The first collomn show the RHS of equation 4.2 and the second collomn show LHS of equation 4.2 for the nominally two-dimensional plunging plate at $St = 0.2$, $h_0/c = 0.3$, $k = 1.05$, $\phi = 45°$. First row: $z/s = 37.5\%$, second row: $z/s = 50\%$, and third row: $z/s = 62.5\%$.

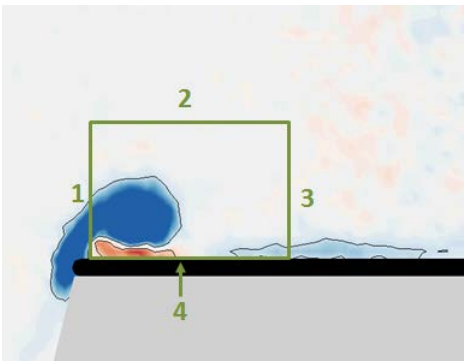

Figure 4.7: Planar control volume in which the vorticity transport analysis was conducted.

across boundaries 1 through 3 (where u_n represents the velocity component in the direction of the inward normal, and finally the diffusive flux of vorticity across the control volume boundary coincident with the surface of the plate. It should be noted that the tilting term is calculated only to better understand the magnitudes of the individual x- and y-tilting terms, as their sum should be zero since tilting cannot alter the circulation of the vortex. The diffusive boundary flux is computed from the phase-averaged surface pressure measurements described in Section 2.2.5, and the integrand is determined based on computed pressure gradients:

$$\nu\left(\frac{\partial\omega_z}{\partial y}\right)_{\text{wall}} = -\frac{1}{\rho}\left(\frac{\partial p}{\partial x}\right)_{\text{wall}}. \tag{4.4}$$

The control volume was defined such that the upstream boundary (Boundary 1) was located $0.042c$ from the leading edge coincident with the first pressure tap, and the downstream boundary was located $0.5c$ from the leading edge. Figure 4.8 shows the phase-averaged vorticity field, the surface pressure distribution, and the resulting surface vorticity flux at $\phi = -45°$ and $0°$ during the downstroke [12]. Pressures are measured on the top

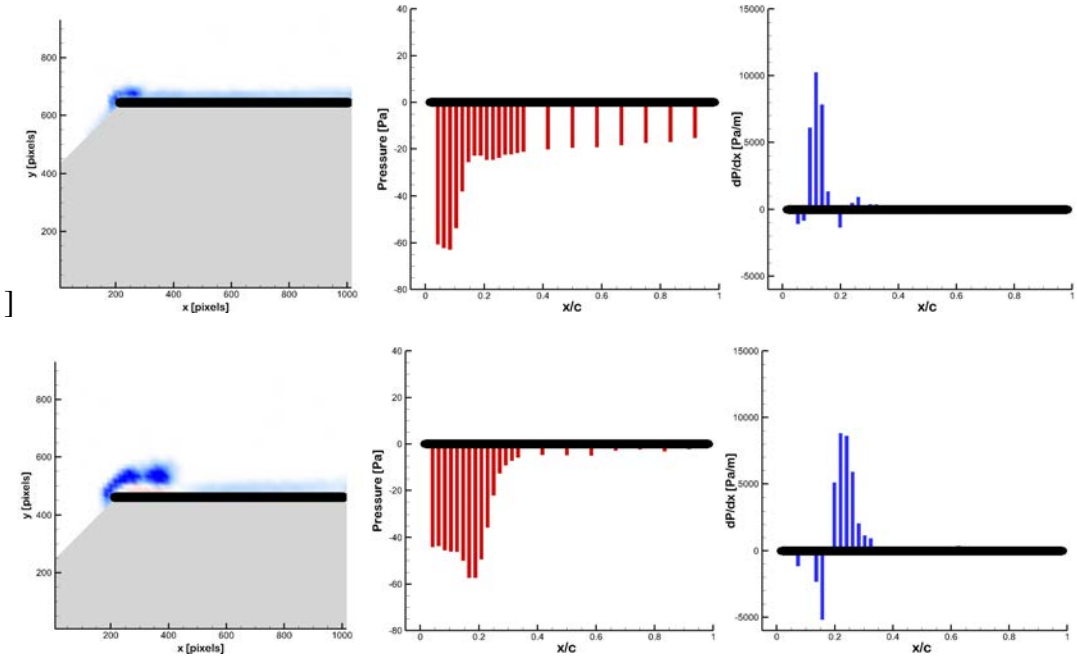

]

(b)

Figure 4.8: Vorticity field, surface pressure distribution, and pressure gradient on the top surface of the two-dimensional plate at (a) $\phi = -45°$ and (b) $\phi = 0°$.

surface of the airfoil by James Akkala. At $\phi = -45°$, the negative pressures indicated along the chord length are due to inertial effects as the airfoil accelerates downward. At both phases, a region of strong suction exists beneath the LEV, and a strong streamwise pressure gradient exists at the downstream end of the leading-edge vortex that provides a significant source of secondary vorticity, which is advected upstream by the velocity field inducted by the LEV and ultimately entrained as described in Section 3.2.

Figure 4.9 contains the values of the terms in equation 4.3 integrated in time throughout the downstroke. As Figure 4.9(a) illustrates, the shear layer flux through Boundary 1 is clearly the largest source of vorticity in the control volume. The maximum slope (max-

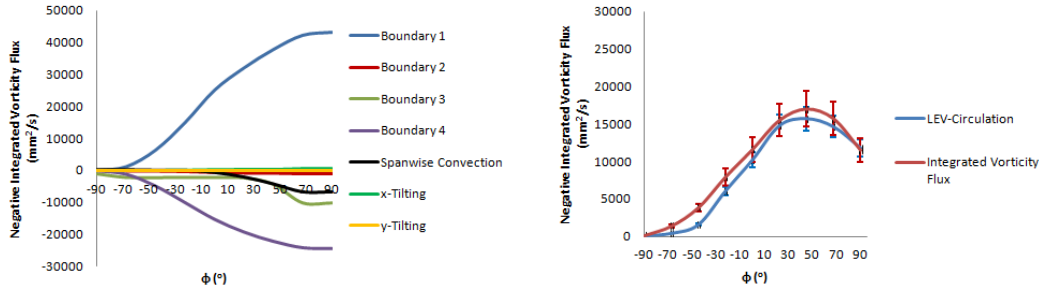

(a) (b)

Figure 4.9: (a) Integrated boundary vorticity fluxes and vorticity tilting terms, (b) the sum of the integrated fluxes vs. LEV circulation throughout the downstroke of the two-dimensional plate.

imum shear layer flux) occurs between approximately $\phi = -30°$ and -10°, then steadily declines over the second half of the stroke until it becomes approximately zero for approximately $\phi > 80°$. Interestingly, the opposite-sign pressure-gradient flux through Boundary 4 is approximately half that of the shear-layer flux, and has a similar shape – the net circulation in the control volume is significantly reduced by the boundary vorticity flux generated by the presence of the LEV itself. As Figures 4.1 through 4.4 suggest, there is very little tilting occurring within the LEV during the downstroke, as both the x- and y-tilting terms are very small. On the other hand, the flux of vorticity through Boundary 3 becomes important for $\phi > 45°$ as the LEV begins to cross the downstream boundary of the control volume. Finally, it is evident that for $\phi > 45°$, spanwise convection of vorticity provides a non-negligible sink of LEV vorticity, meaning that organized spanwise flow exists within the vortex core, as well as a spanwise gradient in the vorticity distribution. Thus, an important deviation from true two-dimensional flow is identified.

Figure 4.10 shows the spanwise velocity distribution in relation to the vorticity field at $\phi = 45^\circ$. A weak (approximately 1/5 of free-stream velocity) positive spanwise velocity is apparent above the LEV and negative spanwise velocity in the secondary vortex. It varies in strength but remains positive (downward) within the spanwise region above the LEV. It is stronger in the region close to the root at 37.5% of span and it is wider at 62.5% of span compared to the other spanwise locations. However, the size of the LEV structure does not change along the span. The origin of this spanwise velocity is not clear. It may be due to a) a growing instability within the LEV, or b) spanwise deflection of the plate. Considering the fact that the spanwise velocity was measured for only one chord length in the midspan region, it is not clear how this spanwise velocity developes in z-direction. Since the spanwise velocity of the same magnitude gets wider along the span, this suggests the LEV structure might have a tornado shape due to the interaction with the top and bottom surfaces. On the other hand, the LEV structure might have been deformed in z-direction due to the deflection of plunging plate, because the 3 mm plate thickness is very thin relative to the 300 mm plate length made of Aluminum. Moreover, the LEV and TEV structures present spanwise instability after shedding into the wake as shown in Figures 4.4(a) and 4.4(a), which might cause this positive spanwise velocity in the region of midspan.

Figure 4.9(b) shows the right hand side of Equation 4.3 integrated in time as well as the circulation contained within the control volume as a function of time. The uncertainty in the circulation is approximately 7%, whereas the uncertainty in the right side of Equation 4.3 is approximately 5% as shown in Figure 4.9(b), suggesting reasonable agreement, although the circulation is consistently lower than the sum of the integrated fluxes.

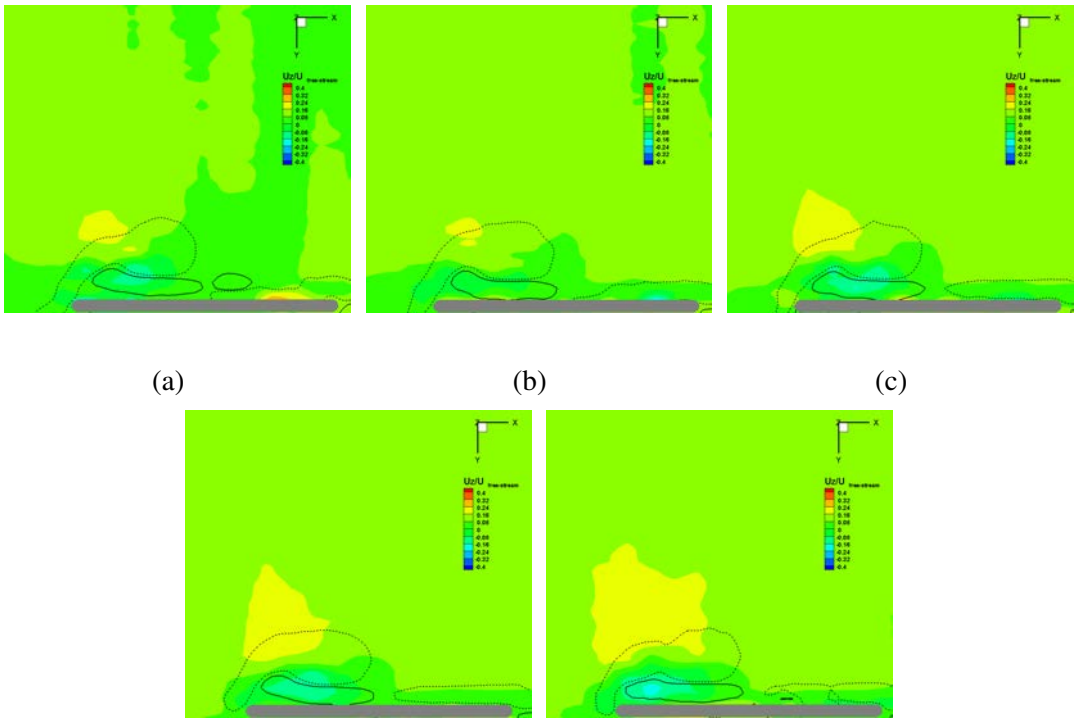

(a) (b) (c)

(d) (e)

Figure 4.10: Isocontours of spanwise velocity as a fraction of the free-stream velocity (filled color contours-red indicates root-to-tip and blue indicates tip-to-root flow) with superimposed contours of spanwise vorticity (black lines- solid lines show positive and dash lines show the negative vorticity) at different spanwise locations: a) z/s = 37.5%, b) z/s = 43.75%, c) z/s = 50%, d) z/s = 56.25%, c) z/s = 62.5% .

4.3 Insights into the Effects of Parameter Variation

Shear layer vorticity fluxes passing throught the control volume were computed for nine combinations of Strouhal numbers and non-dimensionalized plunging amplitudes as shown in Figure 4.11. The case shown in Figure 4.11(d) was discussed in section 4.2. Although the magnitude of integrated shear layer vorticity fluxes and the LEV circulations are different, the behavior of them is qualitativly similar. The slope of integrated vorticity flux is twice of the slope of the LEV circulation during downstroke. At the end of downstroke they level off and there is a deviation between the integrated shear layer vorticity fluxes and the LEV circulations at the end of downstroke. Similar to the case of $h_o/c = 0.3$, $St = 0.2$, the boundary vorticity flux is assumed to have a great influence on the LEV strength. Also, the deviation between shear layer vorticity fluxes and the LEV circulations becomes largers for higher St and h_o/c, where the flow seems to be very turbulent. This suggests that there should be some three-dimensionality effect in the flow field despite the nature of 2-D flow and there should be some annihilation which regulates the LEV strength like the spanwise convection of vorticity or the instability in spanwise direction which were observed for the case of $h_o/c = 0.3$, $St = 0.2$ (Figure 4.9(a)).

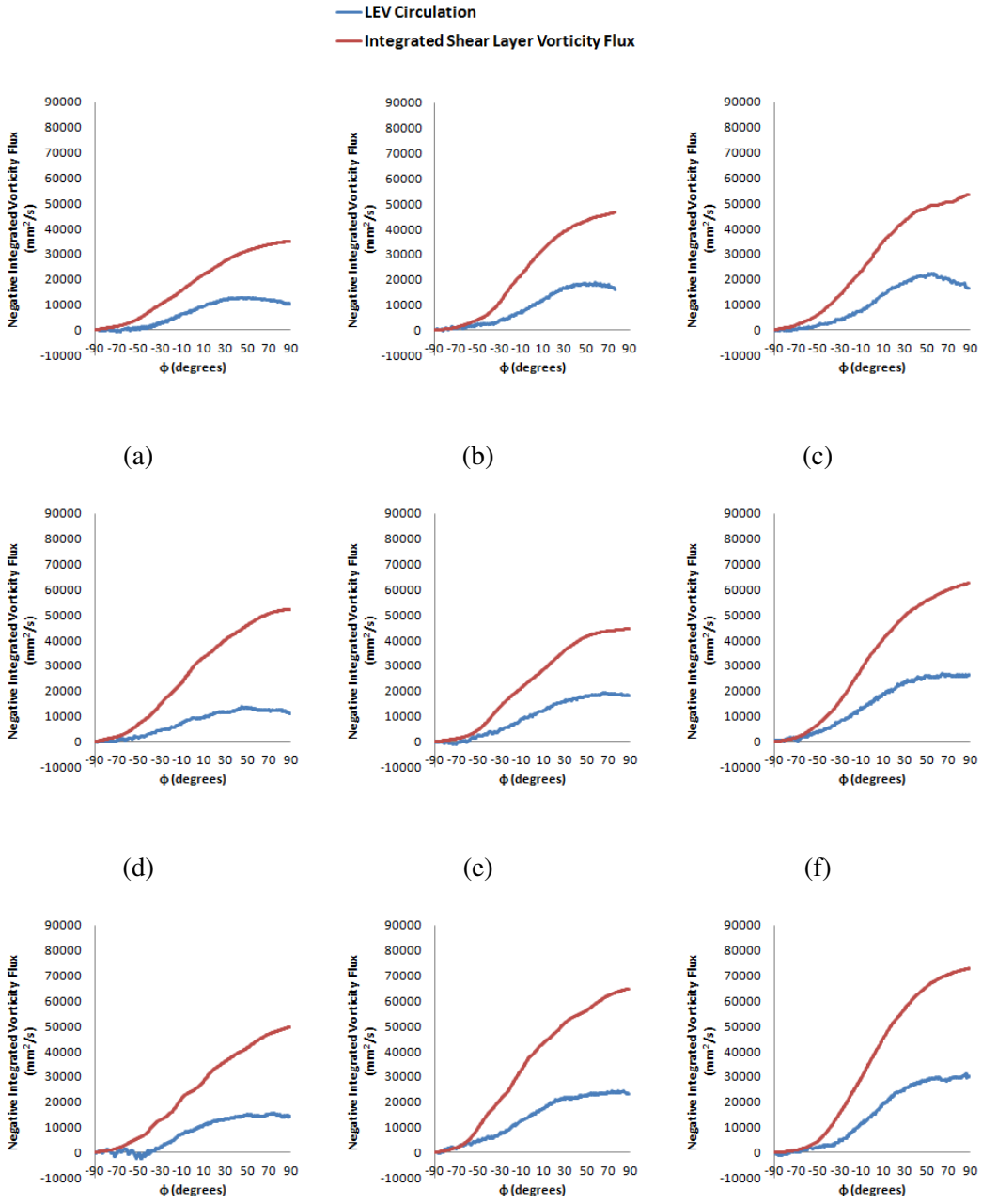

Figure 4.11: Flux analysis based on phase-averaged flow field. First row: $h_o/c = 0.2$, second row: $h_o/c = 0.3$, third row: $h_o/c = 0.4$; first colomn: $St = 0.2$, second column: $St = 0.3$, third column: $St = 0.4$.

CHAPTER 5
FLOW EVOLUTION FOR A FINITE-AR PLUNGING WING

5.1 Preliminary Vortex Dynamics on Finite-Aspect-Ratio wings

As described in Chapter 2, the same plunging kinematics were applied to finite wings with roots bounded by a no-slip wall. The physical semi-aspect ratios of the plates are $sAR = 1$ and 2, corresponding to full aspect ratios (mirrored about the symmetry plane) of $AR = 2$ and 4. This section includes the results from Stereo Particle Image Velocimetry measurements as described in section 2.2.2.

5.1.1 $sAR = 2$

In this section, we consider the vorticity and velocity fields for the finite plunging plate of $sAR = 2$ with the root plate installed (See Figure 2.5). Figure 5.1 shows a quasi-3D reconstruction of the spanwise component of the vorticity field for $St = 0.2$, $h_0/c = 0.3$ ($k = 1.05$) at $\phi = 45°$. At this phase of the plunge cycle, the LEV structure appears highly two dimensional between the 25% and 75% spanwise positions. Near the root, the LEV appears somewhat diminished. Figure 5.2 shows the plate at the bottom of the downstroke ($\phi = 90°$), where the LEV has moved further downstream. The LEV is now also significantly diminished at the 75% spanwise position. At 12.5%, the LEV is increasingly elongated and adjacent to the surface of the wing. In the mid-span region (25% to 50%), the LEV becomes further elevated off of the surface and convects downstream. These vorticity cross sections are consistent with the initial evolution of the LEV into a full arch structure over the semi-span of the wing, similar to that observed by Calderon et al [15] for the $sAR = 2$

rectangular wing.

Early in the upstroke, at $\phi = 135°$, the LEV moves further from the leading edge and becomes significantly more deformed as shown in figure 5.3. The greatest excursion from the plate is found at 37.5%, and this is also the location where the LEV has achieved the greatest streamwise displacement. This development is still qualitatively consistent with the observations of Calderon et al [15].

At $\phi = 180°$, mid-way through the upstroke, the LEV has reached the trailing edge from the 12.5% to the 37.5% spanwise locations; however, at the 50% location, the LEV is significantly retarded and it is also closer to the surface presented in figure 5.4. At the 75% spanwise position, the LEV structure is barely detectable on top of the surface. This suggests that the LEV has become highly reoriented into the streamwise direction and drawn inward on the wing such that it is substantially inboard of the 75% spanwise position.

Figs. 5.5 through 5.7 illustrate distributions of spanwise velocity in chordwise planes coincident with the vorticity distributions described above for $45° \leq \phi \leq 135°$. To better interpret the spanwise velocity field, the figures have been stretched by a factor of 2 in the spanwise direction to minimize overlap. Fig. 5.5 shows a strong root-to-tip spanwise flow near the root (12.5% and 25% spanwise positions) at $\phi = 45°$. There is also a weaker region of tip-to-root flow upstream of the LEV. This pattern of outward and inward flow is consistent with the velocity field induced by the LEV that has become tilted down toward the plate. The root-to-tip spanwise flow is significantly decreased by the mid-span region (37.5% and 50%). In the 75% spanwise plane, the pattern of spanwise flow

becomes approximately reversed – there is outward flow upstream of the LEV and inward flow downstream of the LEV, again consistent with the tilting of the LEV down toward the wing. There is also a large region of tip-to-root flow downstream along the rest of the chord. This is consistent with the induction of a separate, streamwise tip vortex outboard of the 75% spanwise position.

At $\phi = 90°$, near the root, there is still strong root-to-tip flow up to 37.5%, which can be seen in figure 5.6. At 50%, the region of tip-to-root flow has significantly strengthened, consistent with the narrowing of the LEV structure over the span of the wing as shown in Figure 5.2. At this point, root-to-tip flow is also significantly above the tip-to-root flow, supporting the assertion based on observations of the vorticity field that the LEV is tilting into the streamwise direction in this region. At $\phi = 135°$, strong spanwise root-to-tip flow is still observed near the root. This region has moved downstream consistent with vorticity field. On the other hand, tip-to-root flow is growing upstream of the LEV. Note that while the LEV structure tilts and it is not extending toward the tip, thus the circulation values might be different for vertical planes at different spanwise locations.

5.1.2 sAR=1

Figures 5.8 through 5.10 show the evolution of the vorticity and velocity fields on the $sAR = 1$ wing for phase angles in the range $45° \leq \phi \leq 135°$ for the same kinematic parameters: $St = 0.2$ and $h_0/c = 0.3$ ($k = 1.05$). Similar to $sAR = 2$, the spanwise velocity figures have been stretched twice in the spanwise direction. Figure 5.8 shows that at $\phi = 45°$, the flow is much more highly three dimensional than for the $sAR = 2$

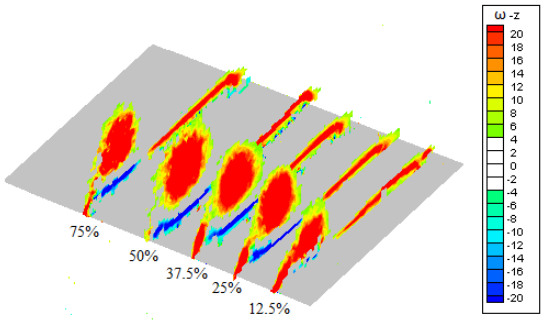

Figure 5.1: Vorticity field of $sAR = 2$ wing at $\phi = 45°$ at $St = 0.2$, $h_0/c = 0.3$

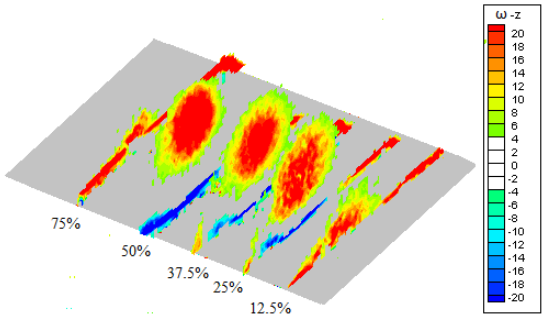

Figure 5.2: Vorticity field of $sAR = 2$ wing at $\phi = 90°$ at $St = 0.2$, $h_0/c = 0.3$

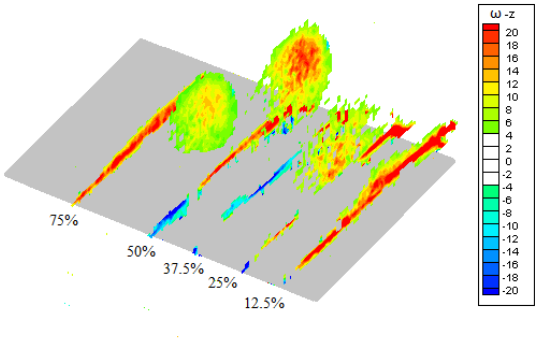

Figure 5.3: Vorticity field of $sAR = 2$ wing at $\phi = 135°$ at $St = 0.2$, $h_0/c = 0.3$

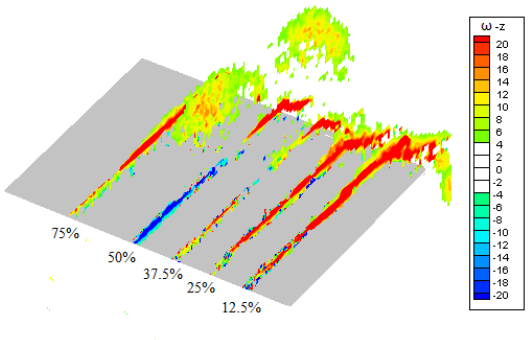

Figure 5.4: Vorticity field of $sAR = 2$ wing at $\phi = 180°$ at $St = 0.2$, $h_0/c = 0.3$

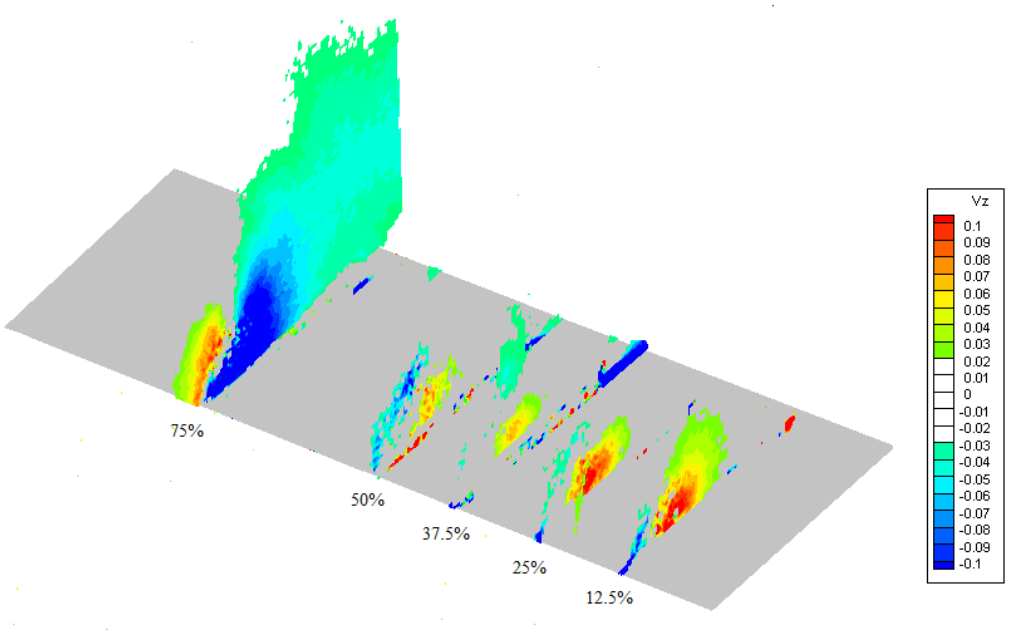

Figure 5.5: Spanwise velocity field of $sAR = 2$ wing at $\phi = 45°$ at $St = 0.2$, $h_0/c = 0.3$

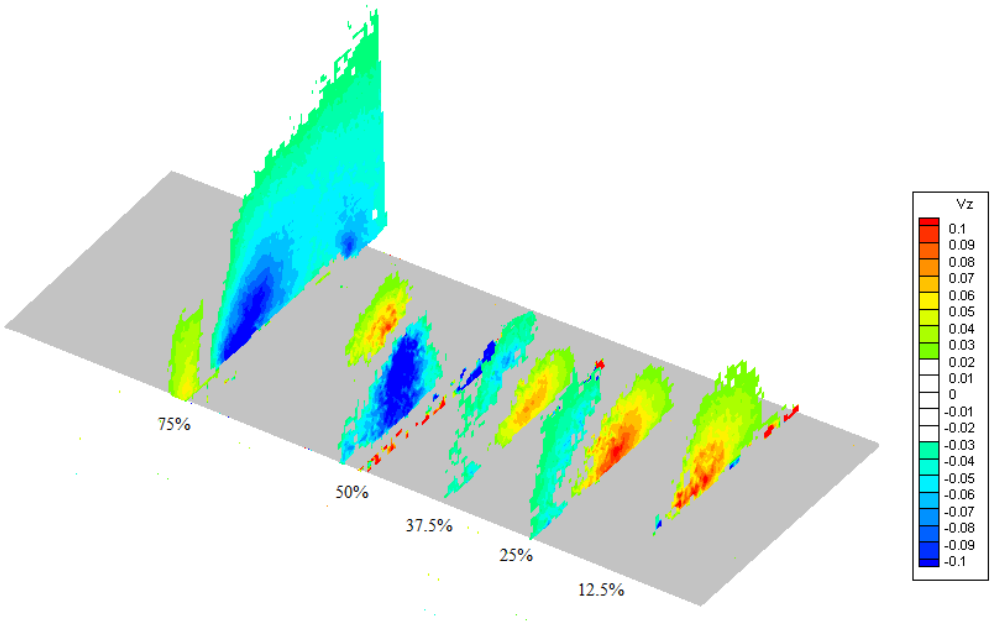

Figure 5.6: Spanwise velocity field of $sAR = 2$ wing at $\phi = 90°$ at $St = 0.2$, $h_0/c = 0.3$

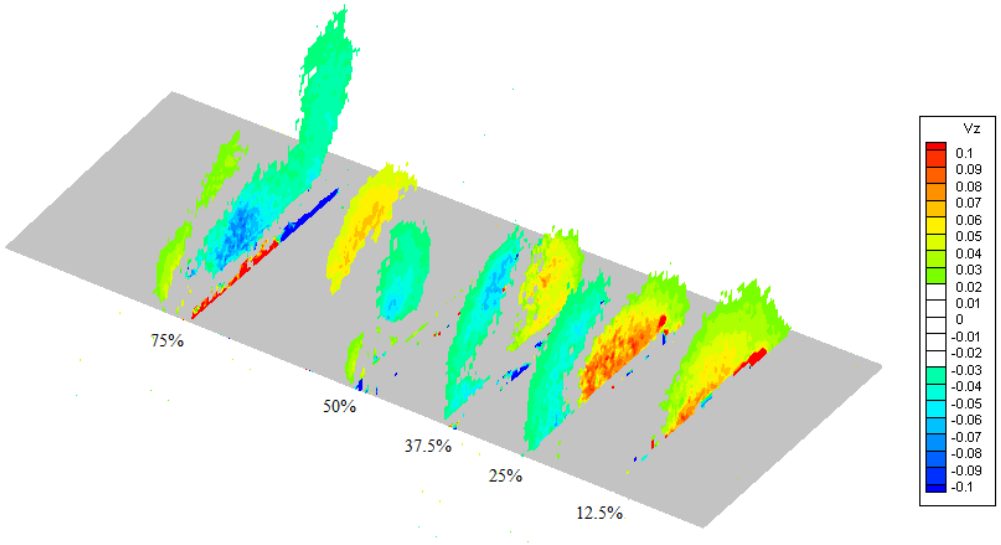

Figure 5.7: Spanwise velocity field of $sAR = 2$ wing at $\phi = 135°$ at $St = 0.2$, $h_0/c = 0.3$

wing since the cross-section of the LEV at the 75% spanwise position is now significantly weakened and adjacent to the surface of the wing. At this phase, the flow structure appears to be similar to the half arch structure observed on the semi-span wings by Yilmaz and Rockwell[82], Visbal[66], and Calderon et al.[15]. There is strong tip-to-root spanwise velocity at 75% as shown in figure 5.8(b), which decreases in the mid-span region. At 25%, the flow is reversed, and the spanwise flow here is primarily in the vortex core.

At $\phi = 90°$, the LEV becomes more diffuse at the 25% spanwise position, as shown in Fig. 5.9(a), whereas at the mid-span position (50%), the LEV cross section begins to elongate in the streamwise direction. In addition, the spanwise flow is growing due to the three dimensionality (Fig. 5.9(b)).

At $\phi = 135°$, the LEV is descending near the root, as shown in figure 5.10(a) and

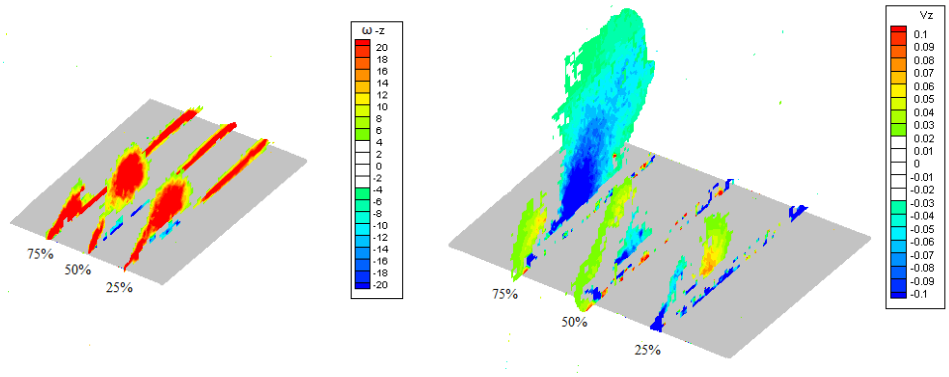

(a) Vorticity filed (b) Spanwise flow field

Figure 5.8: Vorticity and spanwise velocity field of $sAR = 1$ wing at $\phi = 45°$ at $St = 0.2$, $h_0/c = 0.3$

therefore takes on the appearance of a full-arch for $sAR = 1$ during upstroke. This is a deviation from the single arch structure extrapolated to the full-span by Visbal[66] and Calderon et al.[15]. Figure 5.10(b) explores that the spanwise velocity is stretched along the chord length and it is like vorticity is tilting. Weak vorticity and high spanwise velocity suggests that there is a highly streamwise oriented vortex on top of the surface.

5.2 Effect of Root Boundary Conditions

Whereas all previous results in Chapter 3 and 4 was obtained at the mid-span of the on the nominally 2D plunging plate, also the scaling parameter of Buchholz et al. (2011) established from measurements on the symmetry plane of a pitching symmetric panel, the fix plate at the top surface of the water will form a no-slip plane in the experiments for the finite wing. It is not entirely clear what influence this boundary condition will have on the

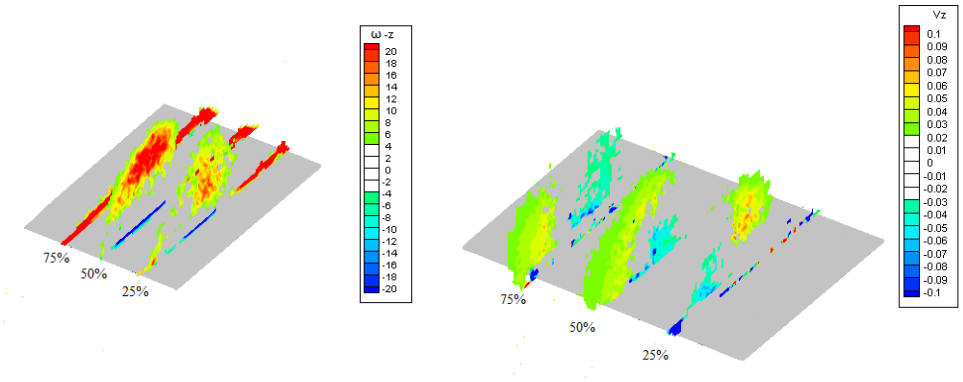

(a) Vorticity filed (b) Spanwise flow field

Figure 5.9: Vorticity and spanwise velocity field of $sAR = 1$ wing at $\phi = 90°$ at $St = 0.2$, $h_0/c = 0.3$

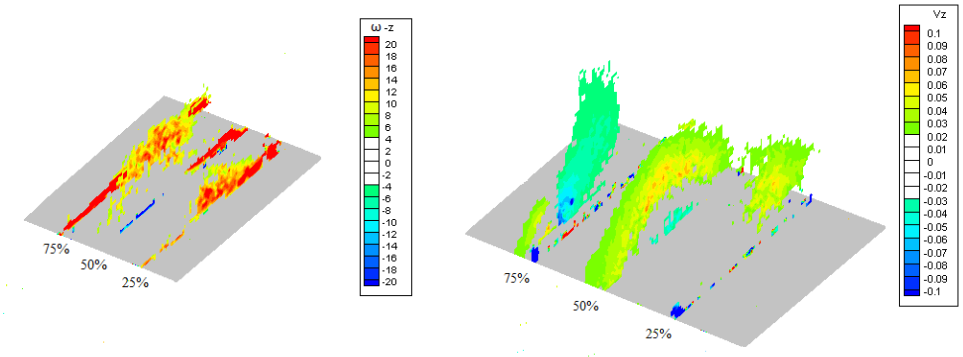

(a) Vorticity filed (b) Spanwise flow field

Figure 5.10: Vorticity and spanwise velocity field of $sAR = 1$ wing at $\phi = 135°$ at $St = 0.2$, $h_0/c = 0.3$

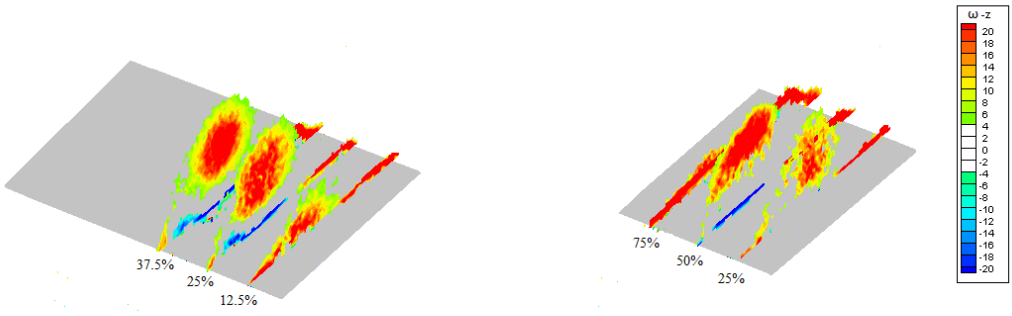

(a) (b)

Figure 5.11: Effect of root plate on vorticity field for dimensional spanwise location of plunging plate with root plate at $\phi = 90°$ at $St = 0.2$, $h_0/c = 0.3$ for a) $sAR = 2$, b) $sAR = 1$

structure and dynamics of vorticity shed by the wing, since the interaction of vortices with wall-bounded shear layers is known to generate (sometimes significant) axial flows in the vortex core, and these flows have been shown to alter vortex circulation [6, 7, 19, 39].

A comparison of the same dimensional distances from the root plate as illustrated in Figure 2.5 on $sAR = 2$ and $sAR = 1$ plunging wing with $St = 0.2$, $h_0/c = 0.3$ ($k = 1.05$) is shown in figure 5.11. It reveals that close to the root, the LEV of $sAR = 2$ at 12.5% is descending toward the surface of the plate; however, for $sAR = 1$ at 25%, a large LEV structure is on the top surface which might intersect the root plate rather than the plunging plate. Therefore, on the $sAR = 1$ wing, the LEV is more close to represent half-arch for $sAR = 1$, consistent with Visbal's and Calderon's study.

The experimental three-dimensional phased-averaged flow structure of $sAR = 2$ with the root plate compared to $sAR = 2$ without the root plate is represented in figure

5.12. The vorticity field reveals that the LEV of the wing with the root plate at 25% is weaker than 50% but it is not clear what happens at the root (Fig. 5.12(a)). However, as we showed in figure 5.2, at 12.5%, the LEV is descending to form the arch-type structure on the top surface. The LEV of the wing without the root plate, at 25% is much weaker than that of the wing with root plate, suggesting that the root acts more like the tip of the wing and the LEV is more pronounced compared to the case with the root plate. This is also due to the gap between the top of the plate without root plate and the top surface plate.

Regions of strong root-to-tip flow coincident with the vortex core at the most inboard locations strongly suggests that the root boundary condition plays an important role in the generation of spanwise flow. In previous studies for the cases of the inviscid symmetry plane (numerical simulations in Visbal[66], 3D streamlines in Fig. 4 and transverse velocity fields in Fig. 18) or the full-span experiment (Yilmaz and Rockwell[82], velocity vectors in Fig. 3), there was no corewise flow near the symmetry plane, therefore the corewise flow in our study is most likely caused by the root boundary condition.

5.3 3-D Flow Evolution on the $sAR = 2$ Wing

Since the no-slip wall boundary condition acted like root which might be caused by the significant gap in the stationary wall case, the stationary root boundary condition was modified. To reduce the effects of root boundary conditions on flow evolution and to avoid the inflow and outflow from the slot in the top plate, the gap between the top of the bracket (which mounted the airfoil or wing to the scotch yoke mechanism) and the top plate has been minimized to less than 1 mm as shown in Figure 2.7. Similarly, a gap of

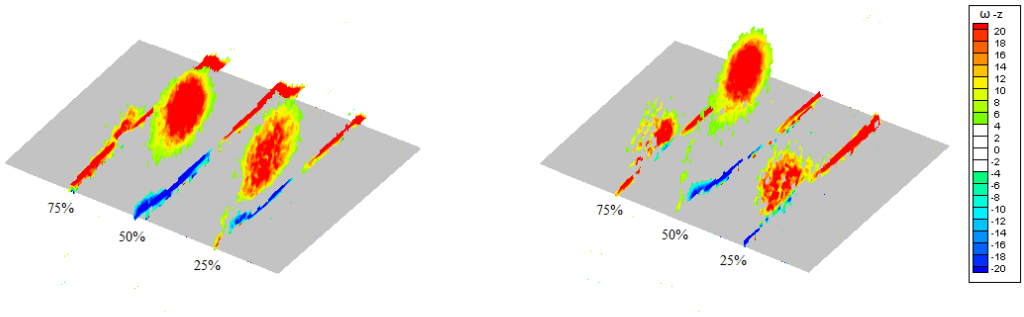

(a) (b)

Figure 5.12: Effect of root plate on vorticity field for $sAR = 2$ plunging plate at $\phi = 90°$ at $St = 0.2$, $h_0/c = 0.3$ a) with root plate and 2) without root plate.

less than 2 mm existed between the bottom of the airfoil and the bed of the water channel. For the rest of this study, this root boundary condition was used and the spanwise locations are measured with respect to the top of the holding bracket. Taking the preliminary results of $sAR = 2$ wing, this section includes the results from two-dimensional Particle Image Velocimetry measurements from two point of view as described in section 2.2.4 using 3-D volume reconstruction method as described in section 2.2.4.2.

Figures 5.13 through 5.16 illustrates the isosurfaces of the Q-criterion[35] ($Q = 5$) on the rectangular wing of $AR = 2$ for $k = 1.05$, $St = 0.2$, and $h_0/c = 0.3$, matching the kinematics of the nominally two-dimensional plate. Again, each reconstruction is phase-averaged from 100 velocity fields. First of all, the modified root boundary condition acts like the moving root plate comparing the results shown in Figures 5.1 and 5.14(b) at $\phi = 45°$. At this phase, the LEV structure appears highly two dimensional over the wing, and

only near the root, the LEV appears somewhat diminished. Also, Figure 5.15(a) and 5.2 show the plate at the bottom of the downstroke ($\phi = 90°$), where near root the LEV is increasingly elongated and adjacent to the surface of the wing. These comparison confirms that the modified root boundary condition is sufficiently acts like a symmetry plane. In the mid-span region, the LEV becomes further elevated off of the surface and convects downstream. These vorticity cross sections are consistent with the initial evolution of the LEV into a full arch structure over the semi-span of the wing, similar to that observed by Calderon et al [15] for the $sAR = 2$ rectangular wing with symmetry plane at root.

The shedding of vorticity from the finite-aspect-ratio wing is somewhat delayed in comparison to the nominally two-dimensional wing, similar to the preliminary results. This is particularly evident in the development of the leading edge vortex up to $\phi = -45°$. A rapid decrease in the size of the LEV is also evident near the tip of the wing, which signals the beginning of a rapid three-dimensional deformation of the LEV that causes the inboard portion to lift off of the wing surface to form an arch-like structure as it advects downstream along the chord through the mid-portion of the stroke (Figures 5.15(a) and 5.15(b). Early in the upstroke, at $\phi = 135°$, the LEV moves further from the leading edge and becomes significantly more deformed as shown in figure 5.15(b). At $\phi = 180°$, the LEV has become highly reoriented into the streamwise direction and drawn inward on the wing such that it is substantially inboard of the 75% spanwise position. Also, there must be the possibility that it has become obliterated through interactions with the surface.

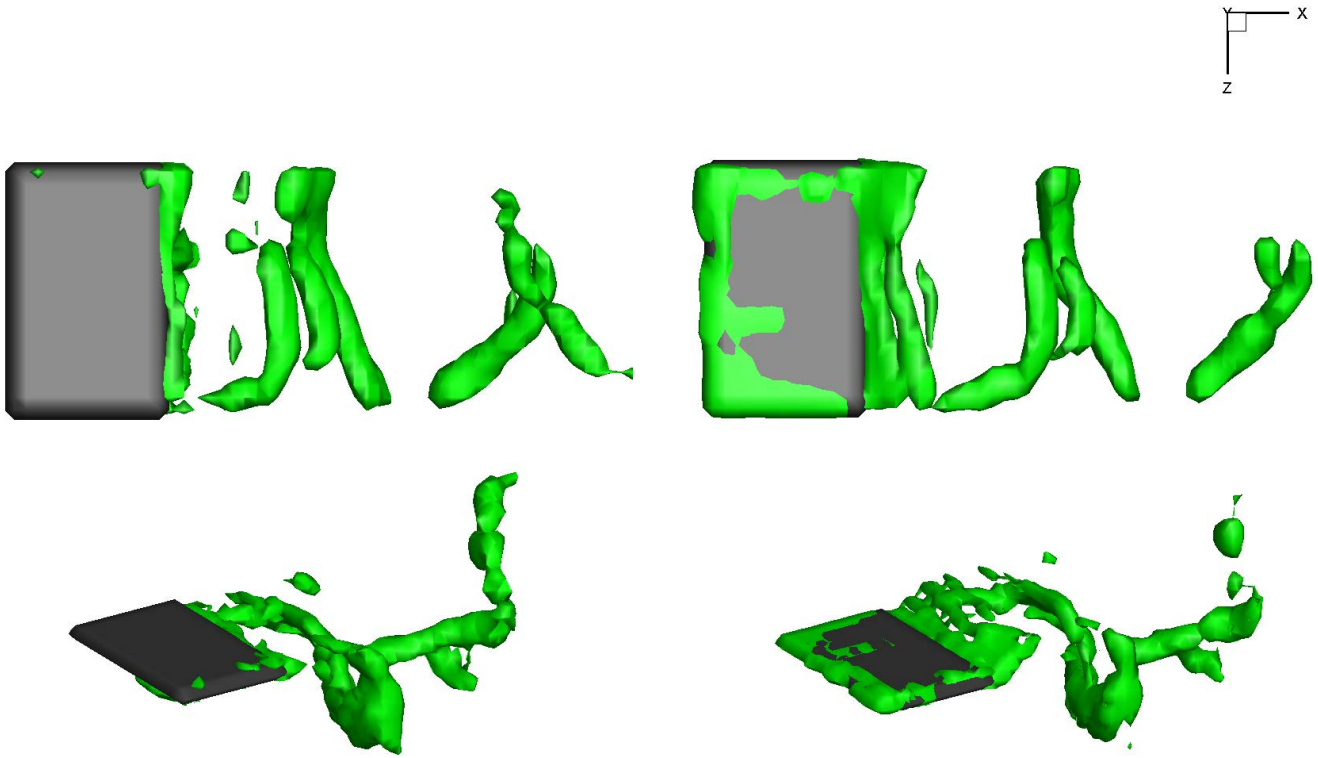

(a) $\phi = -90°$ (b) $\phi = -45°$

Figure 5.13: Evolution of the iso-Q (Q=5) field on the plunging plate of aspect ratio 2 at $St = 0.2$, $h_0/c = 0.3$, $k = 1.05$.

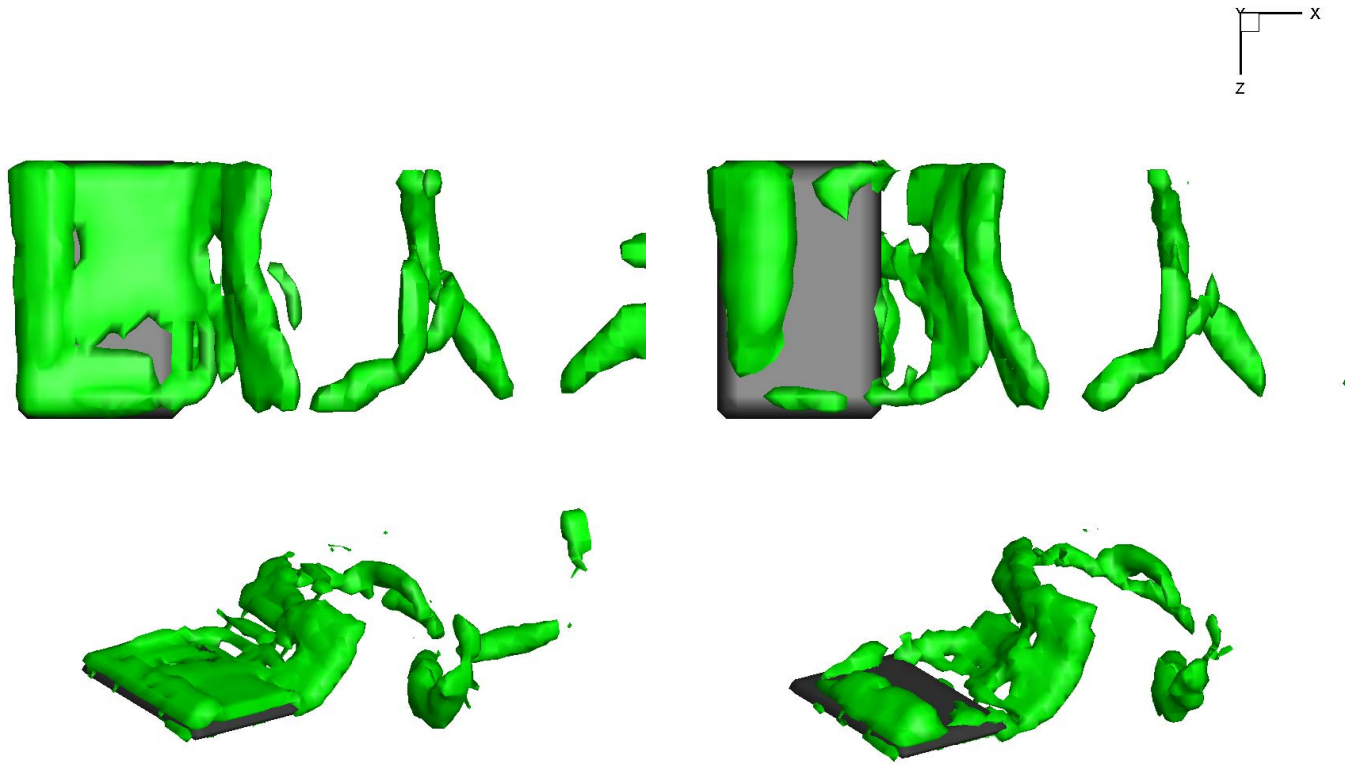

(a) $\phi = 0°$ (b) $\phi = 45°$

Figure 5.14: Evolution of the iso-Q (Q=5) field on the plunging plate of aspect ratio 2 at $St = 0.2$, $h_0/c = 0.3$, $k = 1.05$.

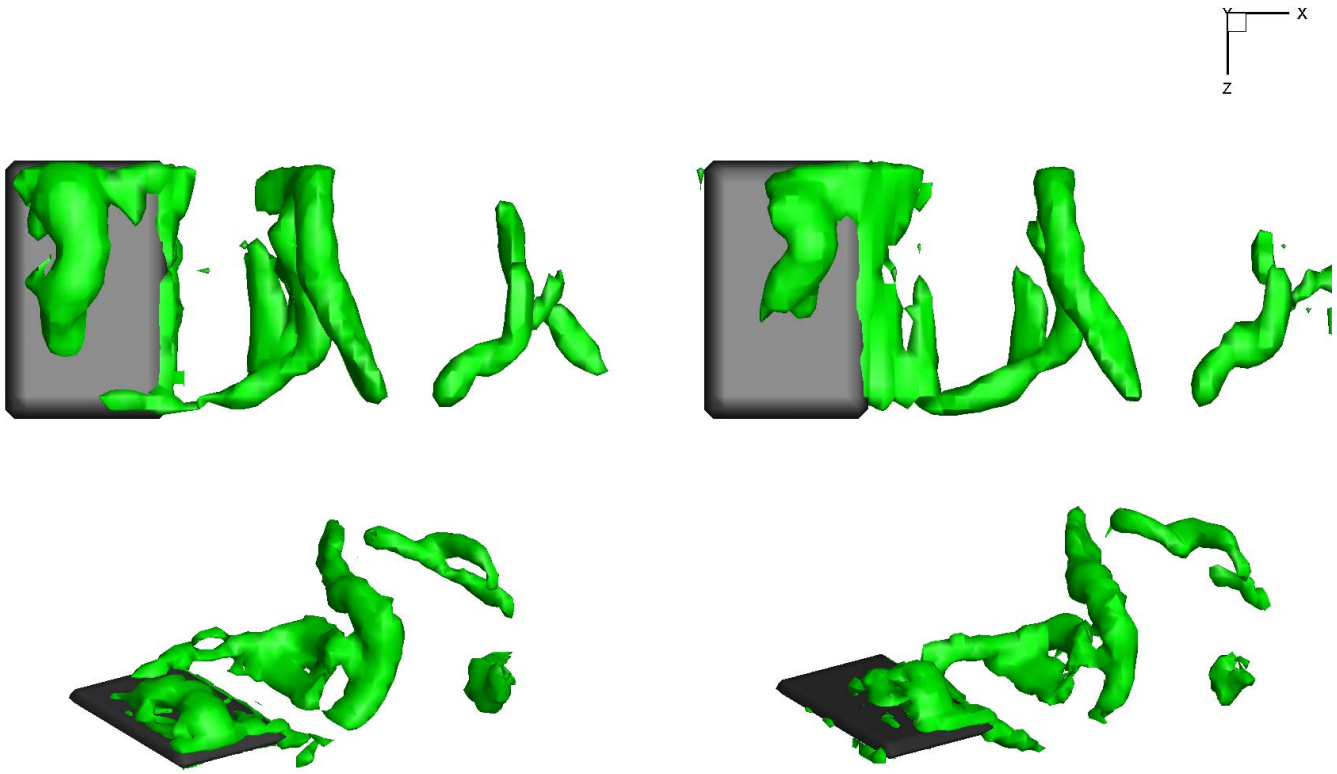

(a) $\phi = 90°$ (b) $\phi = 135°$

Figure 5.15: Evolution of the iso-Q (Q=5) field on the plunging plate of aspect ratio 2 at $St = 0.2$, $h_0/c = 0.3$, $k = 1.05$.

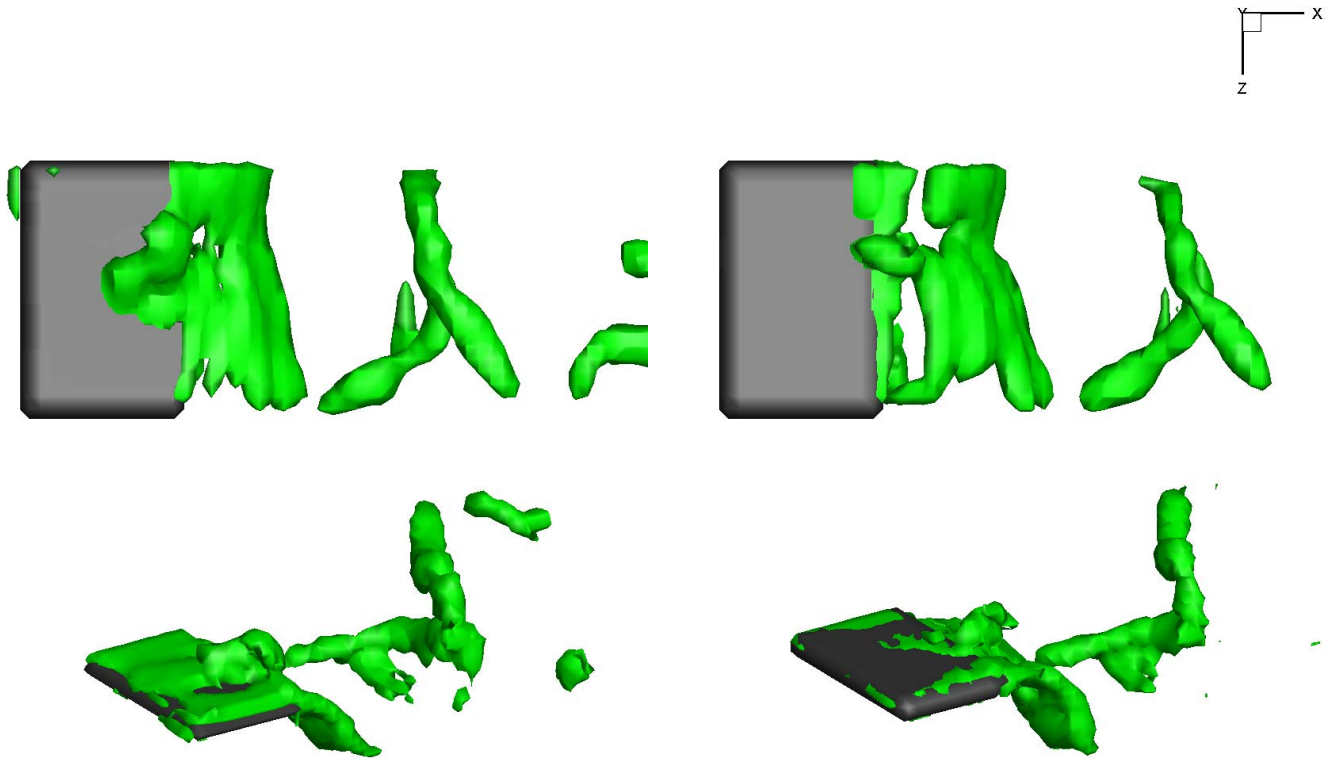

(a) $\phi = 180°$ (b) $\phi = 225°$

Figure 5.16: Evolution of the iso-Q (Q=5) field on the plunging plate of aspect ratio 2 at $St = 0.2$, $h_0/c = 0.3$, $k = 1.05$.

5.4 Vorticity Transport on the $sAR = 2$ Wing

To further understand the evolution of the arch-type structure, we will repeat the 3D flux analysis described in section 4.2 at different spanwise locations on the wing. The integrated values of the terms in Equation 4.3 are shown in Figure 5.17(a) during the downstroke, at the 50% spanwise position on the $sAR = 2$ wing. This location corresponds approximately to the spanwise position of the middle of the LEV arch. As expected, and similar to the 2D plate, the shear layer flux provides the greatest contribution to LEV circulation. However, LEV circulation remains much lower than the integrated shear layer flux. Moreover, spanwise flow provides a more significant sink of negative (LEV) vorticity than for the 2D plate. However, the rate of change of circulation due to the spanwise flux does not become significant until approximately $\phi = 0°$ when the LEV rolls up. The flux (slope in the curve) continues to be significant until near the bottom of the downstroke (approximately $\phi = 70°$) after the arch is formed. The 50% spanwise plane approximately bisects the arch structure so, despite the significant deformation of the LEV, there is little tilting of vorticity in this plane.

Figure 5.17(b) compares the right hand side of Equation 4.3 integrated in time as well as the circulation contained within the control volume as a function of time for $sAR = 2$. The sum of the fluxes through boundaries 1 through 3 and the spanwise convection flux is approximately double that of the resulting LEV circulation. The surface pressure measurements have not yet been conducted on the finite wing, and therefore the boundary vorticity flux from the plate surface has not been included. Since for the 2D plate, the boundary vorticity flux was approximately half of the shear layer flux, this would suggest

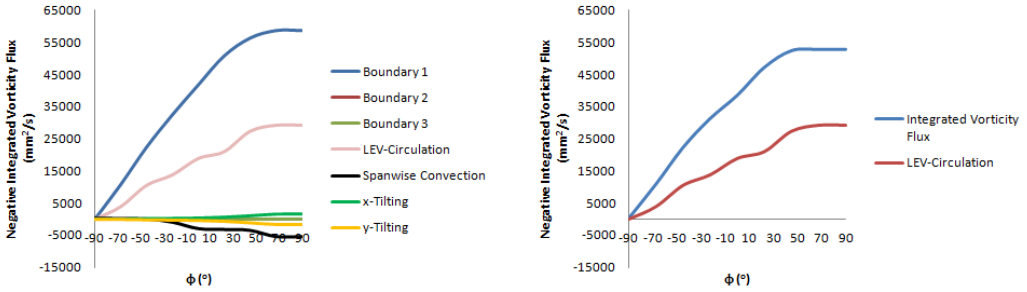

(a) (b)

Figure 5.17: Integrated vorticity transport terms for the wing of sAR=2 at the 50% of spanwise position.

a similar influence of the boundary flux in the finite wing at this position.

Figure 5.18 shows the integrated values of the terms in Equation 4.3 for the $sAR = 2$ wing at the 25% (close to root) and 75% (close to tip) of spanwise position. The shear layer flux (boundary 1) is similar in magnitude at the 25% spanwise position as it is at the 50% spanwise position; however, it is slightly lower at the 75% spanwise position despite being so close to the tip. The LEV circulation is also similar in magnitude at all three spanwise positions. At the 25% spanwise position, the rate of change of circulation due to the spanwise flux is about 25% larger than that at the 50% spanwise position. Although, this requires further investigation to better understand the cause of the spanwise flow, it is likely related to highly three-dimensional flow near the root due to evolution of the LEV into an arch as well as interaction with the top plate at the root. It is also evident that, at the 25% spanwise position, the $x-$ and $y-$tilting terms are highly asymmetric, suggesting the breakdown of the assumption that the LEV behaves as a vortex tube.

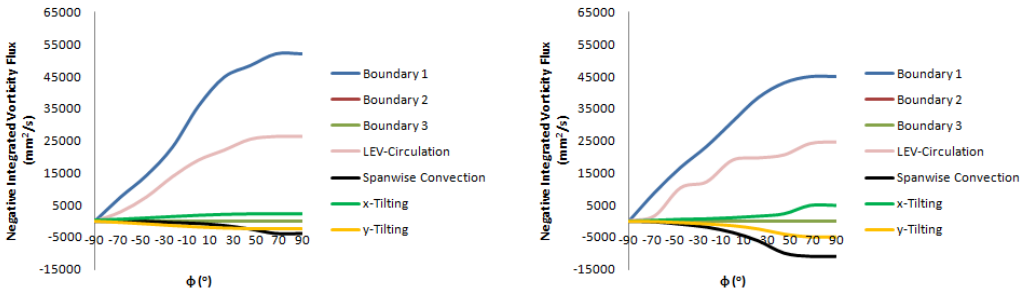

(a) (b)

Figure 5.18: Integrated vorticity transport terms for the wing of sAR=2 at the (a) 25% (b) 75% of spanwise position .

CHAPTER 6
CONCLUSIONS AND FUTURE WORK

6.1 Conclusions

In chapter 3, the evolution of the leading- and trailing-edge vortex structures shed from a nominally two-dimensional, plunging flat-plate was investigated at $Re_c = 10,000$ using particle image velocimetry, and the trajectories of the LEV cores were quantified. Leading-edge vortex circulation was found to be highly sensitive to Strouhal number within the range $0.3 < St < 0.5$, concurrent with an accelerated roll-up of the leading-edge vortex. Despite an increased importance of Strouhal number, for $St \gtrapprox 0.4$, on the evolution and structure of vorticity shed from the leading and trailing edges, interactions between the leading- and trailing-edge vortices – and therefore also the resulting wake patterns – were found to depend primarily on reduced frequency.

For the parameter space considered, four categories of wake patterns were observed based on the nature of the interaction between the leading- and trailing-edge vortex structures. These categories were found to depend primarily on reduced frequency within the parameter range investigated. In category 1 wakes, which were observed for $0.52 \leq k \leq 1.18$, the leading edge vortex merges with like-signed vorticity shed from the trailing edge in the subsequent stroke. In category 2 wakes, which were consistently observed at $k = 1.57$, the LEV passes the trailing edge after the like-sign trailing edge vortex system is shed in the subsequent stroke, and interacts with the following stronger, opposite-signed trailing-edge structures to form a dipole that results in a wide wake. Category 3 wakes were observed

only for $St = 0.3$ and $h_0/c = 0.2$ ($k = 2.36$), where the LEV is further delayed (with respect to the phase of oscillation) so that it passes the trailing edge after the opposite-sign TEV system one full cycle after its own generation. Category 4 wakes, which were observed for $k > 1.96$, are defined as those in which the LEV either does not pass the trailing edge, or resides on the surface of the airfoil for at least three strokes such that it is very weak when it is finally released into the wake. Generation of category 4 wakes are attributed to small displacements of the LEV during a stroke, which are governed by two factors: a) short airfoil plunging periods due to the high reduced frequencies for which they occur, and b) stronger Biot-Savart induction of the LEV due to significant increases in LEV circulation. In addition, at $St = 0.6$ with $h_0/c = 0.4$, a deflected category 4 wake was observed.

Comparison with computed and experimentally measured wakes by Lewin and Haj-Hariri [43] and Lua et al. [46], respectively, at Reynolds numbers an order of magnitude lower, yielded mostly similar results, also demonstrating validity of the proposed classification system through extended regions of the parameter space. However, category 1 wakes were also observed in the data of Lua et al. [46] for large Strouhal number and reduced frequency, which is inconsistent with the present results. This indicates the importance of Reynolds number and airfoil shape on wake structure, and suggests more studies of vortex formation and evolution, including characterization of the shear layers feeding the vortices, and the nature of interactions with the airfoil surface and opposite-sign layer beneath the LEV.

In chapter 4, the three-dimensional flow field was characterized for a plunging two-dimensional flat-plate airfoil using three-dimensional reconstructions of planar PIV

data. Whereas the phase-averaged description of the flow field shows the secondary vortex penetrating the leading-edge shear layer to terminate LEV formation on the airfoil, time-resolved, instantaneous PIV measurements show a continuous and growing entrainment of secondary vorticity into the shear layer and LEV. A planar control volume analysis on the airfoil indicated that the generation of secondary vorticity produced approximately one half the circulation, in magnitude, as the leading-edge shear layer flux. A small but non-negligible vorticity source was also attributed to spanwise flow toward the end of the downstroke. Wojcik and Buchholz [78] showed that cross-cancelation of LEV vorticity appears to be a robust and significant mechanism of LEV regulation, which is still not well understood. To predict the flow evolution and aerodynamic forces on flapping mechanisms, it is necessary to understand how the vorticity transport is affected by geometry and kinematics parameters.

In chapter 5, first the evolution of the LEV structure on finite-AR wings with similar kinematics to the nominally 2D cases was studied experimentally using stereo-PIV in multiple chordwise planes. The results show that LEV development during the cycle depends primarily on aspect ratio; however, the wall boundary condition was found to be also important in generation of spanwise flow within the vortex core. For both aspect ratios, $sAR = 1$ and $sAR = 2$, A single- or double-arch LEV structure was observed, qualitatively similar to Yilmaz and Rockwell [82], Visbal [65], and Calderon et al. [15]. For $sAR = 1$, some descent of the arch near the wall suggests a deviation from the full-span case. For $sAR = 2$, increased descent of arch near the wall supports double-arch structure, observed by Calderon et al. [15]. Regions of strong root-to-tip flow coincident with the vortex core

at the most inboard locations strongly suggest that the no-slip wall plays an important role in the generation of spanwise flow. The influence of the no-slip wall in creating spanwise flow is further supported by the observations of spanwise flow without the root plate. Although spanwise flow is observed near the root in all cases, axial flow is not apparent in the core of vortex structure, independent of root boundary conditions.

Furthermore, the 3-D flow field of a finite wing of $sAR = 2$ was characterized using three-dimensional reconstructions of planar PIV data after minimizing the gap between the plunging plate and the top stationary wall. The LEV on the finite wing rapidly evolved into an arch structure centered at approximately the 50% spanwise position, similar to previous observations by Calderon et al. [16], and Yilmaz and Rockwell [82]. At that location, the circulation contribution due to spanwise flow was approximately half that of the shear layer flux because of the significantly greater three-dimensionality in the flow. Increased tilting at the 25% and 75% spanwise locations suggests increasing three-dimensionality at those locations compared to the symmetry plane of the arch (50% spanwise location). The deviation between the LEV circulation and integrated convective vorticity fluxes at the 50% spanwise location suggests that entrainment of secondary vorticity plays a similar role in regulating LEV circulation as in the 2D case. While the wing surface flux of vorticity could not be measured in that case, the significant difference between LEV circulation and the known integrated fluxes is comparable to that for the 2D plate, suggesting that a significant boundary flux of secondary vorticity may exist.

6.2 Future Work

Studying flow evolution on pure plunging flat plate airfoil/wing which simplified the kinematics and geometry by minimizing the number of parameters that describe the problem, helped to somewhat understand the wake structures of unsteady propulsors. As a result, a classification scheme has been developed for structures produced by the plunging airfoil based on the nature of the LEV and TEV's interaction and the resulting structure of the wake. However, the relation between the aerodynamic loads and these shedding patterns is not understood yet while prediction of aerodynamic forces is a critical area for designing micro-aerial vehicles. Of equal importance, understanding the evolution of the shed vorticity can provide insight into flow interactions within bird flocks and fish schools, as well as the control of biorobotic vehicles.

Yilmaz and Rockwell (2010), Visbal (2011), and Calderon et al (2012) studied just the formation and evolution of LEV on top of the plate, but it is not clear exactly what happens to this LEV in the wake. Furthermore, the existence of LEV in the wake presents a challenge to current models of vortex wakes for pitching panels where the LEV is absent. Therefore, in the interests of understanding the physics of bird and insect flight and aquatic animal swimming, it is necessary to characterize the qualitative ultimate wake structure of a plunging finite-AR wing.

One of the overarching goals of this work is to develop insight into the flow physics of local vorticity transport where the generation and vorticity transport in the Leading-Edge Vortex of a flapping wing needs further investigation considering other kinematics and geometries to develop robust and physics-based models of leading-edge vortex formation

and evolution. Of particular interest is the relationship between the vorticity field and the spanwise flow field over the wing, the vortex core axial flow, and vortex tilting and stretching which indicate the vortex breakdown. To gain further insight into the physics of plunging wings, it will be very useful to measure the time-resolved pressure distribution on the surface of the finite-AR panel to understand the importance of shear layer vorticity flux vs. the boundary layer vorticity flux and see how the interaction with the wing surface regulates the LEV circulation and . As shown for the 2-D airfoil, the pressure distribution is the second primary source of the vorticity generation as well as propulsive forces acting on the panel.

Furthermore, to predict the ultimate wake structure and aerodynamic loads, it is necessary to consider the aspects of biological locomotions that have not been considered in the present work. Investigation of other basic kinematics such as pitching and rolling, and examination of other geometries such as different planform shapes, will yield an increased understanding of the mechanics of propulsors. For example, as Yilmaz and Rockwell (2012) reported, the shape of planform affects on the spanwise velocity within the leading edge vortex. Also by changing the kinematics to the rotational wings, it is expected to observe other mechanisms to be involved in vorticity transport in the LEV such as centrifugal pumping due to the rotation of the wing.

APPENDIX A
UNCERTAINTY ANALYSIS

In this Appendix, the analysis of the uncertainties in Equation 4.3 is described in detail based on the study of Wojcik [76]. This analysis was done on the 2-D PIV data for the case of $h_o/c = 0.3$, $St = 0.2$, $k = 1.05$, at $\phi = 45^\circ$ where the rate of change in vorticity fluxes is maximum. Figure A.1 shows contours of the U_x, U_y, and U_z as a fraction of the free-stream velocity, and contours of the ω_z. The green box shows the boundary of the control vlume used for the flux analysis.

A.1 Velocity and Vorticity

The velocity vectors are calculated using PIV by first using a cross-correlation analysis to determine a mean particle displacement within a sub-window of the domain between the two images and dividing by the time interval separating the image pair [50]. For example, the velocity component in x direction, U_x, can be defined as:

$$U_x = \frac{\Delta x}{M \Delta t} \tag{A.1}$$

Where M is the magnification ratio. The total uncertainty in the streamwise velocity can be obtained by once again taking partial derivatives of U_x with respect to the terms that will contribute error.

$$\delta_{U_x} = \frac{\delta_{\Delta x}}{M \Delta t} \tag{A.2}$$

The camera was calibrated with the laser plane using a LaVision type # 20 calibration plate a third-order polynomial fit to the view, essentially dewarping the image. The root-mean-square (RMS) of the fit was 0.106 pixels which is in the range (less than 0.3) to be

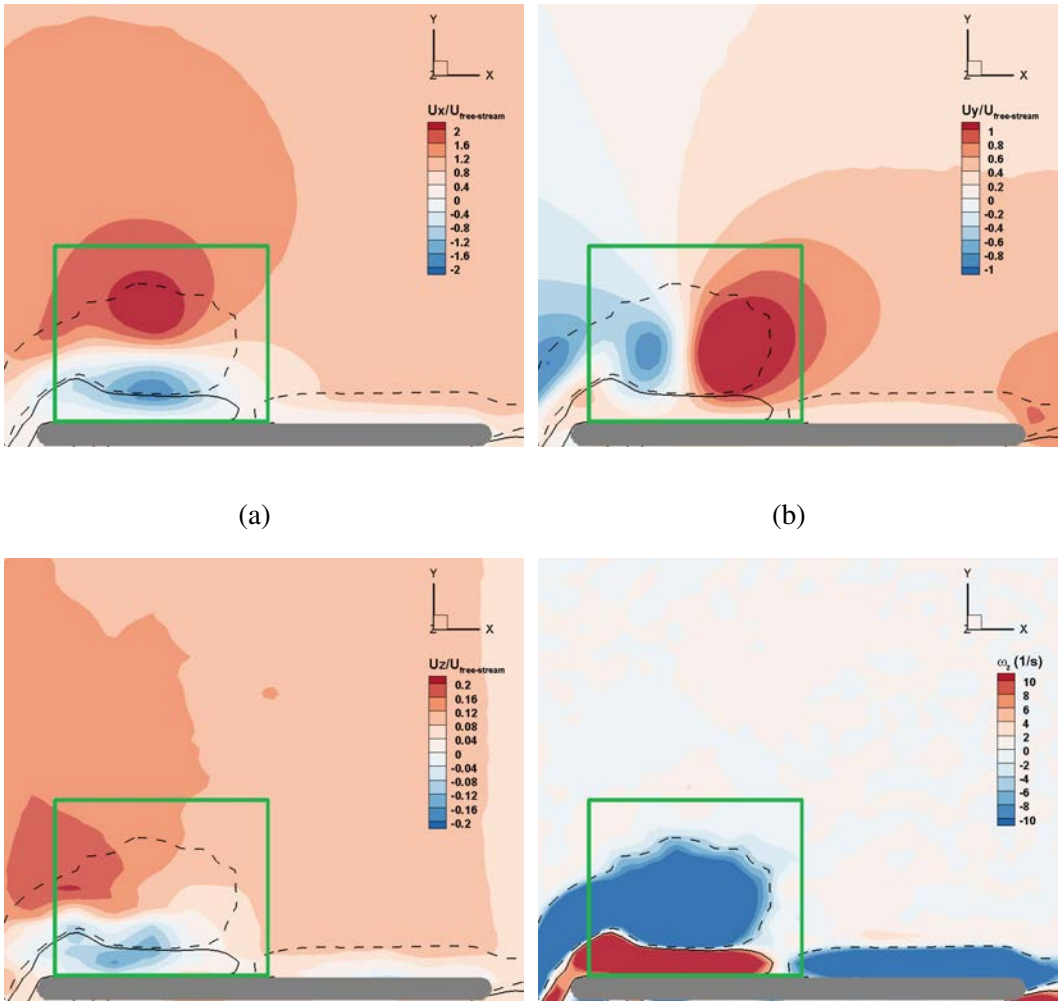

(a) (b)

(c) (d)

Figure A.1: Contours of velocity components as a fraction of free-stream velocity: (a) U_x, (b) U_y , (c) U_z, and (d) contours of out-of-plane vorticity ω_z for $St = 0.2$, $h_0/c = 0.3$, $k = 1.05$ at $\phi = 45°$. Free stream velocity is 130 (mm/s). Solid lines represent positive values and dashed lines represent negative values of the vorticity contained within the contour.

considered as ”high quality”. With the quality of the data obtained and previous publications [34], the assumed uncertainties for the change in pixel position for $\delta_{\Delta x}$, $\delta_{\Delta y}$, $\delta_{\Delta z}$ were 0.1, 0.1, and 0.3 pixels, respectively. Since the calibration was of high quality, the uncertainty in the magnification ratio is assumed to not be a major component of uncertainty in the spanwise velocity. The uncertainty in Δt is determined by the laser timing and can be as high as 10 to 100 nanoseconds, and assumed to be negligible.

During the processing of the PIV images , a window size of 32×32 was used. This implied the magnification ratio was 0.02924 mm/pixel. Lastly, the Δt used between laser pulses for the data acquired was 1250 microseconds. Using these values, the uncertainties can be obtained as seen below:

$$\delta_{U_x} = \delta_{U_y} = 2.3394(\text{mm/s}) \tag{A.3}$$

which is about 1.8% of free stream velocity.

$$\delta_{U_z} = 3.5345(\text{mm/s}) \tag{A.4}$$

which is about 2.7% of free stream velocity. Moreover, dynamic range of velocity DR_v corresponds to the ratio of maximum to minimum resolvable velocity which is defined as below:

$$DR_v = \frac{U_{\max}}{\delta_v} = \frac{S_{\max}}{\delta_S} \tag{A.5}$$

where S is displacement and δ_v and δ_s are the uncertainty in velocity and displacement, respectively. Keane and Adrian [38] state that the displacement S should be smaller than one quarter of the interrogation window size d_I. Therefore, DR_v is represented by:

$$DR_v = \frac{\frac{1}{4}d_I}{\delta_S} \tag{A.6}$$

Based on this equation, the actual increase in dynamic velocity range can be determined. Assuming $\delta_s = 0.1$ pixel and $d_I = 64$ pixel, the dynamic velocity range obtained in laboratory conditions is $DR_v = 160 : 1$.

The out-of-plane vorticity component was calculated using the central difference scheme. Using the uncertainties in the velocity components, the uncertainty in the vorticity values can be determined by:

$$\delta_{\omega_z} = \left(\frac{\delta_{U_y}^2}{2X_g^2} + \frac{\delta_{U_x}^2}{2Y_g^2} \right)^{\frac{1}{2}} \tag{A.7}$$

where the X_g and Y_g were the spacing between vector points and both determined to be 0.367 mm. This yeilds:

$$\delta_{\omega_z} = 3.8616(1/\text{s}) \tag{A.8}$$

which is about 5% of maximum vorticity magnitude in the flow field.

A.2 LEV Circulation

To determine the circulation of a vortex, a MATLAB code was implemented using a vorticity threshold for a specified area where the uncertainty in Γ is:

$$\delta_\Gamma = \delta_{\omega_{z_{ij}}} \Delta x \Delta y \sqrt{N} \tag{A.9}$$

A rectangular cross-section was used as the planar control volume, and based on the vector spacing, it was determined to have approximately $N = 1600$ vectors in the control volume. This yields $\delta_\Gamma = 247.1424(\text{mm}^2/\text{s})$ which is approximately $\pm$ 1.37% of LEV circulation.

A.3 Spanwise Convection of Vorticity

From Equation 4.3, the spanwise convection of spanwise vorticity is:

$$\text{Convection} = -\int_{A_z} u_z \frac{\partial \omega_z}{\partial z}\, dA_z \tag{A.10}$$

Therefore, the uncertainty in the convection term is calculated discretely as described by Wojcik [76] by:

$$\delta_{Convection} = \left[\left(\frac{\partial conv}{\partial U_z}\delta_{U_z}\right)^2 + \left(\frac{\partial conv}{\partial \omega_{z_{k+1}}}\delta_{\omega_{z_{k+1}}}\right)^2 + \left(\frac{\partial conv}{\partial \omega_{z_{k-1}}}\delta_{\omega_{z_{k-1}}}\right)^2 + \left(\frac{\partial conv}{\partial X_g}\delta_{X_g}\right)^2 + \left(\frac{\partial conv}{\partial Y_g}\delta_{Y_g}\right)^2 + \left(\frac{\partial conv}{\partial Z_g}\delta_{Z_g}\right)^2\right]^{\frac{1}{2}} \tag{A.11}$$

By substituting the values in equation A.11, the uncertainty in the convection term is 9.59 mm^2/s^2 which is approximately ± 0.23% of the convection value at $\phi = 45°$.

A.4 *x*-Tilting and *y*-Tilting of LEV

From Equation 4.3, the *x*-tilting and *y*-tilting terms are represented as:

$$x - tilting = \int_{A_z} \left(\omega_x \frac{\partial u_z}{\partial x}\right) dA_z \tag{A.12}$$

$$y - tilting = \int_{A_z} \left(\omega_y \frac{\partial u_z}{\partial y}\right) dA_z \tag{A.13}$$

The general uncertainty in the *x*-tilting is derived by Wojcik [76] in equation A.14:

$$\delta_{X_{Tilting}} = \left[\left(\frac{\partial X_{Tilting}}{\partial U_{z_{j+1}}}\delta_{U_{z_{j+1}}}\right)^2 + \left(\frac{\partial X_{Tilting}}{\partial U_{z_{j-1}}}\delta_{U_{z_{j-1}}}\right)^2 + \left(\frac{\partial X_{Tilting}}{\partial U_{y_{k+1}}}\delta_{U_{y_{k+1}}}\right)^2 + \left(\frac{\partial X_{Tilting}}{\partial U_{y_{k-1}}}\delta_{U_{y_{k-1}}}\right)^2 + \left(\frac{\partial X_{Tilting}}{\partial U_{z_{i+1}}}\delta_{U_{z_{i+1}}}\right)^2 + \left(\frac{\partial X_{Tilting}}{\partial U_{z_{i-1}}}\delta_{U_{z_{i-1}}}\right)^2 + \left(\frac{\partial X_{Tilting}}{\partial X_g}\delta_{X_g}\right)^2 + \left(\frac{\partial X_{Tilting}}{\partial Y_g}\delta_{Y_g}\right)^2 + \left(\frac{\partial X_{Tilting}}{\partial Z_g}\delta_{Z_g}\right)^2\right]^{\frac{1}{2}} \tag{A.14}$$

where the following assumptions were made:

$$\delta_{X_g} \approx \delta_{Y_g} \approx \delta_{Z_g} \approx 0 \tag{A.15}$$

$$\delta_{U_{y_{k+1}}} = \delta_{U_{y_{k-1}}} = \delta_{U_y} \tag{A.16}$$

$$\delta_{U_{z_{i+1}}} = \delta_{U_{z_{i-1}}} = \delta_{U_{z_{j+1}}} = \delta_{U_{z_{j-1}}} = \sigma_{U_z} \tag{A.17}$$

Similar approach was used for the tilting term in y direction and assumed:

$$\delta_{U_{x_{k+1}}} = \delta_{U_{x_{k-1}}} = \delta_{U_x} \tag{A.18}$$

Using the related values, results in an uncertainty for both the x-tilting and y-tilting terms to be 2.35 mm^2/s^2, and the representative x-tilting and y-tilting terms equal to 310 and 363 mm^2/s^2 which yeilds to ± 0.75% and ± 0.65% uncertainty respectively.

A.5 Convection of Vorticity Across Boundaries

The shear layer vorticity flux was evaluated discretely as described in Equation 4.3. The shear layer term is shown as below:

$$\text{Boundaries} = \int_{1\text{ to }3} u_n\, \omega_z\, dL \tag{A.19}$$

The general uncertainty of the shear layer term is expressed as:

$$\delta_{Boundary(1)} = \left[\left(\frac{\partial Boundary}{\partial U_x}\delta_{U_x}\right)^2 + \left(\frac{\partial Boundary}{\partial \omega_z}\delta_{\omega_z}\right)^2 + \left(\frac{\partial Boundary}{\partial Y_g}\delta_{Y_g}\right)^2\right]^{\frac{1}{2}} \tag{A.20}$$

U_x velocity and ω_z vorticity value over the boundary 1 are shown in Figures A.1(a) and A.1(d) respectively. Those values yield an uncertainty in the shear layer term of 496.3 mm^2/s^2 for boundary 1, 53.7 mm^2/s^2 for boundary 2, and 151.3 mm^2/s^2 for boundary 3.

The value of shear layer vorticity flux at $\phi = 45^\circ$ was 40887 mm^2/s^2 for boundary 1, 1825 mm^2/s^2 for boundary 2, 14993 mm^2/s^2 for boundary 3. Therefore, the relative error in the shear layer vorticity flux was calculated to be ± 1.2% for boundary 1, ± 2.9% for boundary 2, and ± 1.0% for boundary 3.

APPENDIX B
3-D INTERPOLATION

For the 3-D volume reconstruction, tri-quadratic interpolation method was used which is a method for interpolating values of a function defined at arbitrary points in 3D space onto the new 3D grid.

B.1 Quadratic Spline Interpolation

In this section, the concept of spline interpolation using second-order polynomials is explained. Spline interpolation is preferred over high-order polynomial interpolation because the interpolation error is small even when using low degree polynomials for the spline. The second-order spline can be represented generally as:

$$f_i(x) = a_i x^2 + b_i x + c_i \tag{B.1}$$

Figure B.1 has been included to clarify the notations. For $n + 1$ data points, there are n intervals and consequently $3n$ unknown coefficients. Therefore, $3n$ equations are needed to evaluate these unknowns. To find these unknowns the following steps need to be considered as discussed by Chapra and Canale [17]:

1- The function values must be equal at the interior points for $i = 1$ to $n - 1$ which provide $2 \times (n - 1)$ equations:

$$a_{i+1} x_i^2 + b_{i+1} x_i + c_{i+1} = f(x_i) \tag{B.2}$$

$$a_i x_i^2 + b_i x_i + c_i = f(x_i) \tag{B.3}$$

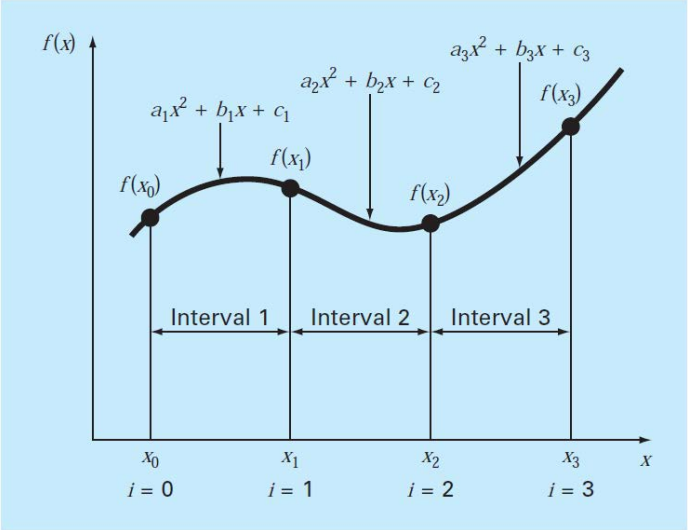

Figure B.1: Notation used to drive the quadratic splines (Adopted from Chapra and Canale [17]).

2- The first and last functions must pass through the end points which adds two more equations:

$$a_1 x_0^2 + b_1 x_0 + c_1 = f(x_0) \tag{B.4}$$

$$a_n x_n^2 + b_n x_n + c_n = f(x_n) \tag{B.5}$$

3- The first derivatives at the interior points must be equal where $f'(x) = 2ax+b$. Therefore, the condition can be represented as below which provides another $n - 1$ equations:

$$2a_i x_i + b_i = 2a_{i+1} x_i + b_{i+1} \tag{B.6}$$

4- Assume that the second derivative is zero at the first point in which the first two points assumed to be connected by a straight line, can be expressed as:

$$a_i = 0 \tag{B.7}$$

Now we have total $3n$ equations which can be solved for $3n$ interval coefficients at each 3 points in one direction.

B.2 Tri-Quadratic Interpolation

In this method, a sequential application of one dimensional quadratic spline interpolation is used in 3 directions as explained by Lekien and Marsden [41]. Since we know the value of, for example, velocity U at each grid point ($U(i, j, k)$), first we can interpolate along z direction using one-dimensional quadratic splines interpolation method as discussed in section B.1:

$$h(i, j, z) = \mathrm{QINT_z}[U(i, j, k-1), U(i, j, k), U(i, j, k+1)] \tag{B.8}$$

where $\mathrm{QINT_z}$ represents the quadratic spline interpolation only in z direction using the four steps as discussed in B.1. Also, $U(i, j, k-1)$, $U(i, j, k)$, and $U(i, j, k+1)$ are the velocity values at three neighbor points Then we interpolate the h values along y direction:

$$g(i, y, z) = \mathrm{QINT_y}[h(i, j-1, z), h(i, j, z), h(i, j+1, z)] \tag{B.9}$$

Finally, we interpolate the g values along x direction:

$$f(x, y, z) = \mathrm{QINT_x}[g(i-1, y, z), g(i, y, z), g(i+1, y, z)] \tag{B.10}$$

This gives us a predicted value for the target point at (x,y,z). Note that the described procedure is just a general procedure to interpolate data in three directions and for horizontal and vertical planes different approches were used. For example, for the horizontal planes ($x - y$ plane), since the x and y components are known, it is necessary to start in x and y directions first, then interpolate in z direction (out-of-plane direction).

REFERENCES

[1] M. Acharya and M. H. Metwally. Unsteady pressure field and vorticity production over a pitching airfoil. *AIAA J.*, 30(2):403–411, 1992.

[2] I. Akhtar, R. Mittal, G. V. Lauder, and E. A. Drucker. Hydrodynamics of a biologically inspired tandem flapping foil configuration. *Theo. Comp. Fluid Dyn.*, 21:155–170, 2007.

[3] J. M. Anderson, K. Streitlien, D. S. Barrett, and M. S. Triantafyllou. Oscillating foils of high propulsive efficiency. *J. Fluid Mech.*, 360:41–72, 1998.

[4] Y. S. Baik, J. M Rausch, L. P. Bernal, and M. V. Ol. Experimental investigation of pitching and plunging airfoils at reynolds number between 1×10^4 and 6×10^4. In *39th AIAA Fluid Dynamics Conference*, San Antonio, TX, June 2009. AIAA Paper 2009-4030.

[5] R. L. Bisplinghoff, H. Ashley, and R. L. Halfman. *Aeroelasticity*. Addison-Wesley, 1955.

[6] D. G. Bohl and M. M. Koochesfahani. Molecular tagging velocimetry measurements of axial flow in a concentrated vortex core. *Phys. Fluids*, 16(11):4185–4191, 2004.

[7] D. G. Bohl and M. M. Koochesfahani. MTV measurements of the vortical field in the wake of an airfoil oscillating at high reduced frequency. *J. Fluid Mech.*, 620:63–88, 2009.

[8] I. Borazjani and F. Sotiropoulos. Numerical investigation of the hydrodynamics of carangiform swimming in the transitional and inertial flow regimes. *J. Exp. Biol.*, 211:1541–1558, 2008.

[9] I. Borazjani and F. Sotiropoulos. Numerical investigation of the hydrodynamics of anguilliform swimming in the transitional and inertial flow regimes. *J. Exp. Biol.*, 212:576–592, 2009.

[10] I. Borazjani and F. Sotiropoulos. On the role of form and kinematics on the hydrodynamics of self-propelled body/caudal fin swimming. *J. Exp. Biol.*, 213:89–107, 2010.

[11] M. S. H. Boutilier and S. Yarusevych. Effects of end plates and blockage on a low reynolds number airfoil experiment. In *41st AIAA Fluid Dynamics Conference*, Honolulu, HI, June 2011. AIAA Paper 2011-3723.

[12] J. Buchholz, A. Eslam Panah, J. Akkala, K. Wabick, and C. Wojcik. Vorticity generation and transport on a plunging wing. In *52th AIAA Aerospace Sciences Meeting*, National Harbor, Maryland, 13-17 January 2014.

[13] J. H. J. Buchholz and A. J. Smits. On the evolution of the wake structure produced by a low-aspect-ratio pitching panel. *J. Fluid Mech.*, 546:433–443, 2006.

[14] J. H. J. Buchholz and A. J. Smits. The wake structure and thrust performance of a rigid low-aspect-ratio pitching panel. *J. Fluid Mech.*, 603:331–365, 2008.

[15] D. E. Calderon, Z. Wang, I. Gursul, and M. R. Visbal. Volumetric measurements and simulations of the vortex structures generated by low aspect ratio plunging wings. In *50th AIAA Aerospace Sciences Meeting*, Nashville, TN, January 2012. AIAA Paper 2012-0914.

[16] D. E. Calderon, Z. J. Wang, and I. Gursul. Effect of wing geometry on the lift of a plunging finite wing. In *40th AIAA Fluid Dynamics Conference*, Chicago, IL, June 2010. AIAA Paper 2010-4459.

[17] S. Chapra and R. Canale. Numerical methods for engineers with personal computer applications. McGraw-Hill, Inc., New York, NY, USA, 1988.

[18] R. P. Clark and A. J. Smits. Thrust production and wake structure of a batoid-inspired oscillating fin. *J. Fluid Mech.*, 562:415–429, 2006.

[19] R. K. Cohn and M. M. Koochesfahani. Effect of boundary conditions on axial flow in a concentrated vortex core. 5(1):280–282, 1993.

[20] J. O. Dabiri. Optimal vortex formation as a unifying principle in biological propulsion. *Annu. Rev. Fluid Mech.*, 41:17–33, 2009.

[21] T. L. Doligalski, C. R. Smith, and J. D. A. Walker. Vortex interactions with walls. *Annu. Rev. Fluid Mech.*, 26:573–616, 1994.

[22] H. Dong, R. Mittal, and F. M. Najjar. Wake topology and hydrodynamic performance of low-aspect-ratio flapping foils. *J. Fluid Mech.*, 566:309–343, 2006.

[23] A. Eslam Panah and J. H. J. Buchholz. Parameter dependence of vortex interactions on a two-dimensional plunging plate. *Expts. Fluids*, 2014. DOI: 10.1007/s00348-014-1687-7.

[24] P. Freymuth. Propulsive vortical signature of plunging and pitching airfoils. *AIAA J.*, 27(9):1200–1205, 1988.

[25] P. Freymuth. Flow visualization in fluid mechanics. 64(1):1–18, 1993.

[26] M. Gharib, E. Rambod, and K Shariff. A universal time scale for vortex ring formation. *J. Fluid Mech.*, 360:121–140, 1998.

[27] R. Gopalkrishnan, M. S. Triantafyllou, G. S. Triantafyllou, and D. Barrett. Active vorticity control in a shear flow using a flapping foil. *J. Fluid Mech.*, 274:1–21, 1994.

[28] L. Graftieaux, M. Michard, and N. Grosjean. Combining PIV, POD and vortex identification algorithms for the study of unsteady turbulent swirling flows. *Meas. Sci. Tech.*, 12(9):1422–1429, 2001.

[29] K. Granlund, M. V. OL, and L. P. Bernal. Experiments on pitching plates: Force and flowfield measurements at low reynolds numbers. In *49th AIAA Aerospace Sciences Meeting*, Orlando, FL, January 2011. AIAA Paper 2011-872.

[30] M. A. Green and A. J. Smits. Effects of three-dimensionality on thrust production by a pitching panel. *J. Fluid Mech.*, 531:211–220, 2008.

[31] J. P. Hagen and M. Kurosaka. Corewise cross-flow transport in hairpin vortices – the "'tornado effect"'. 5(12):3167–3174, 1993.

[32] S. M. Hajimirzaie, C. J. Wojcik, and J. H. J. Buchholz. The role of shape and relative submergence on the structure of wakes of low-aspect-ratio wall-mounted bodies. *Expts. Fluids*, 53(6):1943–1962, 2012.

[33] H. Hu, L. Clemons, and H. Igarashi. An experimental study of the unsteady vortex structures in the wake of a root-fixed flapping wing. *Expts. Fluids*, 51:347–359, 2011.

[34] H. Huang, D. Dabiri, and M. Gharib. On errors of digital particle image velocimetry. *Meas. Sci. Tech.*, 8:1427–1440, 1997.

[35] J. C. R. Hunt, A. A. Wray, and P. Moin. Eddies, stream, and convergence zones in turbulent flows. Technical Report CTR-S88, Center for Turbulence Research, 1988.

[36] K. D. Jones, C. M. Dohring, and M. F. Platzer. Wake structures behind plunging airfoils: a comparison of numerical and experimental results. 1996. AIAA Paper 96-0078.

[37] K. D. Jones, C. M. Dohring, and M. F. Platzer. Experimental and computational investigation of the knoller-betz effect. *AIAA J.*, 36(7):1240–1246, 1998.

[38] R.D. Keane and R. J. Adrian. Optimization of particle image velocimeters. part I: Double pulsed systems. *Meas. Sci. Technol.*, 1:1202–1215, 1990.

[39] M. M. Koochesfahani. Vortical patterns in the wake of an oscillating airfoil. *AIAA J.*, 27(9):1200–1205, 1989.

[40] J. C. S. Lai and M. F. Platzer. Jet characteristics of a plunging airfoil. *AIAA J.*, 37(12):1529–1537, 1999.

[41] F. Lekien and J. Marsden. Tricubic interpolation in three dimensions. 63:455–471, 2005.

[42] D. Lentink and M. H. Dickinson. Biofluiddynamic scaling of flapping, spinning, and translating fins and wings. *J. Exp. Biol.*, 212:2691–2704, 2009.

[43] G. C. Lewin and H. Haj-Hariri. Modelling thrust generation of a two-dimensional heaving airfoil in a viscous flow. *J. Fluid Mech.*, 492:339–362, 2003.

[44] J. Longo, J. Shao, M. Irvine, and F. Stern. Phase-averaged piv for the nominal wake of a surface ship in regular head waves. 129:524–540, 2007.

[45] K. B. Lua, T. T. Lim, and K. S. Yeo. Effect of wing-wake interaction on aerodynamic force generation on a 2D flapping wing. *Expts. Fluids*, 51:178–195, 2011.

[46] K. B. Lua, T. T. Lim, K. S. Yeo, and G. Y. Oo. Wake-structure formation of a heaving two-dimensional elliptic airfoil. *AIAA J.*, 45(7):1571–1583, 2007.

[47] A. Luton, S. Ragab, and D. Telionis. Interaction of spanwise vortices with a boundary layer. *Phys. Fluids*, 7:2757–2765, 1995.

[48] L. Guglielmini. M. Triantafyliou P. Blondeaux, F. Fornarelli. Numerical experiments on apping foils mimicking sh-like locomotion. *Phys. Fluids*, 17, 2005b.

[49] M. F. Platzer, K. D. Jones, J. Young, and J. C. S. Lai. Flapping-wing aerodynamics: Progress and challenges. *AIAA J.*, 48(9):2136–2149, 2008.

[50] M. Raffel, C. Willert, S. T. Wereley, and J. Kompenhans. *Particle Image Velocimetry: A Practical Guide*. Springer, Berlin, 2 edition, 2007.

[51] D. Rival, G. Hass, and C. Tropea. Recovery of energy from leading- and trailing-edge vortices in tandem-airfoil configurations. 48(1):203–211, 2011.

[52] D. Rival, T. Prangemeier, and C. Tropea. The influence of airfoil kinematics on the formation of leading-edge vortices in bio-inspired flight. *Expts. Fluids*, 46:823–833, 2009.

[53] D. E. Rival, J. Kriegseis, P. Schaub, A. Widmann, and C. Tropea. A criterion for vortex separation on unsteady aerodynamic profiles. In *51st AIAA Aerospace Sciences Meeting*, Grapevine, TX, 2013. AIAA. AIAA Paper 2013-0836.

[54] O. Robinson and D. Rockwell. Construction of three-dimensional images of flow structure via particle tracking techniques. *Expts. Fluids*, 14:257–270, 1993.

[55] T. Sarpkaya. A critical review of the intrinsic nature of vortex induced vibrations. Technical report, Naval Postgraduate School, 2003.

[56] W. Shyy, H. Aono, S. K. Chimakurthi, P. Trizila, C. K. Kang, C. E. S. Cesnik, and H. Liu. Recent progress in flapping wing aerodynamics and aeroelasticity. *Prog. Aerosp. Sci.*, 46:284–327, 2010.

[57] J. M. M. Sousa. Turbulent flow around a surface-mounted obstacle using 2D-3C DPIV. *Expts. Fluids*, 33:854–862, 2002.

[58] K. Taira and T. Colonius. Three-dimensional flows around low-aspect-ratio flat-plate wings at low reynolds numbers. *J. Fluid Mech.*, 623:187–207, 2009.

[59] G. K. Taylor, R. L. Nudds, and A. L. R. Thomas. Flying and swimming animals cruise at a strouhal number tuned for high power efficiency. 425:707–711, 2003.

[60] T. Theodorsen. General theory of aerodynamic instability and the mechanism of flutter. Report 496, NACA, 1935.

[61] G. S. Triantafyllou, M. S. Triantafyllou, and M. A. Grosenbaugh. Optimal thrust development in oscillating foils with application to fish propulsion. 7:205–224, 1993.

[62] M. S. Triantafyllou, G. S. Triantafyllou, and R. Gopalkrishnan. Wake mechanics for thrust generation in oscillating foils. 3(12):2835–2837, 1991.

[63] P. Trizila, C. K. Kang, H. Aono, W. Shyy, and M. Visbal. Hydrodynamics of fishlike swimming. *AIAA J.*, 49:806–823, 2011.

[64] M. R. Visbal. High-fidelity simulation of transitional flows past a plunging airfoil. *AIAA J.*, 47(11):2685–2697, 2009.

[65] M. R. Visbal. Numerical investigation of deep dynamic stall of a plunging airfoil. *AIAA J.*, 49(10):2152–2170, 2011.

[66] M. R. Visbal. Three-dimensional flow structure on a heaving low-aspect-ratio wing. In *49th AIAA Aerospace Sciences Meeting.*, Orlando, Florida, 2011. AIAA Paper 2011-219.

[67] M. R. Visbal. Flow structure and unsteady loading over a pitching and perching low-aspect-ratio wing. In *42nd AIAA Fluid Dynamics Conference.*, New Orleans, Louisiana, 2012. AIAA Paper 2012-3279.

[68] M. R. Visbal, R. E. Gordnier, and M. C. Galbraith. Direct numerical simulation of a forced transitional plane wall jet. 1998. AIAA Paper 98-2643.

[69] K. D. von Ellenrieder, K. Parker, and J. Soria. Flow structures behind a heaving and pitching finite-span wing. *J. Fluid Mech.*, 490:129–138, 2003.

[70] K. McAlister W. McCroskey, L. Carr. Dynamic stall experiments on oscillating airfoils. *AIAA J.*, 14:57–63, 1976.

[71] H. Wagner. Uber die entstehung des dynamischen auftriebes von tragfliigeln. pages 17–35, 1925. Z. angew. Math. Mech.

[72] J . D. A. Walker. The boundary layer due to rectilinear vortex. *Proc. R. Soc. London Ser. A.*, 359:167–88, 1978.

[73] C. Wang and J. Eldredge. Low-order phenomenological modeling of leading-edge vortex formation. 2012.

[74] Z. J. Wang. Vortex shedding and frequency selection in flapping flight. *J. Fluid Mech.*, 410:323–341, 2000.

[75] C. H. K. Williamson and A. Roshko. Vortex formation in the wake of an oscillating cylinder. 2:355–381, 1988.

[76] C. J. Wojcik. The dynamics of spanwise vorticity on a rotating flat plate in a starting motion. Master's thesis, University of Iowa, 2012.

[77] C. J. Wojcik and J. H. J. Buchholz. Parameter variation and the leading-edge vortex of a rotating flat plate. *AIAA J.*, 2013. Accepted.

[78] C. J. Wojcik and J. H. J. Buchholz. Vorticity transport on a rotating blade. *J. Fluid Mech.*, 2013. Accepted.

[79] J. Wu. Theory for aerodynamic force and moment in viscous flows. *AIAA J.*, 19:432–441, 1981.

[80] J. Z. Wu and J. M Wu. Interactions between a solid surface and a viscous compressible flow field. *J. Fluid Mech.*, 254:183–211, 1993.

[81] T. Yilmaz, M. Ol, and D. Rockwell. Scaling of flow separation on a pitching low aspect ratio plate. 26:1034–1041, 2010.

[82] T. Yilmaz and D. Rockwell. Three-dimensional flow structure on a maneuvering wing. *Expts. Fluids*, 48:539–544, 2010.

[83] T. O. Yilmaz and D. Rockwell. Flow structure on finite-span wings due to pitch-up motion. *J. Fluid Mech.*, 691:518–545, 2012.

[84] J. Young and J. C. S. Lai. Oscillation frequency and amplitude effects on the wake of a plunging airfoil. *AIAA J.*, 42(10):2042–2052, 2004.